2000

Thermodynamic and solidification modeling of laser welded nickel-based alloys

Brian D. (Dale) Newbury
Lehigh University

Recommended Citation

Newbury, Brian D. (Dale), "Thermodynamic and solidification modeling of laser welded nickel-based alloys" (2000). *Theses and Dissertations.* Paper 668.

Newbury, Brian D.

Thermodynamic and Solidification Modeling of Laser Welded Nickel-Based Alloys

January 2001

Thermodynamic and Solidification Modeling of Laser Welded Nickel-Based Alloys

By

Brian D. Newbury

A Thesis

Presented to the Graduate and Research Committee

Of Lehigh University

In Candidacy for the Degree of

Master of Science

In

Materials Science and Engineering

Lehigh University

November 13, 2000

CERTIFICATE OF APPROVAL

This thesis is accepted and approved in partial fulfillment of the requirements for the degree of Master of Science.

11-20-02

Date

Thesis Advisor

Chairman of Department

Acknowledgements

I would like to thank my advisor, Dr. John DuPont, for giving me the opportunity of furthering my education. I have learned a great deal about both materials science and life during my post undergraduate stay; most of it I owe to him. I would also like to thank Dr. Arnold Marder, for his expertise and advice in my studies and of course the Mets. Arlan Benscoter provided help and solutions to all my metallographic problems too many times to count, and for this I thank him greatly. Thanks also go out to Mike Rex for helping me with all the plasma cutting and machining (and there was a lot of it), most of it at short notice. I would also like to thank Dr. Zhen Liu, the Taskmaster, for his invaluable help with the AEM analysis which proved so important in my results.

I am very greatful for the funding of my research, which was sponsored by Sandia National Laboratories. Many people at Sandia provided advice and help without hesitation. I'd like to thank Dr. Charles Robino for performing the laser welds for me and his guidance throughout my project. I would also like to thank Dr. Phillip Fuerschbach for his time and help with the melting efficiency section of my results. I would also like to thank Haynes International for providing me with the Hastelloy B2 and Ni200 raw materials for my study.

I would also be remiss if I did not thank my fellow graduate (and former graduate) students in my group, Steve Banovic, Don Susan, Jesse Nawrocki, Kevin Luer, Chad Kusko, and Nick Barbosa. They have all helped me greatly throughout my time here and I owe a good deal to them. I also would like to thank my fellow graduate

students who I didn't work directly with but still had an impact on my life: Dan Lewis, William VanGeertruyden, Mario Epler, and Alex Banadar to name a few.

I would also like to thank my family for all the love and support they have given me. To my Mom for always sending me cookies to lift my spirits and coupons so I'd have more money for bike parts. To my Dad for his endless help and for making me want to be a scientist in the first place! And of course to my sister Jenny for her love and trudging through grad school and letting me know what to expect around the corner.

Last, and most certainly not least, to Melissa Lim who has always been there to help me through the hard times and revel in the good times. Her love and support mean a great deal to me and I am especially grateful that she is in my life. I love you very much.

Dedicated to my Father

Dale Newbury

Table of Contents

List of Tables

Chapter 2

Chapter 3

Chapter 4

Chapter 5

List of Figures

Chapter 2

Chapter 3

Chapter 4

Chapter 5

Abstract

Laser beam welding is one of the leading methods for joining nickel-based alloys due to its ability to have extremely high travel speeds; minimal heat affected zone size, and capability to fuse a wide range of joint designs. Laser beam welding is often used to provide high solidification rates in an effort to reduce microsegregation in the fusion zone. However, it is often costly and time consuming to develop a sufficient welding schedule through trial and error.

A technique has been determined to model fusion zone characteristics such as cell spacing and cell core composition by coupling the thermodynamics modeling package ThermoCalc with solidification models. ThermoCalc was verified for accuracy over a range of nickel-based alloys calculating liquidus and solidus temperatures, liquidus and solidus slopes, partition coefficients, and phase diagrams. The ThermoCalc program was then used to calculate pertinent inputs for solidification modeling. The cell spacing, solidification velocity throughout the weld pool, and cell core composition were measured to compare to the predictions of the model for laser welding. Cell spacing and solidification velocity were measured for gas tungsten arc welds (GTA) prepared under similar conditions to compare to the laser welds as a traditional arc process. It was found that the coupling of thermodynamics modeling and solidification modeling was accurate in predicting essential weld pool characteristics.

1.0 Introduction

Welding is one of the most basic and versatile joining processes in use in industry today. The welding process involves melting metal (or material) to fuse components together. A simple process in theory, however when applied to today's high tech alloys that are often custom tailored for a specific application, problems can arise. Often the materials to be joined have undergone a specific temperature history to impart mechanical properties that will be affected adversely after welding. Corrosion resistance deterioration, loss of precipitation strengthening and hot cracking are some examples of problems that alloys may undergo after welding [1.1, 1.2]. If the degree of susceptibility for these problems can be predicted for an alloy before costly experiments are run, time and money can be saved.

High energy density welding processes such as laser welding are relatively new technologies when compared to the traditional arc welding processes. High energy density processes have many advantages, one being that they allow greater joint design flexibility, since often only line of sight access is required instead of accommodating a bulky welding torch [1.3]. High energy density processes impart much less total heat into the base metal, thus reducing the amount of change to the microstructure. These processes are also capable of being performed at much higher travel speeds, which in theory leads to larger solidification rates. If solidification occurs fast enough, the microsegregation mentioned above lessens or can even disappear. For these reasons, there is much interest in studying laser weld microstructure evolution.

Many of these problems that arise from the welding process can be traced to the non-equilibrium solidification that arises from the welding process. The high temperature gradients and cooling rates associated with welding lead to solidification where diffusion often does not occur, giving rise to compositional gradients within the weld pool on a microstructural level. The fact that many of the problems associated with welding are caused by segregation of alloying elements in the fusion zone has caused much research into understanding the key factors to control segregation [1.2].

General alloy solidification models have been modified to apply to welding with some success in predicting compositional gradients. However, most of these models are binary or ternary solidification models while most practical alloys are multi-component (more than three elements) and often upwards of 8 or 10 elements. The addition of elements to solidification models increases the complexity dramatically, so the assumption of binary or ternary systems is often done to provide for a manageable model.

Another trend in solidification modeling is the use of computer-based thermodynamic databases. These databases have been in development for some years and have recently been developed for nickel-based alloys. Thermodynamic databases allow equilibrium calculations of phase diagrams, liquidus and solidus temperatures, liquidus and solidus slopes, and many other pertinent thermodynamics-based calculations.

There has been little research done to couple these two approaches. While there has been a significant amount of research done to predict weld pool microstructure, this research has always relied on experimental measurement of pertinent data required in the modeling. This data (liquidus and solidus slopes, etc.) often requires tedious experimentation to determine.

The purpose of this research is to develop a technique to model nickel-based alloy laser fusion zone solidification (microstructure development and microsegregation tendency) given alloy composition and pertinent welding parameters. To do this the thermodynamics modeling software package ThermoCalc is used to calculate phase diagrams and pertinent thermal data required for solidification models. The outputs from the thermodynamics modeling is then used to predict the fusion zone structure and microsegregation tendency given a welding process and parameters. This work shall give the user a technique to predict important weldment properties and dramatically reduce the amount of timely and costly experimentation associated with designing sound laser weld joints.

2.0 Literature Review

2.1 Introduction

Welding is one of today's most popular and important fabrication techniques in the joining industry. It allows a wide range of customization in geometry, ease of use, and quick turnover for the manufacturer. While the actual welding process has been in use since before the turn of the century, it is also one of the more promising fabrication techniques for the future. Advances in laser beam welding have pushed welding to the forefront of technology.

There is much work to be done to understand the welding process on a microscopic level. There has been little study of high-speed welding/solidification conditions and much is assumed from the knowledge of slow speed solidification. This work shall investigate high-speed (up to 76.2 mm/s) laser and Gas Tungsten Arc Welding (GTAW) processes to further understand the nature of solidification at these high speeds. This knowledge would allow for much greater efficiency in the welding process as well as greater strength and physical properties of the weld area. The results of this research shall provide a means to reduce the number of time consuming and costly test welds to determine welding parameters required for sound welds. By utilizing computer accessed thermodynamic databases to model the alloy systems to be welded, welding parameters can be maximized for the highest performance at the minimum cost to the manufacturer.

2.1.1 Nickel-Molybdenum System

Laser and GTAW welds shall be performed on the Hastelloy B2 nickel-based alloy, as well as Ni-200 (commercially pure nickel). Hastelloy B2 is a multi-component alloy based on the Ni-Mo system, with other alloying elements added for reasons to be discussed later. It is important to have a grasp on the behavior of the Ni-Mo system since it forms the basis for B2. Figure 2.1 illustrates the Ni-Mo binary phase diagram. Since nickel is the major element in the alloys to be studied, the microstructure matrix is that of austenite since nickel is of FCC crystal structure. The addition of Mo is often performed to improve the chemical corrosion resistance, and is seen to cause the formation of the intermetallics Ni_4Mo, Ni_3Mo, and NiMo before turning from the Ni austenite matrix into the BCC Mo matrix. Since Hastelloy B2 contains approximately 27 wt% Mo, we shall only be concerned with the Ni rich region of the phase diagram.

According to the phase diagram shown in Figure 2.1, the first phase to solidify for this binary alloy of composition 27 wt% Mo bal. Ni (similar to the B2 alloy) would be austenite. As the alloy is cooled (under non-equilibrium conditions), the compositions of the liquid and solid will become enriched to the eutectic point (at 45.5 wt% Mo) and some of the NiMo phase would form at the end of solidification. Solid state transformations shall not be studied in this work. The high cooling rates seen in welding are expected to prevent the much slower solid state transformations seen in this system from occurring.

2.1.2 Nickel-Chromium-Molybdenum System

Since the actual alloys to be studied are not simple binary alloys, the nickel-chromium-molybdenum system should be studied as well to become familiar with the phases that form upon solidification. Figure 2.2 shows the ternary phase diagram at 1250 °C. Bloom and Grant found the σ phase to decrease in amount with temperature [2.3].

They also determined the presence of another ternary compound, arbitrarily called the P phase, which they were unable to determine the crystal structure. Further work on the 1250 °C phase diagram was completed by Raghavan et.al [2.4]. Through the use of AEM techniques they determined that the P phase was indeed present. The three intermetallic phases, δ, P, and σ are very close in lattice dimensions. The use of electron diffraction is required to determine one from another [2.4].

Figure 2.3 illustrates an experimentally determined liquidus projection for the Ni-Cr-Mo system [2.5]. It is seen that there are two main regions to the diagram, the FCC Ni-rich corner and the BCC Mo or Cr rich corners, separated by three smaller phase regions (NiMo, P, and σ). The composition of the alloy to be studied is approximately 27 wt% Mo, 0.5 wt% Cr, and balance Ni. This puts the initial solidification mode as the FCC austenite in the Ni-rich corner. There are many options that the primary solidification path can take that will be determined by the alloy's partition coefficient k. The partition coefficient can be defined as:

$$k = \frac{X_{s,A}}{X_{l,A}} \qquad (2.1)$$

where X_s and X_l are the composition of the liquid and solid for element A as defined by the phase diagram. The partition coefficient determines the tendency for that element to segregate to the liquid or solid, thus telling the direction of the primary path. The effect of the partition coefficient on the direction of the primary solidification path shall be discussed in further detail later. Once the primary solidification path is determined, the intersection of this path with the phase boundary lines of the liquidus projection will determine the rest of the solidification sequence.

If Figure 2.3 is examined closely, one will notice that there are arrows pointing in the solidification path direction along the phase boundaries. These arrows indicate the direction of decreasing temperature and the direction the solidification path takes once a certain phase boundary line is intersected. For instance, if the primary path intersects the phase boundary between austenite and P phase, the solidification path would continue down the phase boundary line towards the σ phase. At the triple point between P, austenite, and σ phase the remaining liquid shall solidify as a eutectic structure. This is because the other lines at this intersection indicate that progressing past the triple point would *increase* the systems temperature instead of decreasing it. It is helpful to think of the phase boundaries as "valleys" and the indication arrows as indicating which direction a river in the valley floor would flow. Water cannot flow uphill, and solidification cannot go against the indication arrows.

2.1.3 Alloy to be studied

In this study, the laser beam welding characteristics of the nickel based alloy Hastelloy B-2 will be examined. This alloy was picked since it represents a good model system that can be applied to other nickel-based alloys as well as many stainless steels. The development and design purpose of the alloy shall be discussed.

The composition of Hastelloy B-2 is listed in Table 1 below. Hastelloy B-2 is a corrosion resistant Ni-Mo alloy that has good strength characteristics below 425 ^{o}C. It has good corrosion resistance to HCl and H_3PO_4 and is often used in environments where these solutions are present [2.6]. The alloy also has excellent chemical attack properties in the as-welded condition, with excellent resistance to heat-affected zone attack due to its resistance to forming grain-boundary carbides during welding [2.8]. Therefore, since the alloy is readily used after welding, it is a suitable model system for this welding investigation.

Table I – Alloy Composition in Weight Percent [2.6, 2.7]

Alloy	C	Co	Cr	Fe	Mn	Mo	Ni	P	S	Si
Hastelloy B-2	0.002	0.15	0.49	1.01	0.17	27.71	Bal.	<0.005	<0.002	0.02

Lienert et. al. have studied the solidification behavior and welding metallurgy of Hastelloy B-2. In their investigation, the hot cracking susceptibility was examined as well, the results showing that B-2 is very resistant to hot cracking [2.6]. Differential Thermal Analysis (DTA) was performed on the alloy to determine the solidification reaction temperatures for B-2; the results of which can be seen in Figure 2.4 and Table II below.

Table II – Reaction Temperatures from DTA Test of Hastelloy B-2 [2.6]

Reaction	Temperature, °C
Solidus (on heating)	1376
Liquidus (on heating)	1431
Liquidus (on cooling)	1404
$Ni_2Mo_3C^*$	1277

*Possible phase, not fully characterized at time of publication

Lienert et. al. found through microstructural analysis that the excellent hot cracking resistance was caused by the very small amount of secondary constituent (≈0.2 vol. %) in the microstructure. The hot cracking susceptibility has been shown previously to be directly related to the amount of secondary constituents [2.9]. Upon examining the solidification sequence, Lienert et. al. determined that the segregation of Mo dominates the microstructure, giving rise to the terminal eutectic-like constituent [2.6].

2.2 Solidification

It is imperative to have a solid grounding in the solidification sequence before one can understand the welding process. When an alloy or pure metal solidifies, there are two limiting types of solidification that bound all solidification conditions that can occur: equilibrium solidification and non-equilibrium solidification. Since the welding conditions to be studied only pertain to alloy systems, a simple two component system shall be used in explaining the solidification sequence. This description shall then be expanded to a ternary alloy system.

2.2.1 Equilibrium Solidification

Equilibrium solidification is the simplest case of alloy solidification. To obtain equilibrium solidification, the alloy must solidify sufficiently slowly to allow complete diffusion in both the solid and the liquid, giving a completely uniform solid upon final solidification. In practical applications equilibrium conditions are rarely reached due to the extremely long period of time required to attain complete diffusion in the liquid and solid states for substitutional alloying elements. However, for interstitial alloying elements the D_S term can be very high and equilibrium can be reached as is seen for carbon in one system [2.23]. The criterion for equilibrium solidification is:

$$L^2 << D_s t \qquad (2.1)$$

Where L is ½ the cell/dendrite arm spacing (or diffusion distance), D_s is the diffusion coefficient of the solute in the solid, and t is time [2.12]. Equation (2.8) illustrates the physical requirement for equilibrium solidification conditions to be met. L represents the furthest distance that atoms shall have to diffuse to eliminate any compositional gradients. D_s represents the rate of diffusion and t is the time that is available for diffusion to occur. If $D_s t$ is much less than L^2 then composition gradients will exist in the solid and equilibrium conditions have not been met. Even though it is not commonly encountered, it is still useful to study equilibrium solidification since it is the basis for all alloy solidification.

Consider the equilibrium binary alloy phase diagram as shown in Figure 2.5. The alloy of interest is that of composition X_O. The partition coefficient defined above in equation (2.1) is defined as:

$$k = \frac{X_S}{X_L} \qquad (2.2)$$

Where X_S is the composition of the solid and X_L is the composition of the liquid [2.10]. When using any equilibrium phase diagram, the relative amount of two phases can be calculated using the reverse lever law:

$$F_{L,S} = \frac{w_{S,L} - w_O}{w_{S,L} - w_{L,S}} \qquad (2.3)$$

Where $F_{L,S}$ is the fraction of liquid or solid and w represents the weight fraction of element B in either the solid or the liquid [2.11]. The reverse lever law can be derived from weight balances. It must always follow that:

$$F_S + F_L = 1 \quad (2.4)$$

which can be re-written as $$F_L = 1 - F_S \quad (2.4a)$$

and $$F_S = 1 - F_L \quad (2.4b)$$

If a weight balance for B atoms is created, the following can be written:

$$w_0 = F_L w_L + F_S w_S \quad (2.5)$$

where $w_{0,L,S}$ are the amounts of B in the whole system, the liquid, and the solid respectively. Combining equation (2.5) with equation (2.4a) gives:

$$w_0 = (1 - F_S)w_L + F_S w_S \qquad (2.6)$$

rearranging,

$$F_S w_S - F_S w_L = w_0 - w_L \quad (2.7)$$

and finally

$$F_S = \frac{w_0 - w_L}{w_S - w_L} \qquad (2.8)$$

A similar derivation can be performed for F_L [2.11].

For the model of equilibrium solidification it is assumed that the liquidus and solidus lines in Figure 2.5 are linear, and thus the partition coefficient is constant. Linear liquidus and solidus lines are not required for equilibrium solidification, they are assumed to simplify this illustration. Consider an alloy of composition X_O in Figure 2.5. As it is cooled from the liquid the first solidification is initiated at temperature T_1, where the liquidus is intersected. At this instant, the composition of the solid formed is kX_O. As the alloy is further cooled, the composition of the solid and liquid is uniform and is determined by the intersection of the tie line with the solidus or liquidus, respectively. Again, this is due to the complete diffusion in both the liquid and solid phases. Once the alloy has been cooled to T_3, the last liquid is solidified at composition X_O/k and the solid is homogeneous at composition X_O.

In this study only directional solidification is considered. In weld solidification, nucleation is eliminated at the fusion line since growth occurs directly off the base metal grains. However, with sufficient undercooling it is possible to nucleate dendrites in the weld pool center. The directional solidification creates a planar solid/liquid interface as seen in Figure 2.6. The compositions of the solid and liquid are given by the terms discussed above. The shaded regions of Figure 2.6 must be equal in area due to conservation of mass. After complete solidification in the volume element, the composition would be X_O and homogeneous along the entire length.

2.2.2 Non-Equilibrium Solidification

For many applications equilibrium solidification is not applicable since the time required to obtain complete diffusion is very long. In welding, cooling rates are from 10 to 10^3 Ks^{-1} for conventional arc processes while electron beam welding cooling rates are 10^3 to 10^6 Ks^{-1}, hardly equilibrium conditions [2.13]. However, it has been suggested that solid state diffusion becomes an important consideration when the following holds true:

$$\frac{s}{3} \leq \sqrt{Dt_S} \qquad (2.9)$$

Where s is the cell spacing, D is the diffusivity, and t_S is the local solidification time [2.9]. Diffusivity values for common systems can be seen in Table III. It is seen that for most elements the diffusivity in the solid is much less than the diffusivity in the liquid. The carbon diffusivity in the solid is seen to be many orders of magnitude higher than the others (except for S), indicating that it will be in equilibrium conditions for a wider range of cooling rates than those elements with lower diffusivities. Many non-equilibrium models attempt to deal with these situations and shall be reviewed below.

Table III- Diffusivity Values for Common Alloy Systems [2.14]

Alloy System (solvent-solute)	Liquid State Diffusivity ($10^{-9}m^2s^{-1}$)	Solid State Diffusivity ($10^{-9}m^2s^{-1}$)
Fe-C	7.9	5.8
Fe-Ni	4.8	0.0002
Fe-Si	3.8	0.024
Fe-S	4.5	0.16
Fe-C-Si	6.4 (for Si)	0.03 (for Si)
Fe-Ni-S	---	8 x 10^{-5} (for Ni)
Al-Cu	4.9	0.005
Cu-Ni	3.5	0.002

2.2.2.1 No Solid Diffusion, Complete Liquid Diffusion

In this case it is assumed that the solidification occurs too quickly to allow diffusion in the solid that is formed, but the liquid is mixed to allow homogeneous liquid composition. It is also assumed that there is negligible undercooling before and during solidification [2.15]. Assume an alloy bar of length x is directionally solidified, so that increasing x position corresponds to increasing the fraction of solid. Using the same phase diagram as before in Figure 2.5, the first solid to form is at temperature T_1 and composition kX_0 [2.9]. This composition is lower than X_0, so that solute is rejected into the liquid. Since there is no solid state diffusion, the solid composition does not change after solidification is complete. The composition of the liquid is continually enriched and a compositional gradient is induced on the solid as it forms out of the enriched liquid. This gradient can be seen in Figure 2.7, the composition versus position graph for the directionally solidified alloy bar. In Figure 2.7 it is seen that the solid/liquid interface composition increases with distance along bar x (increasing fraction solid) past the nominal alloy composition X_0 to X_{max}, where it then jumps to the eutectic composition

X_E [2.10]. Since there is no solid diffusion, the position along the bar indicates the composition of the solid/liquid interface at that point. At the point where the forming solid reaches the X_{max} composition, the remaining liquid solidifies as a eutectic reaction. This behavior is caused by the enrichment of the liquid due to solute rejection [2.9]. Since the alloy is assumed to have no solid diffusion, all solute rejected from the solid enriches the liquid. The liquid becomes richer in solute so it solidifies at lower temperatures, increasing the solidification range from T_1 to T_3 in the equilibrium case to T_1 to T_E (the eutectic temperature) in this case. Solidification is terminated at the eutectic temperature since the solid cannot dissolve any more solute and instantaneous freezing occurs.

The solute rejection causes a solidus depression in the equilibrium phase diagram, as seen in Figure 2.8. The average solid composition follows the dashed X_s line. The average solid is defined as the average composition of the solid formed thus far in the reaction. However, the solid/liquid interface must follow the equilibrium solidus since equilibrium conditions must be maintained at the solid/liquid interface. The compositions of the liquid and solid can be predicted for any point during solidification using the Scheil equations, otherwise known as the non-equilibrium lever rule [2.10]. Equating the amount of solute rejected when a small amount of solid forms to the liquid solute enrichment gives the following relation [2.12]:

$$(X_L - X_S)df_S = (1 - f_s)dX_L \quad (2.10)$$

where $X_{L,S}$ is the composition of liquid or solid respectively, and f_S is the fraction of solid formed. If this is integrated using $X_S = kX_O$ when $f_S = 0$ the Scheil Equations result:

$$X_S = kX_0\left(1-f_S\right)^{(k-1)}$$

(2.11 and 2.12)

$$X_L = X_0 f_L^{(k-1)}$$

Thus, for any fraction solid or liquid the composition of the solid and liquid can be calculated [2.9, 2.12, 2.15, 2.16].

2.2.2.2 No Diffusion in Solid, Solute Buildup in Liquid

In this case the cooling rate is sufficiently fast to prevent diffusion in the solid, and there is no mixing in the liquid. Thus, only diffusion can transport solute away from the solidification interface in the liquid. The solute rejected from the solid is therefore not moved from the solid/liquid interface until there is a large enough gradient to cause it to diffuse away from the interface into the liquid. This gradient is seen in Figure 2.9a. Since there is no mixing to evenly distribute the newly rejected solute, it "piles up" at the solid liquid interface. It follows that the solid composition rises quickly during this region due to the lack of diffusion in the liquid in contact with the forming solid. If the solidification occurs at a constant rate, a steady state region of solidification is reached when the temperature at the interface is T_3 in Figure 2.8. At this point, the solute rejected into the liquid is balanced by the amount of solute diffusing away from the interface (Figure 2.9b). This region continues until the width of the remaining liquid (i.e. distance between two solidifying bodies) is approximately the width of the solute gradient in the liquid. At this point the remaining liquid is enriched rapidly until the eutectic composition is reached and final solidification occurs [2.10]. The complete solidification composition profile is seen in Figure 2.9c.

2.2.3 Constitutional Supercooling

In the case above planar front solidification was assumed, while in practice this is found very rarely. It is much more common that the planar front breaks down into a cellular or dendritic solid liquid interface as a result of constitutional supercooling. Constitutional supercooling is a condition that arises from case 2.2.2.2 above. As the solute gradient is built up in front of the solid liquid interface, the temperature at which further solidification will occur decreases as indicated in Figure 2.8. This temperature corresponds to the line T_e in Figure 2.10. This temperature is fixed as defined by the equilibrium phase diagram, and only varies as a function of composition. The actual liquid temperature is not confined by such compositional parameters and can follow the line T_L. The slope T_L is the temperature gradient during the welding process and is controlled by the thermal conductivity properties of the liquid weld metal. The shaded region indicates where the actual temperature is below the liquidus temperature, and the melt is said to be constitutionally supercooled. Under these conditions, the shaded area is unstable in the liquid form and wants to solidify. It is this instability that causes the breakdown of planar front growth into the cellular/dendritic structure, which is discussed later.

It is important to get a physical understanding of constitutional supercooling since it defines the microstructural development of weld pools. It was mentioned above that the slope of T_L defines the degree of constitutional supercooling. If this slope is very shallow, a larger degree of supercooling shall exist and there will be a greater driving force for dendrites to form. It is possible to derive the criterion for planar front stability, and thus know when the transition to a cellular/dendritic structure is expected [2.12]. We must first define the gradient of the solute at the solid liquid interface:

$$\left(\frac{dX_L}{dx'}\right)_{x'=0} = -\frac{R}{D_L} X_L^*(1-k) \quad (2.13)$$

where x' is the position of the interface. Assuming a planar solid/liquid interface, the slope of line T_e in Figure 2.10 related to the liquid composition X_L by the slope of the liquidus line:

$$\left(\frac{dT_e}{dx'}\right)_{x'=0} = m_L\left(\frac{dX_L}{dx'}\right)_{x'=0} \quad (2.14)$$

T_L must have a shallower slope than $(d\,T_L/dx')_{x'=0}$ for constitutional supercooling to occur. Knowing this, combining equations (2.20) and (2.21), and allowing $X_s^* = kX_L^*$ gives the following planar front stability criterion:

$$\frac{G_L}{R} \geq -\frac{m_L X_0(1-k)}{kD_L} \quad (2.15)$$

Where G_L is the temperature gradient in the liquid, R is the growth rate of the cells, m_L is the slope of the liquidus, and D_L is the diffusion coefficient of the solute in the liquid [2.12]. Thus, when G_L/R is less than the above equation, the planar front breaks down to a cellular front.

Equation (2.15) shows how many allow and weld process variables affect microstructure evolution. G_L and R represent the weld process variables that directly control the microstructure. It is easily seen from equation 2.15 that if the growth speed R is decreased, or the temperature gradient G_L is increased planar front stability is increased. Thus, it is expected that for a given R, high energy density processes such as laser welding shall have more planar front stability than conventional arc processes since G_L is larger for laser welding. Conversely, it can be said that for a given temperature gradient, decreasing the growth speed will increase the tendency for planar front growth. While the growth speed cannot be directly controlled by the user, it is directly related to the weld process travel speed as will be shown later.

The materials properties that directly affect the planar front stability are the nominal composition X_o, liquidus slope m_l, partition coefficient k, and liquid diffusivity D_l. If the partition coefficient and diffusivity in the liquid are increased, the planar front solidification becomes more stable. This makes sense physically because higher diffusivity acts to decrease the solute gradient in the liquid, while a higher partition coefficient indicates less solute is rejected into the liquid (refer to equation 2.1). However, if the nominal alloy composition X_o and liquidus slope m_l are increased, the planar front solidification becomes less stable. As X_o increases, there is more solute in the alloy to be rejected into the liquid. This creates a larger gradient and thus larger tendency for undercooling. As m_l is increased, the liquidus temperature change for a given composition increment increases as well. This also acts to increase undercooling.

2.2.4 Ternary Solidification

Since the alloys to be studied are all very complex alloys, binary diagrams are not the most accurate way to describe the solidification sequences. While all the alloys have more than three elements, ternary phase diagrams are more accurate than binary phase diagrams while still being fairly easy to comprehend. Consider a phase diagram as shown in Figure 2.11 and an alloy of composition "a." Assuming Scheil conditions, the alloy will behave like the binary solidification case discussed above, from point a to point b solute shall be rejected from the solid into the liquid. However, since this is a ternary alloy, both B and C atom species shall be rejected into the liquid. Once point b is reached, mono-variant solidification occurs as the solidification path follows the two-fold saturation line towards the eutectic point. The solidification path does not cross this boundary into the β region because this would increase the temperature of the system. It is important to remember that this diagram is a "flattened" three dimensional image. It is handy to recall the analogy of water flowing downhill from section 2.1.2. The α and β phases solidify while C is rejected into the remaining liquid. At point c, the remaining liquid freezes to $\alpha + \beta + \gamma$.

The primary solidification path from point a to point b can be solved for by rearranging equation (2.12) for the fraction liquid:

$$f_L = \left(\frac{X_{L,A}}{X_{0,A}} \right)^{\frac{1}{K_A} - 1} \qquad (2.17a)$$

$$f_L = \left(\frac{X_{L,B}}{X_{0,B}} \right)^{\frac{1}{K_B} - 1} \qquad (2.17b)$$

for both elements A and B respectively. Since the f_L term is independent of atom species, (2.15a) and (2.15b) can be equated:

$$\left(\frac{X_{L,A}}{X_{0,A}} \right)^{\frac{1}{K_A} - 1} = \left(\frac{X_{L,B}}{X_{0,B}} \right)^{\frac{1}{K_B} - 1} \qquad (2.18)$$

Equation (2.18) can then be rearranged for either the $X_{L,A}$ or $X_{L,B}$ to give the primary solidification path:

$$X_{L,A} = X_{0,A}\left(\frac{X_{L,B}}{X_{0,B}}\right)^{K_A-1/K_B-1} \qquad (2.19)$$

It is seen that the partition coefficient has a strong effect on the solidification path of the alloy. In the case discussed above in figure 2.11, the $k_{\alpha B}$ value is low. Therefore there is a high degree of element B rejected into the liquid. As this liquid solidifies, the solid composition of B increases and thus the path heads towards the B end of the diagram. If the $k_{\alpha B}$ value was high, the tendency of B to segregate would be small. Therefore, the overall B composition of the primary solidification α region would stay relatively the same. Since the B composition doesn't change noticeably, the solidification path would tend towards the C end of the diagram as shown in Figure 2.11.

2.3.0 Non-Equilibrium Microstructures

Only non-equilibrium microstructures will be discussed since equilibrium solidification conditions are very rarely encountered in real life. These microstructures correspond to the solidification sequences described in sections 2.2.2.1 and 2.2.2.2 above. In welding conditions, the cooling rate is such that constitutional supercooling will almost always result. It is possible to create a cooling rate sufficiently fast that segregation free solidification occurs; this will be discussed later. Referring to Figure 2.10, there is always a variance in the liquidus temperature due to the solute buildup at the solid/liquid interface unless cooling occurs at almost infinitely slow rates. The slope of the line T_L, which corresponds to the actual temperature of the system, will give supercooling at all but the highest gradients. When an alloy solidifies in a region of constitutional supercooling, planar front solidification always breaks down into a cellular or dendritic structure. This is due to the fact that the liquid ahead of the solid liquid interface is constitutionally supercooled and will solidify preferentially to reduce its free energy. Thus, if a small perturbation on the interface grows ahead, it is in a supercooled region and will continue to grow. The solute rejected from the tip and sides of the protrusion depress the solidification temperature even more, and cause recesses to develop at the sides of the protrusion. These recesses in turn trigger more protrusions and the planar front is eliminated. The sequence of events can be seen in Figure 2.12. The regions between the protrusions are thus very rich in solute. This has been proven experimentally by Brooks and Baskes as seen in Figure 2.13 [2.17].

2.3.1 Types of Microstructures

There are two main types of non-equilibrium microstructures that will be discussed in this work: cellular and dendritic. The differences between the two and factors determining which shall prevail will now be discussed.

2.3.1.1 Cellular Microstructure

The cellular structure is the first to form from a planar solidification front. The structure is similar to long fingers of solid, as seen in Figure 2.14a. Transversely they look like a honeycomb (Figure 2.14b). The breakdown of planar front solidification occurs due to constitutional supercooling, discussed in detail in section 2.2.3. The development of the cellular microstructure can be related to two solidification parameters indirectly controlled by the user, the growth rate R and the temperature gradient G. The growth rate is controlled by the travel speed of the welding process, given by:

$$R = S\cos\theta \qquad (2.20)$$

where R is the growth rate, S is the travel speed, and θ is the angle between the welding direction and the growth direction of the cells. This states that the growth rate is never above the travel speed, and is often only a fraction of the travel speed. Thus, to get a large R value very high travel speeds are required. The temperature gradient can also be controlled by the welding process selected. Arc processes tend to have a lower temperature gradient than the higher energy density processes such as laser and electron beam welding. Thus, the temperature gradient can only be dictated by the welding process used. If a high gradient is required, a high energy density process (such as laser welding) should be used.

2.3.1.2 Dendritic Microstructure

The dendritic microstructure is very similar to the cellular, however the dendritic structure has arms or branches that come off the main trunk of the dendrite, reminiscent of a pine tree. The transition to dendrite growth occurs when the ratio G_L/R decreases. As the growth rate increases, crystallography starts to have an effect on the structure. Growth occurs along preferred directions (<100> in cubics) [2.12]. The actual transition is not truly defined but a gradual transformation, as seen in Figure 2.15.

The cooling rate, $\varepsilon = GR$, defines the spacing in both primary and secondary dendrite arm spacing. Thus, if one measures the dendrite arm spacing, they can calculate the cooling rate. This relationship is:

$$d = a\left(\frac{\Delta T_S}{GR}\right)^n = b(GR)^{-n} \qquad (2.21)$$

Where d is the dendrite arm spacing, a and b are constants, ΔT_S is the non-equilibrium solidification temperature range, and n is from 1/3 to 1/2 for secondary spacing or ½ for primary spacing [2.12]. In physical terms, this states that as G and R increase, the dendrite arm spacing decreases. Thus, to reduce the degree of microsegregation, one would want to increase G and R as much as possible. At a critical G/R ratio, the surface energy becomes too large and the dendritic solidification mode reverts to planar and microsegregation is eliminated.

2.3.2 Solidification Parameters that Affect the Microstructure

There are three user controlled variables in welding that affect the microstructure of the solidified weld. The growth rate R, temperature gradient G, and the amount of undercooling ΔT all effect the microstructure.

2.3.2.1 Growth Rate

The growth rate is the rate at which the solid liquid interface advances, and is directly related to the welding speed [2.13]. In steady state welding conditions, the weld pool has a constant shape as that shown in Figure 2.16. It is clear that the growth rate will change relative to location in the weld pool. At the center of the fusion zone R is maximized due to the interface being perpendicular to the welding direction [2.17]. However, at the edge of the fusion zone the growth rate shall be minimized due to the interface being parallel to the welding direction. The growth rate can be calculated from the following relation:

$$|R_S| = |R_H| \cos\theta \qquad (2.22)$$

Where R_S is the growth rate, R_H is the heat source rate (travel speed), and θ is defined as the surface normal as seen in Figure 2.16 [2.13].

Since the G/R ratio in welding almost exclusively forces cells or dendrites to form, the crystallographic orientation of the solidification front must be considered. At such cooling rates the dendrites grow along easy growth directions as mentioned previously. Since most materials to be joined by welding are polycrystalline, some grains of the base metal shall be oriented more preferably than others. The grains with orientations closest to the easy growth directions shall grow faster than grains with larger misorientations. The dendrite growth rate can be calculated by:

$$|R_{hkl}| = |R_H| \frac{\cos\theta}{\cos\psi} \qquad (2.23)$$

Where R_{hkl} is the growth rate of the dendrite, and Ψ is defined in Figure 2.17 [2.13, 2.18, 2.19].

The growth rate has a strong influence on the solute redistribution in the weld pool solidification. Burden and Hunt have shown that increasing the growth rate will decrease the dendrite tip temperature, thus increasing dendrite core compositions by inducing the tip undercooling [2.20]. If one looks at the phase diagram in Figure 2.5, any decrease in the solidification temperature of a hypoeutecic alloy will increase the initial solid composition. Increasing the growth rate also decreases the stability of a planar growth front. From their study in the Al-Cu system, Burden and Hunt found the breakdown from a planar to cellular interface was reported to be between 1×10^{-4} and 2.8×10^{-4} cm/sec, holding the liquid temperature gradient at 60 ^{o}C/cm [2.20]. These numbers are dependent on alloy system since all elements have different diffusivities and

m_l values, however it is still useful to illustrate the extremely slow growth rates required for planar stability.

2.3.2.2 Thermal Gradient

The thermal gradient of the liquid G_L plays an important role in determining the microstructure in the fusion zone. G_L is affected by the thermal properties of the base metal and is proportional to the heat flux in the liquid and can be either positive or negative. It is positive (i.e. heat flows from the fusion zone into the base metal) for normal welding conditions but can be negative when the weld pool is thermally undercooled [2.13]. In relation to materials properties, the thermal gradient increases as the conductivity decreases. From the classical Rosenthal solution, the thermal gradient at the tail of the weld pool is approximated to be:

$$G \cong \frac{2\pi\kappa}{\eta_t P}(T_M - T_0)^2 \quad (2.24)$$

Where κ is the thermal conductivity, η_t is the transfer efficiency, P is the power of the heat source, T_M is the melting temperature, and T_0 is the temperature of the plate far away from the weld [2.18].

Contrary to the growth rate, the thermal gradient is minimized at the weld centerline and maximized at the edge of the fusion zone. This is due to the cold base metal touching the edge of the fusion zone extracting heat much more quickly than the centerline's just solidified metal.

As shown in Figure 2.18 for an Al-2 wt% Cu alloy, for a given growth rate the dendrite tip temperature decreases with increasing thermal gradient. If the tip temperature is lower, the amount of undercooling is increased and the dendrite core composition will increase [2.20]. This shall be discussed in the section below.

2.3.2.3 Undercooling

Undercooling refers to the difference between the liquidus temperature and the actual liquid temperature at the dendrite tip. In general, the relative amount of undercooling increases with the solidification rate. This undercooling can be broken up into four terms:

$$\Delta T = \Delta T_{TH} + \Delta T_C + \Delta T_R + \Delta T_K \qquad (2.25)$$

Where ΔT_{TH} represents the thermal undercooling, ΔT_C is the constitutional undercooling, ΔT_R is the undercooling due to curvature of the solid liquid interface, and ΔT_K is the kinetic undercooling [2.13, 2.19. 2.21]. The kinetic term is associated with the driving force needed for solidification to proceed and is often ignored since it is typically less than 1 K [2.13].

A much more significant term is the undercooling due to tip curvature [2.9]. The solidification temperature is dropped to compensate for the additional surface energy associated when forming a curved interface. This can be described quantitatively as:

$$\Delta T_R = \phi K \qquad (2.26)$$

Where Φ is the Gibbs-Thomson coefficient and K is the tip curvature. Since the G/R ratios in welding promote dendrite solidification, the tip radius term can be significant. The thermal undercooling term is not significant in welding as it represents the temperature difference of the liquid and the equilibrium freezing temperature. It is significant in casting operations where a nucleation barrier is often present, but in welding solidification nucleation plays a very minor role. Since there is always base metal present, growth occurs from the base metal grains at the fusion line, eliminating the need of nuclei formation. However, David and Vitek reported that in rapid solidification conditions such as those in laser beam welding it is possible for thermal undercooling to exist and be on the order of hundreds of degrees K [2.13]. Under most welding conditions the ΔT_C and ΔT_R term are the most significant undercoolings and have been discussed previously.

Physically the undercooling of the weld pool can lead to what is known as "partitionless" solidification. Under extremely high cooling rates and undercoolings only seen in rapid solidification processes (such as laser or electron beam welding) equilibrium in not maintained at the solid liquid interface. The solidification may take place so fast as to inhibit any diffusion at all and thus the solid has the same composition as the liquid and k=1 [2.13]. Such situations can be quite appealing as the degradation in physical properties due to microsegregation can be avoided [2.14].

2.3.3 Alloy Parameters That Affect the Microstructure

Along with weld processing parameters that effect the microstructure, there are inherent materials properties that affect the microstructure of a weld. Namely, these are the partition coefficient k, the liquidus slope m_L, and the liquidus temperature.

2.3.3.1 Partition Coefficient

The partition coefficient, k, is always less than 1 for the hypoeutectic alloys to be studied in this work. This is obvious from its definition given above, where $k=X_S/X_L$. Since the composition of the solid is always less than that of the liquid, hence $k<1$. Partition coefficient values for common alloy systems are seen in Table IV below. However, the magnitude of k has a strong influence on solidification microstructures in that it determines the relative amount of microsegregation [2.9]. If k is small (below 1), then the liquid composition is much higher than the solid. This means that the liquidus is relatively far from the solidus, and thus the solidification temperature range is large as shown in Figure 2.19a. If k is close to 1, then the liquidus and solidus lines must be close together (see Figure 2.19b). Also, since there is much less tendency for the solute to enrich the liquid, the solidification temperature range is much smaller. This can be easily seen with the aid of Figure 2.5. If the liquid composition is not enriched with a significant solute, there is very little liquidus (and solidus) temperature depression. This of course translates into a smaller solidification temperature range. Thus, for k approximately equal to 1 the microsegregation is less than for low k values [2.9, 2.14]. The liquidus (and solidus) slope also plays a role, but shall be discussed later.

The solidification temperature ranges discussed above are for equilibrium solidification. However, welding has been shown to be a non-equilibrium process. The k term (along with X_0 and X_e) then defines the relative amount of liquid left at final solidification. For the low k value alloy, the equilibrium solidification range is larger than that of the higher k value alloy. Thus, the k term gives an indicator of the amount of microsegregation in an alloy. High k value materials shall be more homogeneous due to the proximity of the liquid and solid compositions compared to lower k value alloys [2.9]. To illustrate this concept, Figure 2.20 is useful. In this figure, composition profiles are calculated via the Scheil equation for the solid. Both curves solidify under the same conditions and have the same initial composition ($X_0 = 0.05$ solute) and eutectic composition ($X_e = 0.1$ solute), the only difference being the value of the partition coefficient. The curve with the high partition coefficient ($k = 0.9$) shows much less variation in composition from the cell core to the boundary than the low partition coefficient ($k=0.3$) curve. It is noticed that for this alloy the low k curve has a flat region at approximately $f_S \approx 0.9$ and solid composition $X_S = 0.1$. This corresponds to the eutectic point of the alloy, thus all remaining liquid solidifies and the solid composition does not vary. The low k curve shows that not only does the composition vary drastically, but there is a significant amount (≈10%) of eutectic formed. In contrast, the high k curve shows much less compositional variation and very little eutectic formation.

Table IV – Partition Coefficient Values for Common Alloy System [2.14]

Alloy System	Partition Coefficient
(Solvent-Solute)	
Fe-C	0.24
Fe-Ni	0.90
Fe-Si	0.86
Fe-S	0.014
Fe-C-Si	1.4 (Si)
Fe-Ni-S	1.2 (Ni)
Al-Cu	0.145
Cu-Ni	2.7

2.4 Solidification Models

Numerous models have been put forth attempting to predict weld microstructures. The most popular shall be summarized and their accuracy assessed.

2.4.1 Scheil Model

The Scheil model was mentioned previously as a method to predict the amount of eutectic and composition of liquid and solid phases during non-equilibrium solidification. In this model, a volume element as seen in Figure 2.21 is used. In this volume the surface is assumed flat with no curvature, so that plane front solidification results. Along with the equilibrium model, the Scheil model acts as a boundary for solidification conditions. All other model predictions fall between the equilibrium and Scheil models conditions. This is due to the assumptions of the Scheil model.

They are:

1) Negligible undercooling exists
2) No mass flow in or out of the volume element studied
3) Diffusion in the liquid is complete

4) The partition coefficient k is constant throughout the solidification range

5) There is negligible solid diffusion [2.15]

Assumption 1 is accurate for welding conditions since the weld pool borders the base metal. The base metal grains act as nucleation sites for the solidifying weld pool so undercooling to initiate solidification is not needed. During growth, it is assumed that there is no undercooling so that equilibrium is maintained at the solid/liquid interface. The presence of cells or dendrites in the microstructure indicates that constitutional supercooling does exist, however to simplify the model we are only concerned with a small volume element where planar front growth occurs. The volume element for this case is shown in Figure 2.21. Assumption 2 is made to simplify calculations by eliminating flux in and out of the volume element. In reality flow can occur due to convection in the weld pool [2.15]. Assumption 3 is valid for welding; the weld pool is mixed due to agitation from the welding process. However, there is always a stagnant boundary layer next to the solid that does not mix due to fluid dynamics [2.22]. There will be solute buildup in this layer. Assumption 4 is made to simplify the math of the model. The accuracy depends on the alloy system's phase diagrams. Assumption 5 is also valid for normal welding conditions since the cooling rate is fast enough to prevent solid diffusion for substitutional alloying elements. Alloy elements that are interstitial (such as carbon) CAN diffuse fast enough to approach equilibrium conditions under certain conditions [2.23].

The Scheil model does a good job at approximating solidification behavior for most systems at intermediate cooling rates, however it does not predict behavior correctly for slow or rapid solidification. This deviation has been attributed to dendrite tip undercooling and solid diffusion [2.9, 2.21]. Thus, it can be seen that assumptions 1 and 5 above are incorrect for certain conditions. At slower rates of solidification, there is time for a degree of solid state diffusion to occur thus increasing the solid composition in solute. This is supported experimentally in the Al-Cu system as evidenced by Brooks and Baskes work. Using the Scheil equation, predicted copper dendrite core compositions were consistently half as much as those measured (0.34 wt% calculated versus 0.75 wt% measured) [2.9]. Brooks states that the solid diffusion is controlled mostly by the diffusivities of the alloying elements rather than the solidification parameters [2.9]. According to Brody, solid diffusion becomes a factor in composition calculations when:

$$\frac{s}{3} \leq \sqrt{Dt_S} \qquad (2.31)$$

Where s is the secondary dendrite arm spacing, D is the diffusivity of the solute in the solid, and t_s is the solidification time [2.9].

The Scheil Equation also fails to predict the compositions of the solidified weld pool for rapidly solidified melts. In rapid solidification rates, the dendrite tip radius decreases effectively decreasing the amount of segregation [2.9]. For rapidly solidified conditions, the D_s effect is eliminated. Brooks and Baskes have proven this to be true in the Al-Cu system, where they credit most of the Cu enrichment of dendrite cores to tip undercooling instead of solid diffusion [2.17]. If one looks to the solidification sequence described in section 2.2.2 above it is seen that constitutional supercooling will force higher solute concentrations in the dendrite cores. Due to the solute buildup in front of the dendrite, the tip is solidifying at a richer composition than that predicted by the Scheil model. Battle points out that the assumption of a planar interface in the volume element is not physically correct and can lead to error, however it often works relatively well [2.14].

2.4.2 Burden and Hunt Model

The Burden and Hunt model attempts to account for some of the shortcomings of the Scheil model by predicting dendrite tip temperature as a function of growth velocity and temperature gradient. The Burden and Hunt model accounts for diffusion along the length of the dendrite in the liquid region between the dendrites [2.24]. The Burden and Hunt Model assumes:

1) The dendrite tip can be approximated by a smooth shape
2) Temperature varies only along the length of the dendrite

Assumption 1 is seen to be valid when the microstructure in Figure 2.22 is examined. Assumption 2 is also valid under experimental conditions where the thermal gradient is controlled along the length of the dendrite.

Before the model is discussed, it is important to define two parameters, the peclet number p and the curvature undercooling constant θ. The peclet number is defined as:

$$p = \frac{VR}{2D_L} \qquad (2.32)$$

Where V is the velocity, R is the dendrite tip radius, and D_L is the diffusivity of the solute in the liquid [2.25].

The curvature undercooling constant θ is defined as:

$$\theta = \frac{V^{\alpha}\sigma}{\left(\overline{S}_A^{\alpha} - \overline{S}_A^{L}\right)\left(1 - C^{\alpha}\right) + \left(\overline{S}_B^{\alpha} - \overline{S}_B^{L}\right)C^{\alpha}} \qquad (2.33)$$

Where V^{α} is the molar volume of α, σ is the surface energy, C^{α} is the B atom fraction in the α phase. $\overline{S}$ is the partial molar entropies of components A or B where α or L refers to solid or liquid respectively [2.25]. This term indicates the relative amount of undercooling associated with the curvature of the interface.

The model attempts to predict the dendrite tip temperature, which the author's compare to experimental data obtained from the Al-Cu system. By growing an interface in steady state growth across a thermocouple Burden and Hunt were able to accurately measure the tip temperatures for varying growth rates. The temperature is seen to increase and then decrease with increasing growth velocity (Figure 2.23) [2.20]. The dendrite tip temperatures were also measured at different thermal gradients, and the temperature is seen to decrease with increasing thermal gradient as shown in Figure 2.18. Two models were proposed, a general model utilizing a Zener approach:

$$\Delta T = T_0 - T_{ID} = \frac{GD}{V} + BV^{n} \quad (2.34)$$

Where T_0 is the liquidus temperature, T_{ID} is the tip temperature, G is the temperature gradient, D is the diffusion coefficient, V is the tip velocity, B is a constant and n is 0.5. The "more accurate" model (as corrected by Tassa and Hunt) is seen to be:

$$\Delta T = \frac{GD}{V}\left[1 - \frac{K\phi}{1 - \phi(1-K)}\right] - \frac{m(1-K)C_{\infty}\phi}{1 - \phi(1-K)} + \frac{\theta V}{pD}\,\frac{\phi N/4p - \phi(1-K)}{1 - \phi(1-K)} \quad (2.35)$$

Where K is the partition coefficient, ϕ is defined as $pe^{p}E_{I}(p)$ (where E_I is the integral exponential function), m is the liquidus slope (defined as negative), C_{∞} is the composition at infinity, and N is approximately 4 [2.25, 2.26].

The Burden and Hunt models show decent agreement for the qualitative analysis but rather poor agreement for the "more accurate" model [2.26]. Fluid flow around the dendrite tip (which is not accounted for in the models) was proposed as a cause for the discrepancy with experimental results. In the experiment by Tassa and Hunt, dendrites were grown vertically. Since Cu was rejected into the liquid (which has a densifying effect), the heavier liquid flows in-between the dendrites aiding diffusion and causing the dendrites to grow at a higher temperature. Thus, when the dendrite tip is far away from the solid liquid front fluid flow leads to a higher tip temperature than that proposed by the model [2.26]. Laxmanan reports that the dendrite radius of curvature equation shows no dependence on the temperature gradient, while in reality the temperature gradient should increase the radius of curvature to increase the area dissipating heat and solute [2.27]. The main drawback in the Burden and Hunt models is that they assume a constant temperature gradient throughout the solidifying liquid, which is clearly not the case [2.28]. The temperature gradient along the edge of the fusion zone is much different from the temperature gradient at the weld centerline.

2.4.3 Esaka and Kurz Model

The Esaka and Kurz model consists of three models that also deal with directional dendrite solidification. The models were derived from studies in the aluminum 2 wt% copper system. Model I assumes:

1) a needle shaped crystal with constant cross section

2) a hemispherical tip

3) the term accounting for tip curvature is negligible

4) marginal tip stability applies [2.29]

The growth velocity is then given by:

$$V = \frac{C'}{R^2} \qquad (2.36)$$

Where

$$C' = \frac{4\pi^2 D\Gamma}{k\Delta T_0} \qquad (2.37)$$

V being the growth velocity, R is the tip radius, D the diffusion coefficient of the solute in the liquid, Γ the Gibbs-Thomson parameter, and ΔT_0 the equilibrium melting range. By graphing the Peclet number (described previously) versus the growth rate, Esaka and Kurz are able to assess the validity of their models applied to the Al-2wt% Cu system as seen in Figure 2.24. Below a critical V planar front solidification prevails and the Peclet number approaches infinity. However, Model I does not share this behavior due to the assumption of the hemispherical tip. At high velocities Model I also fails due to deviations from experimental data [2.29].

Model II assumes a parabolic tip instead of a hemispherical as in Model I (holding all other assumptions the same). The final form of Model II states that:

$$V^2 - \frac{DP^2 m(1-k)C_0}{\pi^2 \Gamma [I_v(P)(1-k)-1]} V + \frac{D^2 P^2 G}{\pi^2 \Gamma} = 0 \qquad (2.38)$$

Where P is the Peclet number, m is the liquidus slope, C_0 is the initial alloy composition, and $I_v(P)$ is the Ivantsov function. This model is much more accurate than the first and is applicable to dendritic growth in intermediate growth rates. At high growth rates (when marginal stability breaks down or the limit of absolute stability has been reached) Model II fails. Marginal stability is defined by Laxmanan to be the radius of the dendrite tip corresponding to the smallest wavelength at the onset of planar instability [2.30].

The most complex model was developed by Trivedi and accounts for capillary effects. Model III is defined as:

$$\frac{GD}{Vk\Delta T_0}+\frac{\Gamma VL}{2D\Delta T_0 kP^2}-1=\frac{(1-k)I_v(P)}{1-(1-k)I_v(P)}F(P) \qquad (2.39)$$

Where L = 28 for most cases and F(P) is given by Trivedi in the Journal of Crystal Growth volume 49. Models II and III are seen in Figure 2.24 to correspond fairly well, with the deviation caused by the accounting of harmonics and perturbations in Model III. Model III also shows the greatest agreement with Burden and Hunt's results for minimum undercooling conditions.

2.4.4 Kurz , Giovanola, and Trivedi Model

The Kurz, Giovanola, and Trivedi (KGT) model attempts to explain directional solidification at high growth rates. The model attempts to predict how microstructural features change with growth velocity and account for changes in the diffusion coefficient due to large undercooling caused by high growth rates [2.31]. The KGT model includes stability criterion that accounts for the surface tension that acts to stabilize the growth interface at high velocity. According to Langer and Muller-Krumbhaar directionally solidified dendrites grow in a marginally stable state where the dendrite tip radius, R, can be defined as:

$$R = \lambda_s \qquad (2.40)$$

where λ_s is the critical wavelength of the solid-liquid interface at the limit of stability [2.32]. From Mullins and Sekerka, the wavelength of a stable plane front is defined as [2.33]:

$$\omega^2 \Gamma = mG_c \xi_c - G \qquad (2.41)$$

with $\omega = 2\pi/\lambda_s$ and

$$\xi_c = 1 - \frac{2k}{\left\{1 + \left[\frac{4\pi D}{(\lambda_s V)}\right]^2\right\}^{1/2} - 1 + 2k} \qquad (2.42)$$

Γ is the Gibbs-Thomson parameter (defined as the ratio of the specific liquid-solid interface energy to the melting entropy), m is the liquidus slope, G_c is the liquid concentration gradient of solute at the interface, G is the temperature gradient at the interface, k is the partition coefficient of the alloy, D is the liquid diffusion coefficient and V is the interface velocity.

The equation for ξ_c can be re-written with the definition of the Peclet number as P=RV/2D to be:

$$\xi_c = 1 - \frac{2k}{\left[1 + (2\pi / P)^2\right]^{1/2} - 1 + 2k} \qquad (2.43)$$

and from above

$$R = 2\pi \left[\frac{\Gamma}{mG_c \xi_c - G}\right]^{1/2} \qquad (2.44)$$

Equation 44 can be reduced to

$$\xi_c = \frac{\pi^2}{kP^2} \qquad (2.45)$$

for high Peclet numbers (defined as $P > \pi^2/\sqrt{k}$). If this value for ξ_c is substituted into equation 2.45 with G=0 the absolute stability condition is found.

The model is defined as:

$$V^2A + VB + C = 0 \qquad (2.46)$$

Where V is the interface velocity, A is defined as:

$$A = \frac{\pi^2\Gamma}{P^2D^2} \qquad (2.47)$$

B is equal to:

$$B = \frac{mX_0(1-k)\xi_C}{D[1-(1-k)I_v(P)]} \qquad (2.48)$$

and

$$C = G \qquad (2.49)$$

For large growth rates the Peclet number is high ($P > \pi^2/\sqrt{k}$) and ξ_C is defined as:

$$\xi_C = \frac{\pi^2}{kP^2} \qquad (2.50)$$

The dendrite tip radius can be calculated using the equation:

$$R = 2\pi\left[\frac{\Gamma}{mG_C\xi_C - G}\right]^{\frac{1}{2}} \qquad (2.51)$$

Where G_C is the concentration gradient at the liquid interface and G is the mean temperature gradient at the interface [2.31]. The dendrite tip radius was plotted versus growth rate and it is seen in Figure 2.25. The radius decreases until a critical growth rate is reached where dendrite solidification is not stable and a planar front again takes over.

To account for temperature dependence of the diffusion coefficient, the following equation is substituted above for D:

$$D = D_0 e^{\left[-Q/R_g T\right]} \qquad (2.52)$$

Where Q is the activation energy and R_g is the gas constant [2.31].

In all previous models it was assumed that the partition coefficient was constant. While this is a valid assumption for some systems, during rapid solidification this is often not the case [2.34]. The partition coefficient is seen to vary as:

$$k = \frac{k_0 + (a_0 V / D)}{1 + (a_0 V / D)} \qquad (2.53)$$

Where k_0 is the equilibrium partition coefficient and a_0 is a length scale related to the interatomic distance.

The KGT model predicts the sharp increase in dendrite tip radius at the stability limit, which agrees with previous experimental results. The model is also accurate during slow growth velocities, corresponding well with the results put forth by Langer and Muller-Krumbhaar. To model laser beam welding, the KGT model is the most accurate due to the ability to vary the partition coefficient, an important consideration in rapid solidification processes.

2.5 Summary

Welding is one of the most important joining processes available today. The development of electron and laser beam welding ensures that the welding process shall be used in the future for high technology joining problems. To better understand the welding process, an overview of the solidification sequence in binary and ternary alloy systems was summarized. The microstructures produced and the process and materials parameters that effect the microstructures were reviewed. It was seen that as the growth rate and temperature gradient increase, the relative amount of undercooling increases as well. As the undercooling increases, the relative amount of solute segregation decreases and can be eliminated all together in partitionless solidification. If an alloy has a low partition coefficient the degree of microsegregation will be severe. The KGT model was selected as the most accurate for the laser beam welding to be studied.

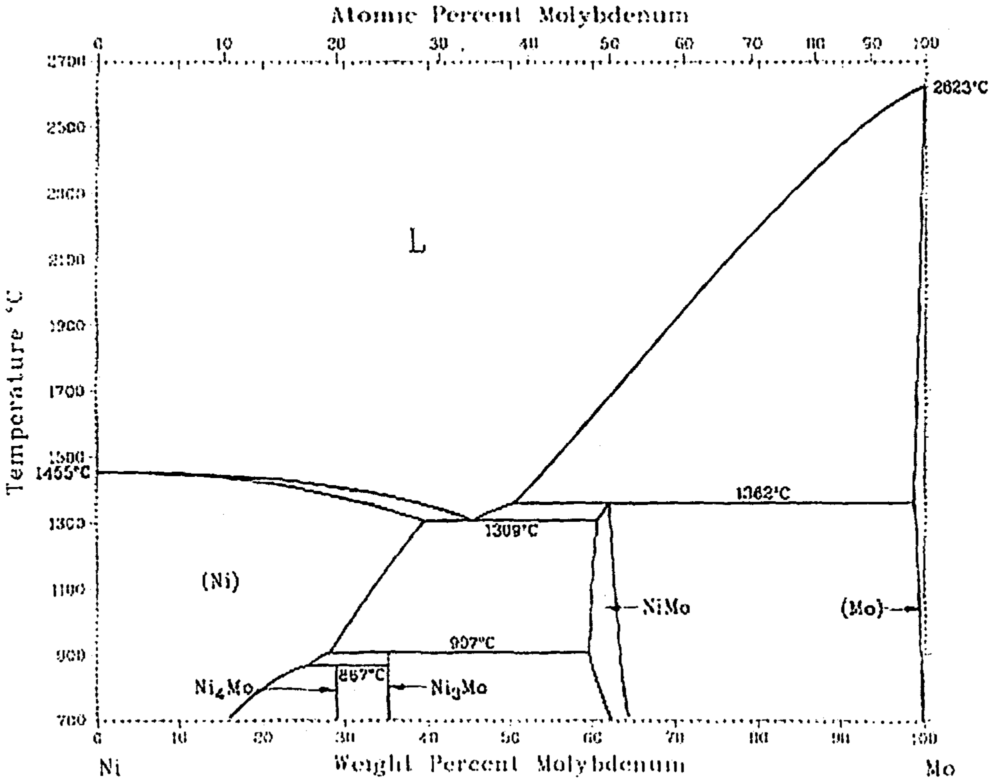

Figure 2.1 – Ni-Mo binary phase diagram [2.1].

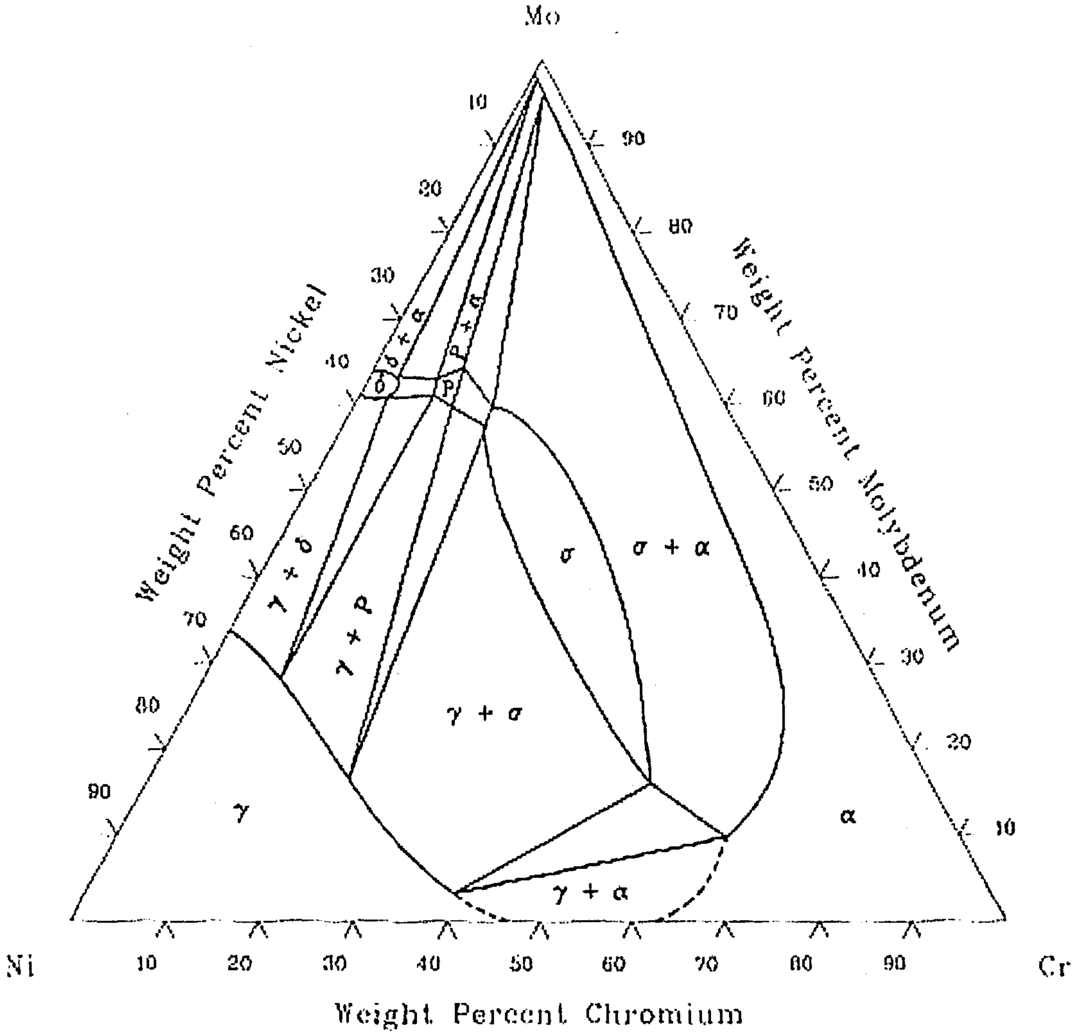

Figure 2.2 – Ni-Mo-Cr ternary phase diagram [2.2].

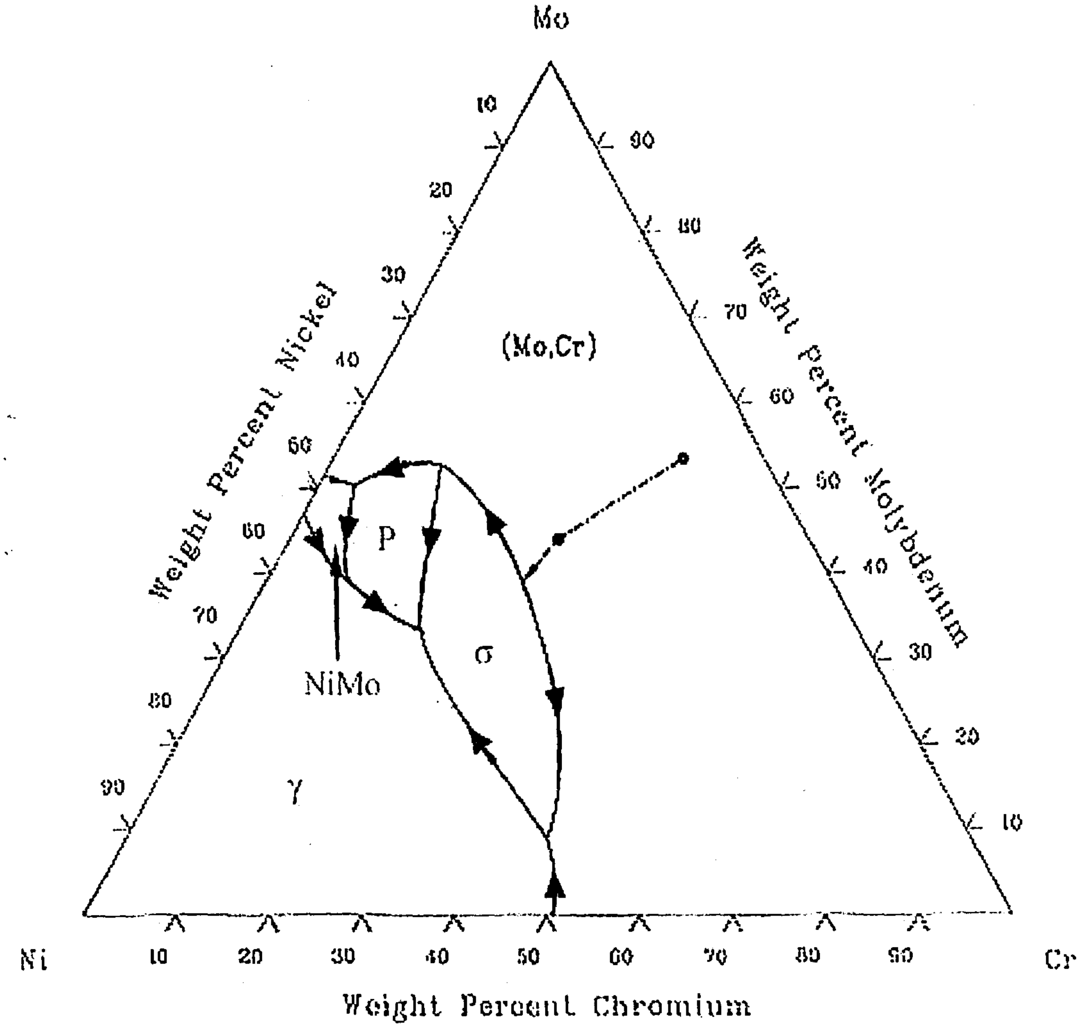

Figure 2.3 – Cr-Ni-Mo liquidus projection [2.5].

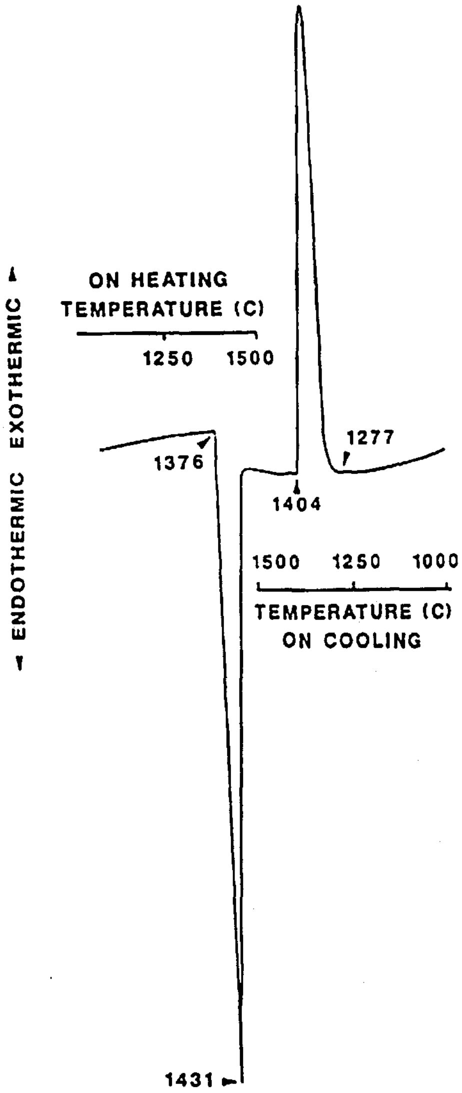

Figure 2.4 – DTA trace for Hastelloy B2.

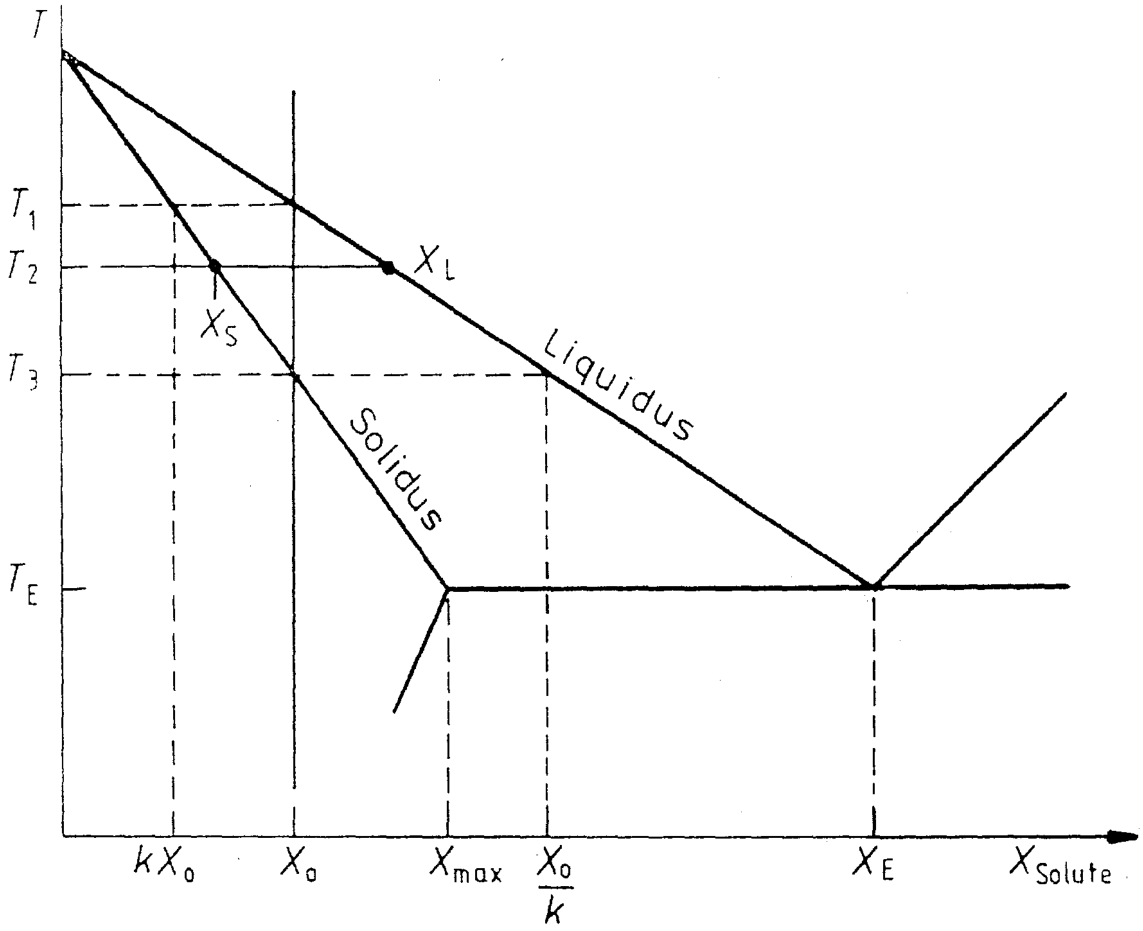

Figure 2.5 – Equilibrium binary phase diagram [2.10].

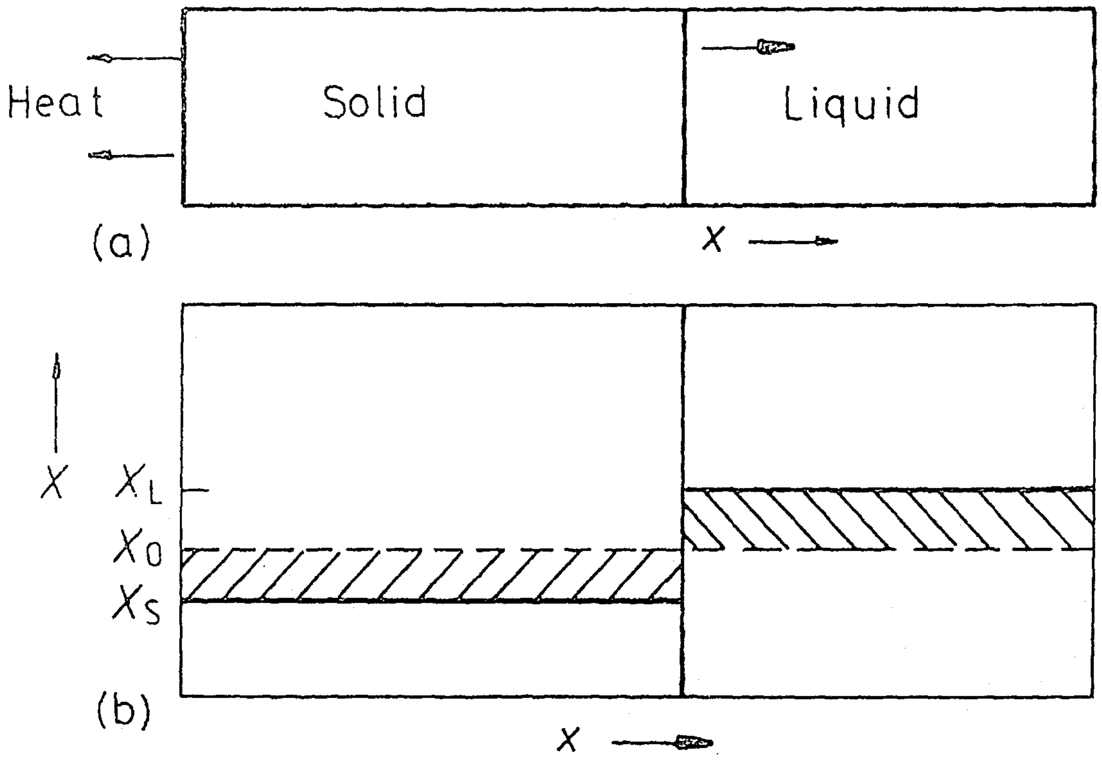

Figure 2.6 – a) Schematic of directionally solidified bar. b) Profile along bar showing solid and liquid composition [2.10].

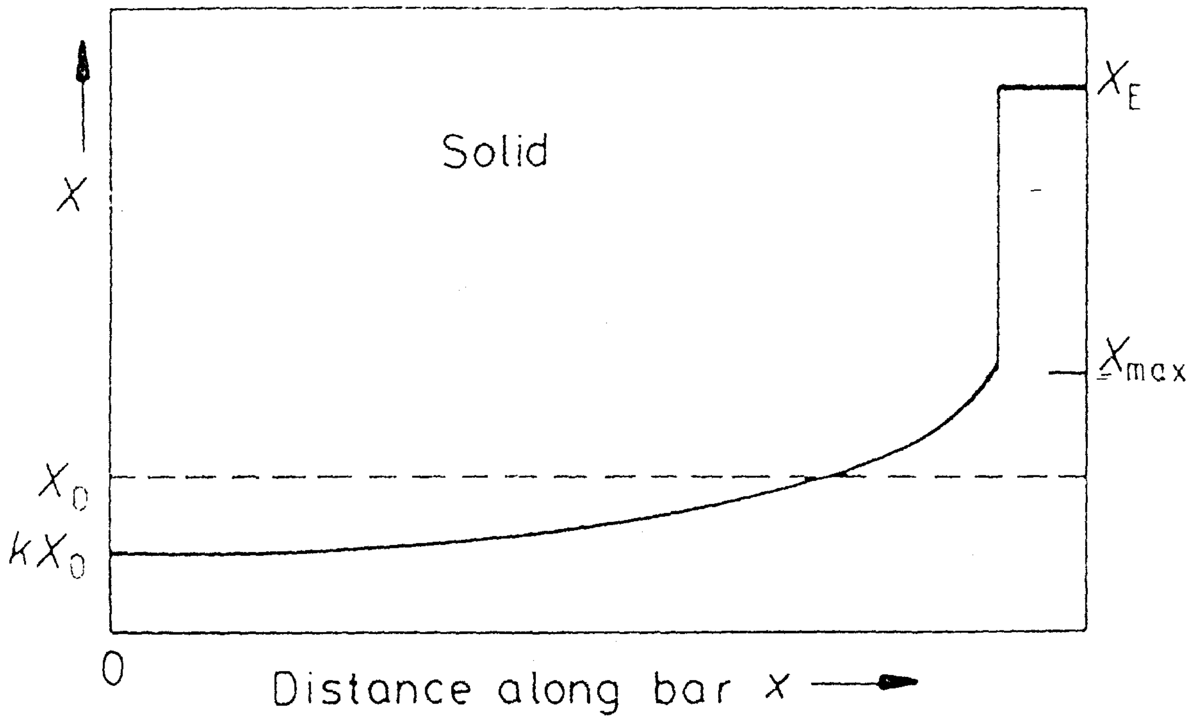

Figure 2.7 – Profile along directionally solidified bar for no solid diffusion, perfect mixing in liquid [2.10].

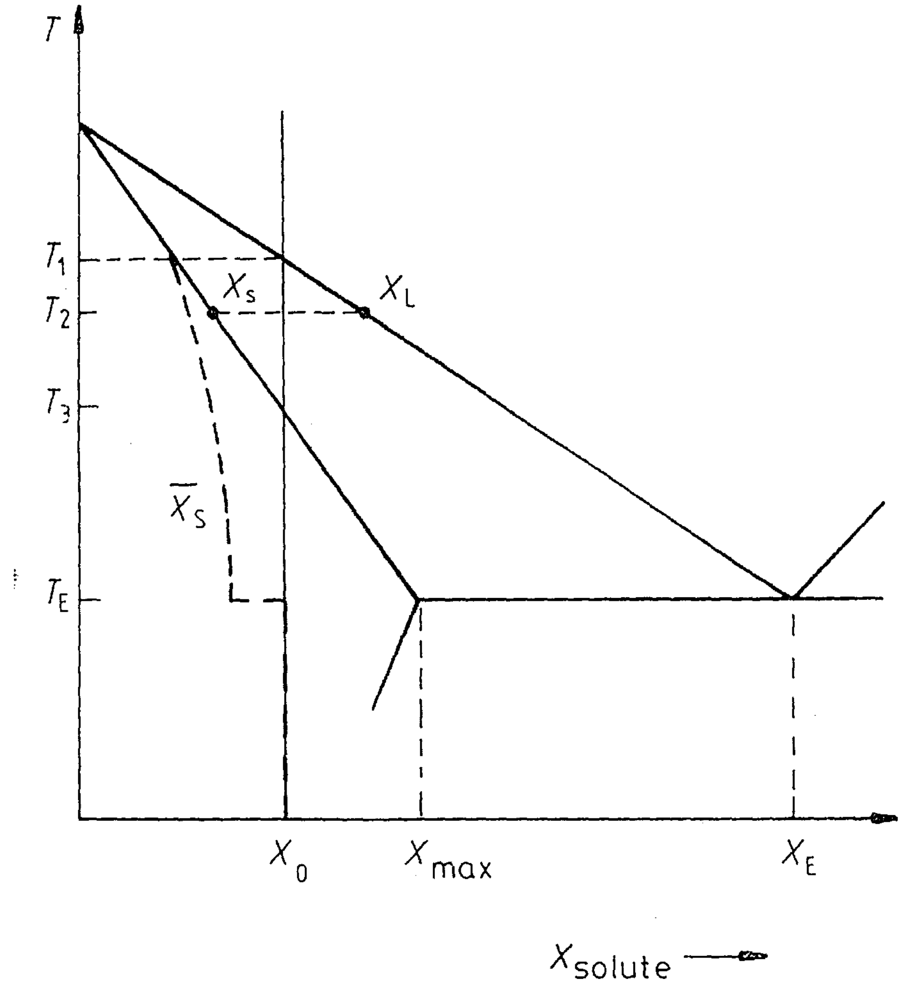

Figure 2.8 – Equilibrium phase diagram illustrating average solid composition (dashed line) during non-equilibrium solidification [2.10].

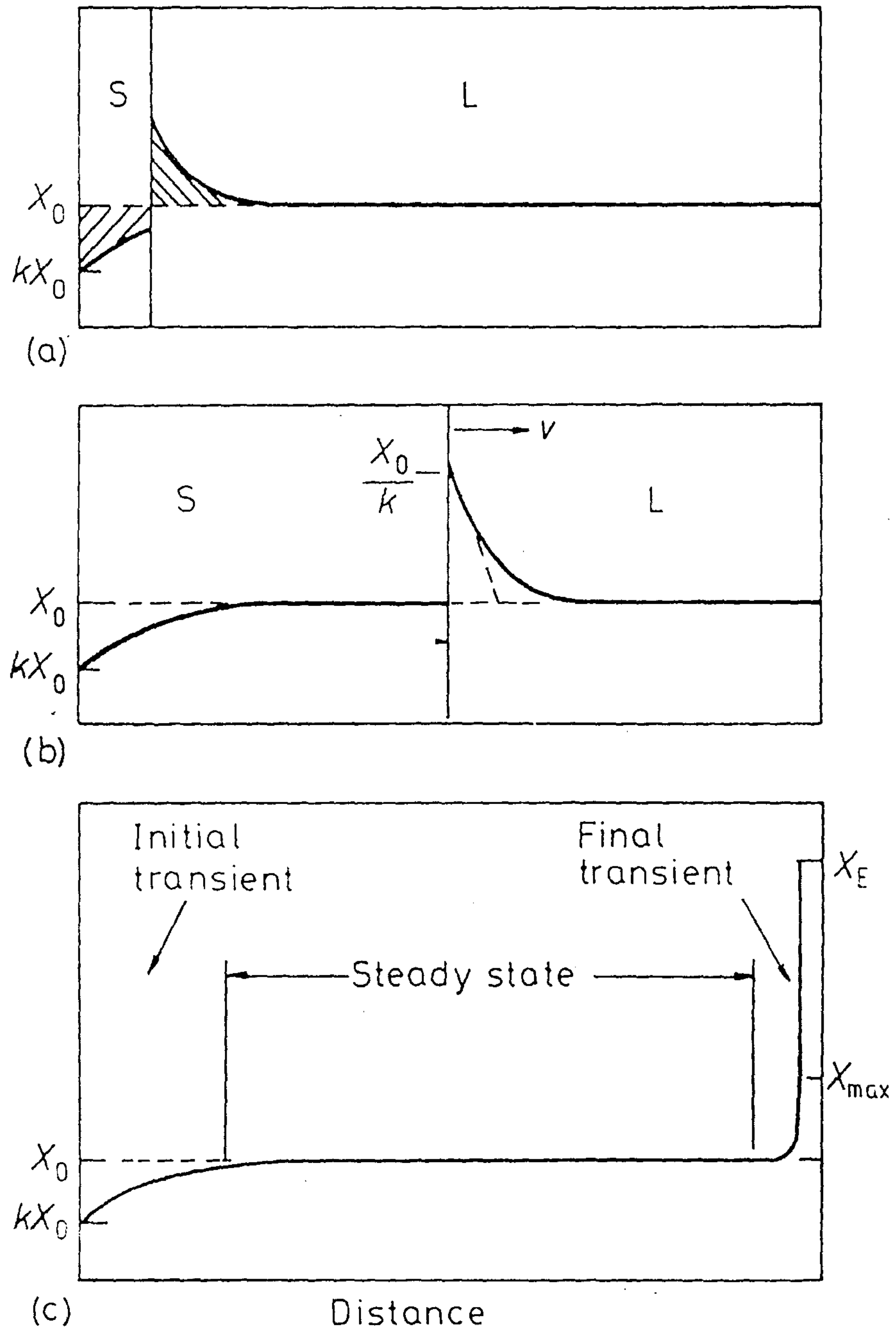

Figure 2.9 – a) Beginning of solidification illustrating solute gradient buildup. b) Steady state conditions of solute gradient in liquid. c) Final composition trace across length of sample [2.10].

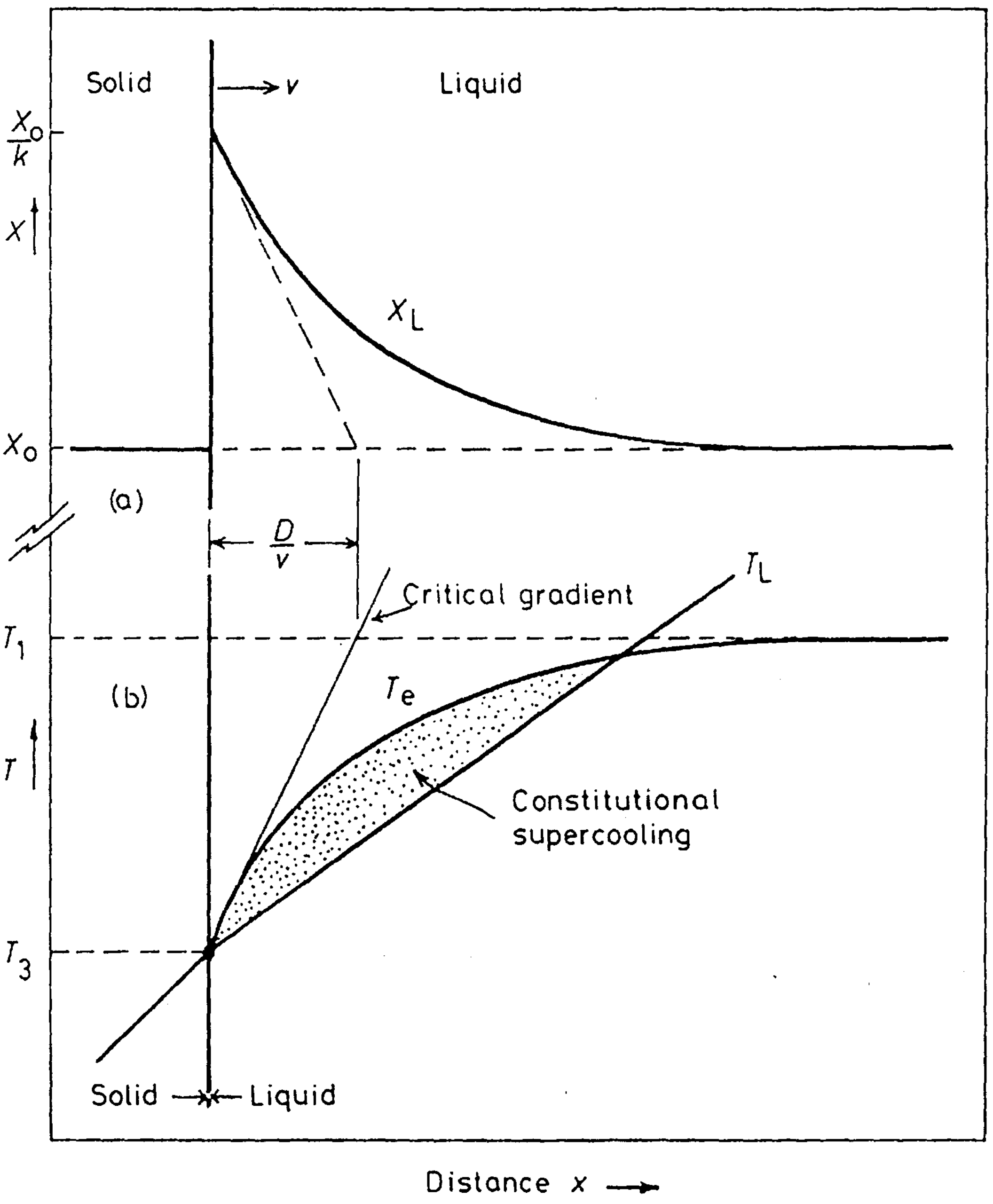

Figure 2.10 – Schematic of constitutional supercooling conditions [2.10].

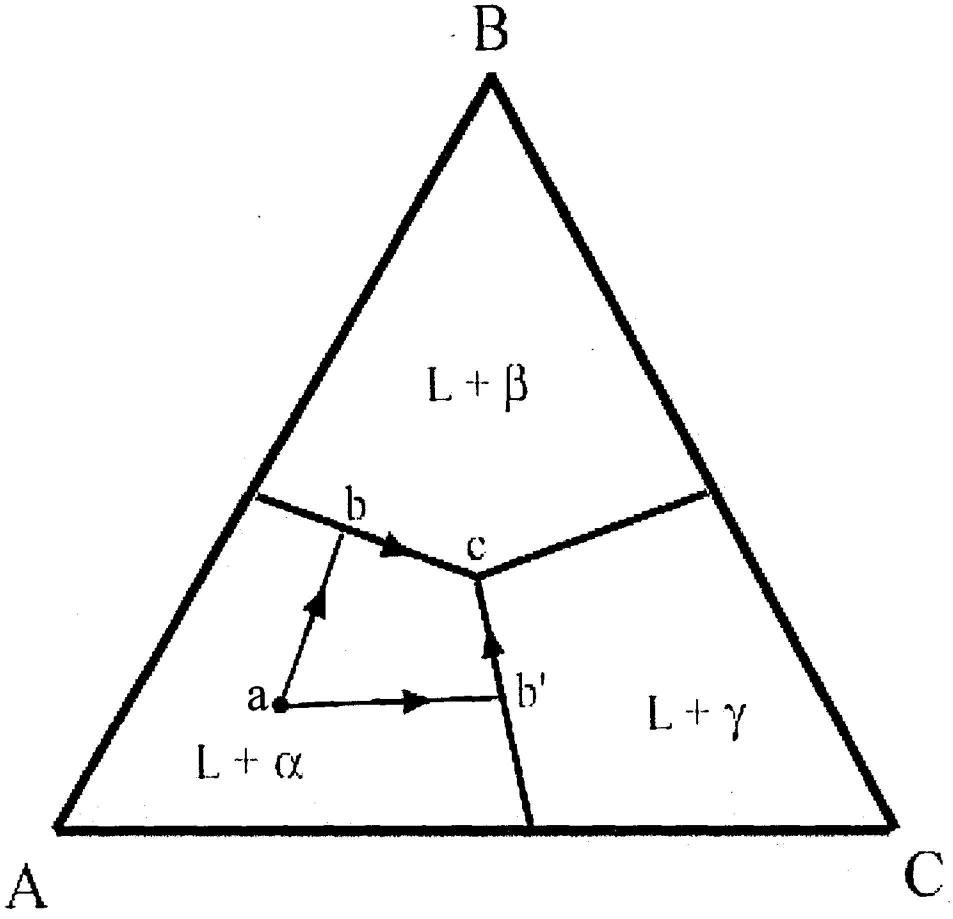

Figure 2.11 – Schematic of ternary liquidus projection with two solidification paths superimposed.

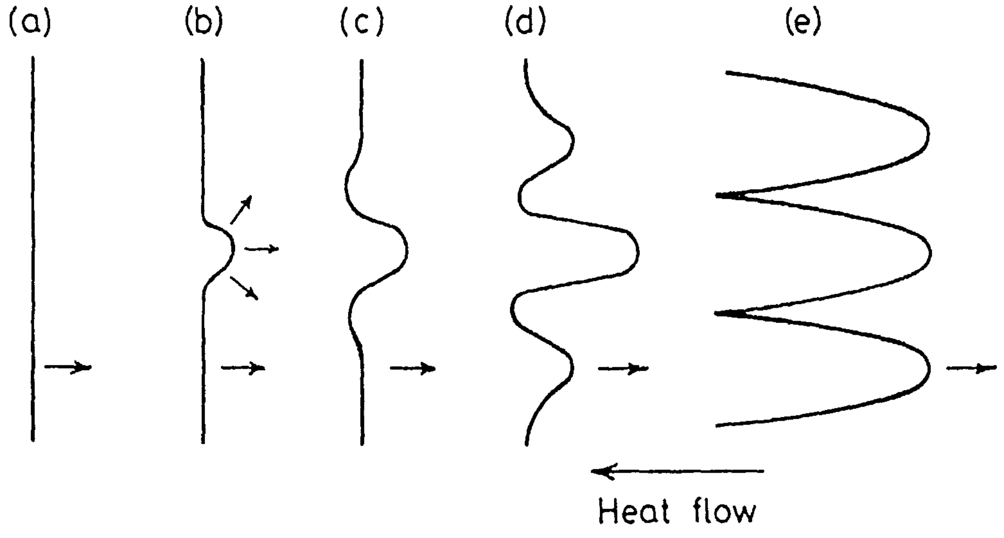

Figure 2.12 – Schematic of planar front breakdown [2.10].

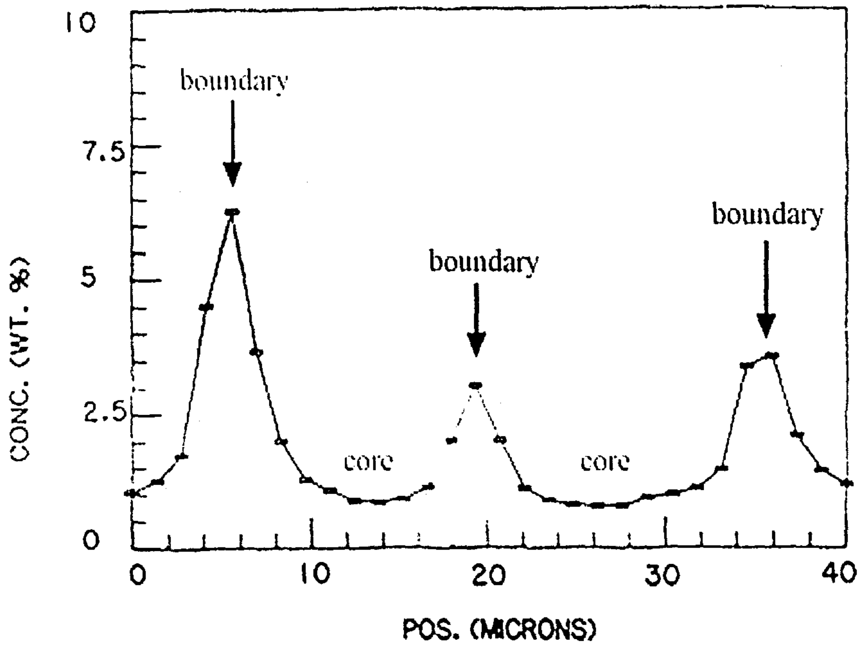

Figure 2.13 – Composition trace across cells showing compositional difference between boundaries and cores for Al-2wt% Cu [2.17].

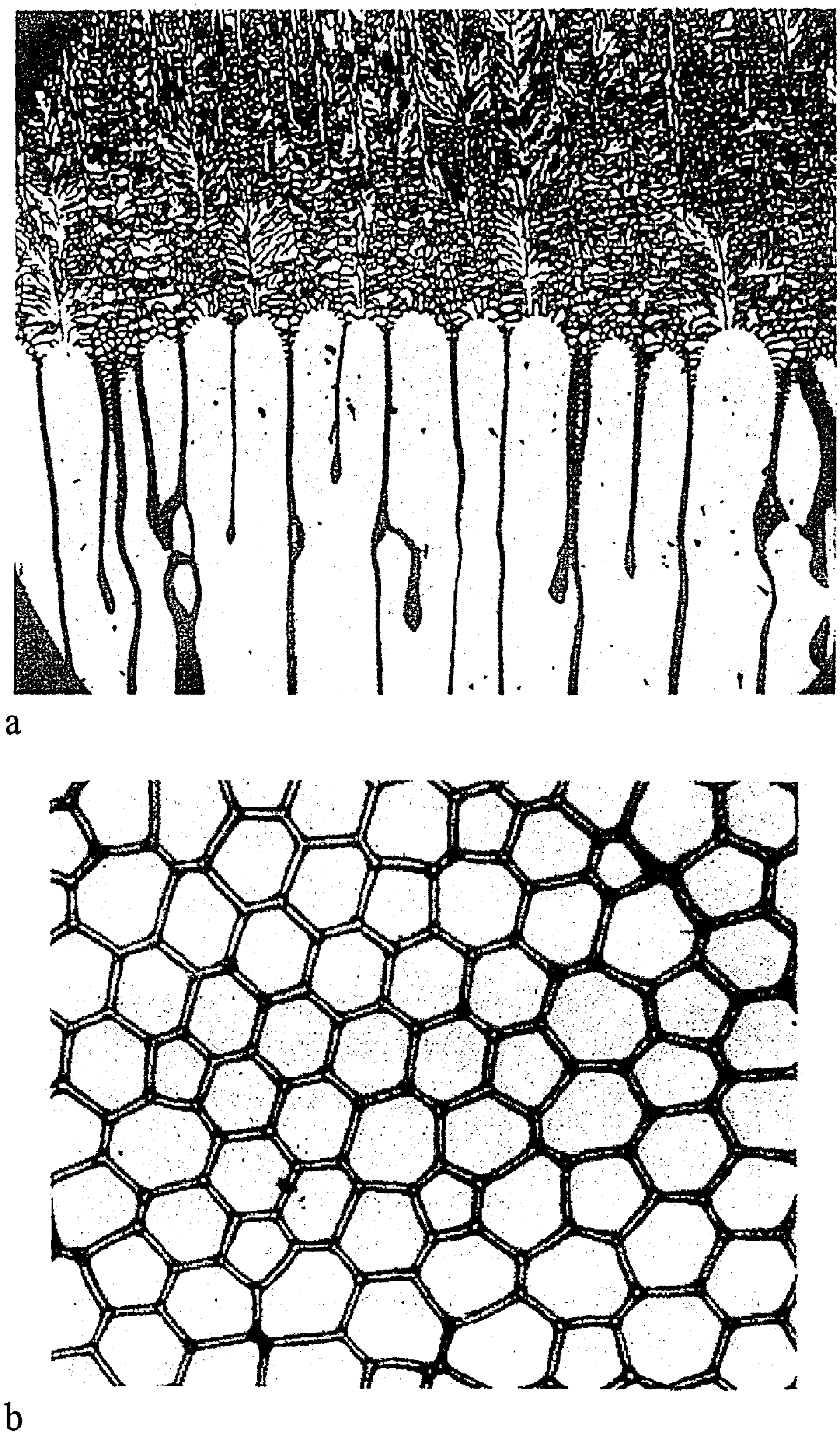

Figure 2.14 –Micrograph of cellular microstructure a) parallel to growth direction, b) transverse to growth direction [2.12].

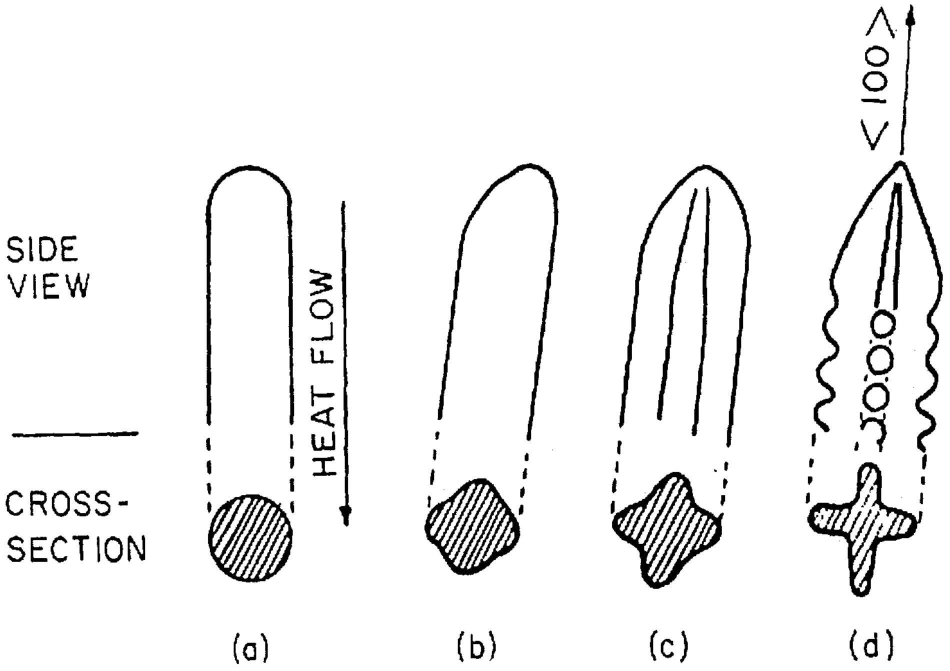

Figure 2.15 – Schematic illustrating the transition from cellular (a) to dendritic microstructure (d) with preferred growth along the <100> direction [2.12].

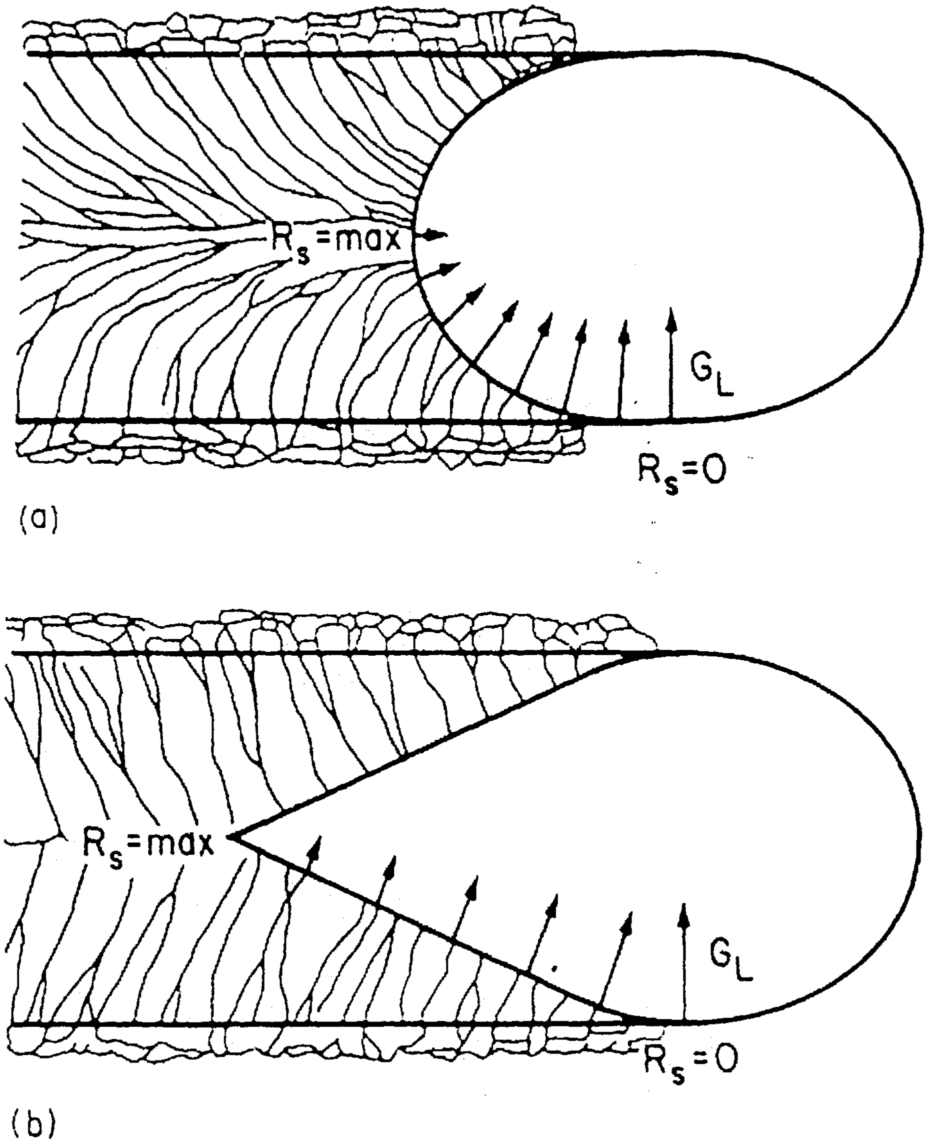

Figure 2.16 – Weld pool shape for a) low and moderate welding speeds where $\theta = 0$ at R_{max} and b) weld pool shape for high welding speeds where $\theta > 0$ at R_{max} [2.13].

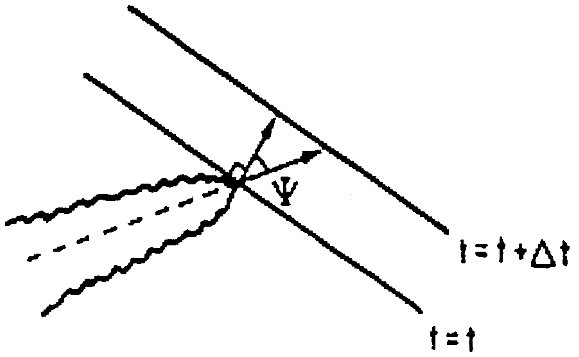

Figure 2.17 – Physical definition of ψ vector [2.13].

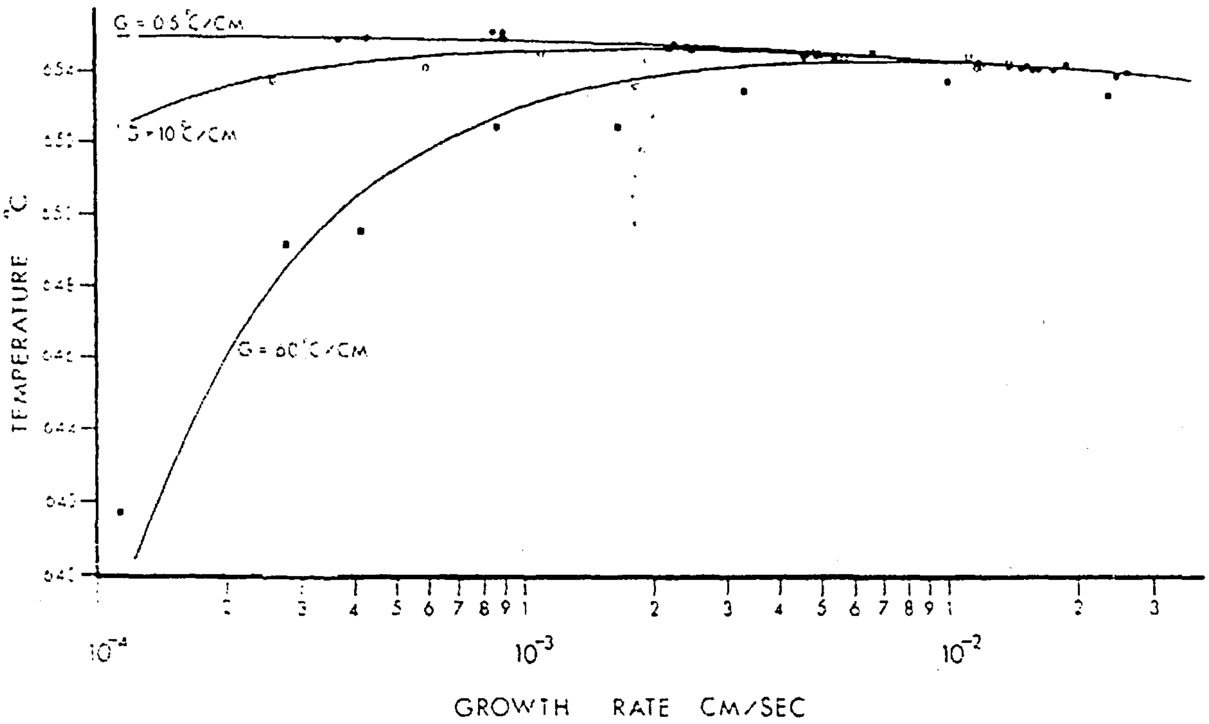

Figure 2.18 – Graph of temperature vs. growth rate for three temperature gradients, 0.5, 10, and 60 °C/cm for Al-2wt% Cu alloy [2.25].

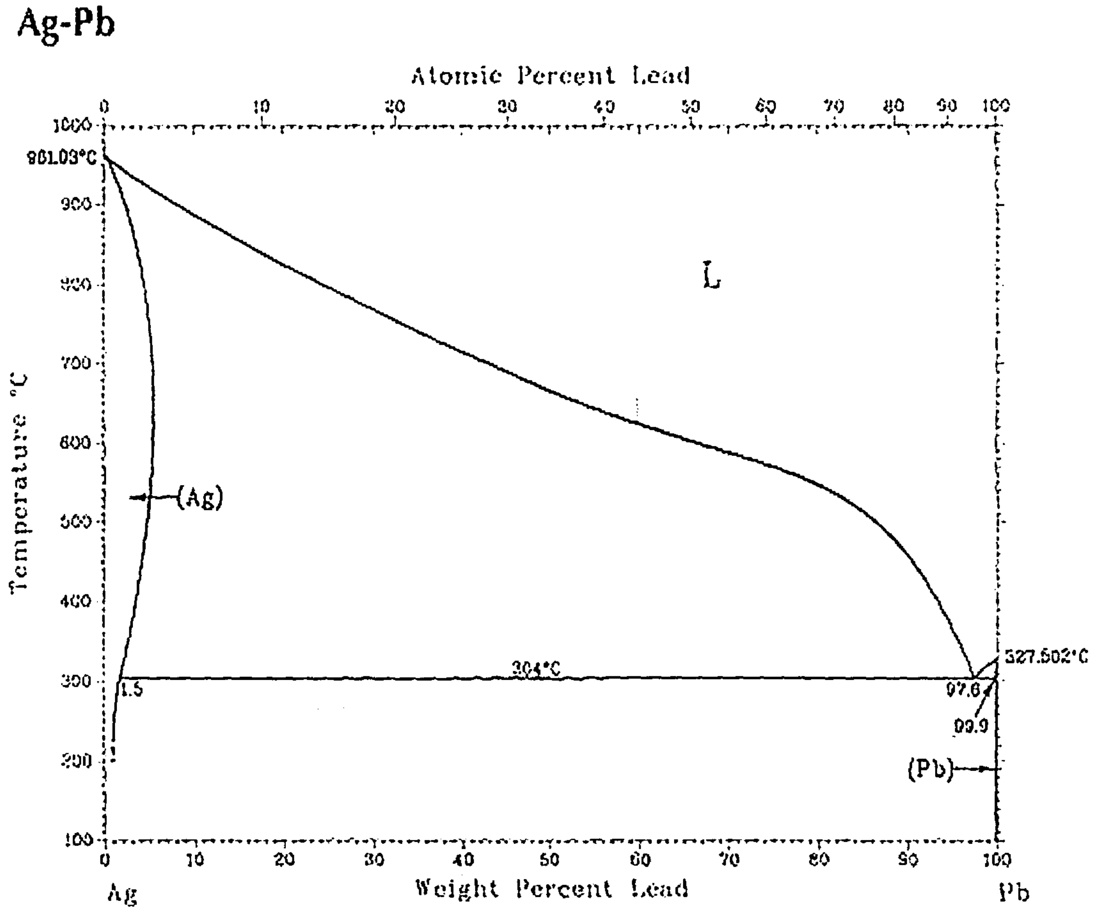

Figure 2.19a – Equilibrium phase diagram for the Ag-Pb system illustrating a large k value due to the separation of the liquidus and solidus lines [2.1].

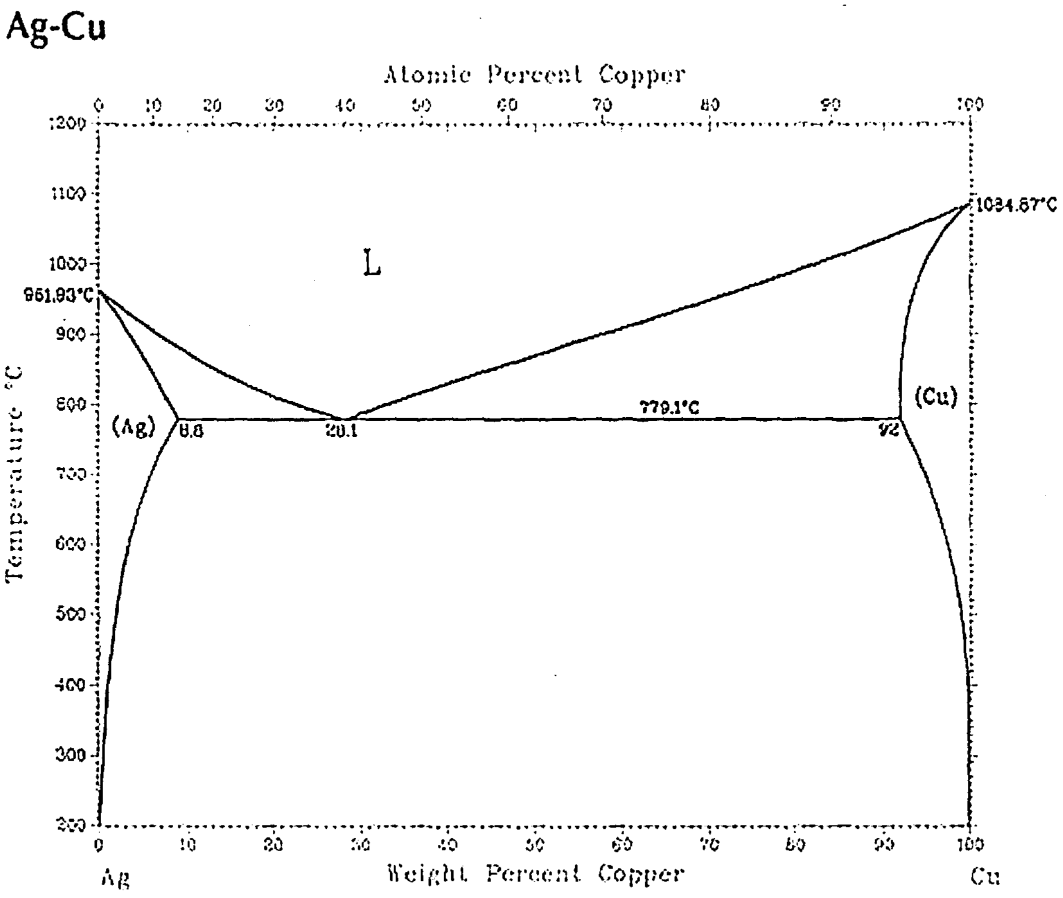

Figure 2.19b – Equilibrium phase diagram for the Ag-Cu system illustrating a low k value due to the proximity of the liquidus and solidus lines [2.1].

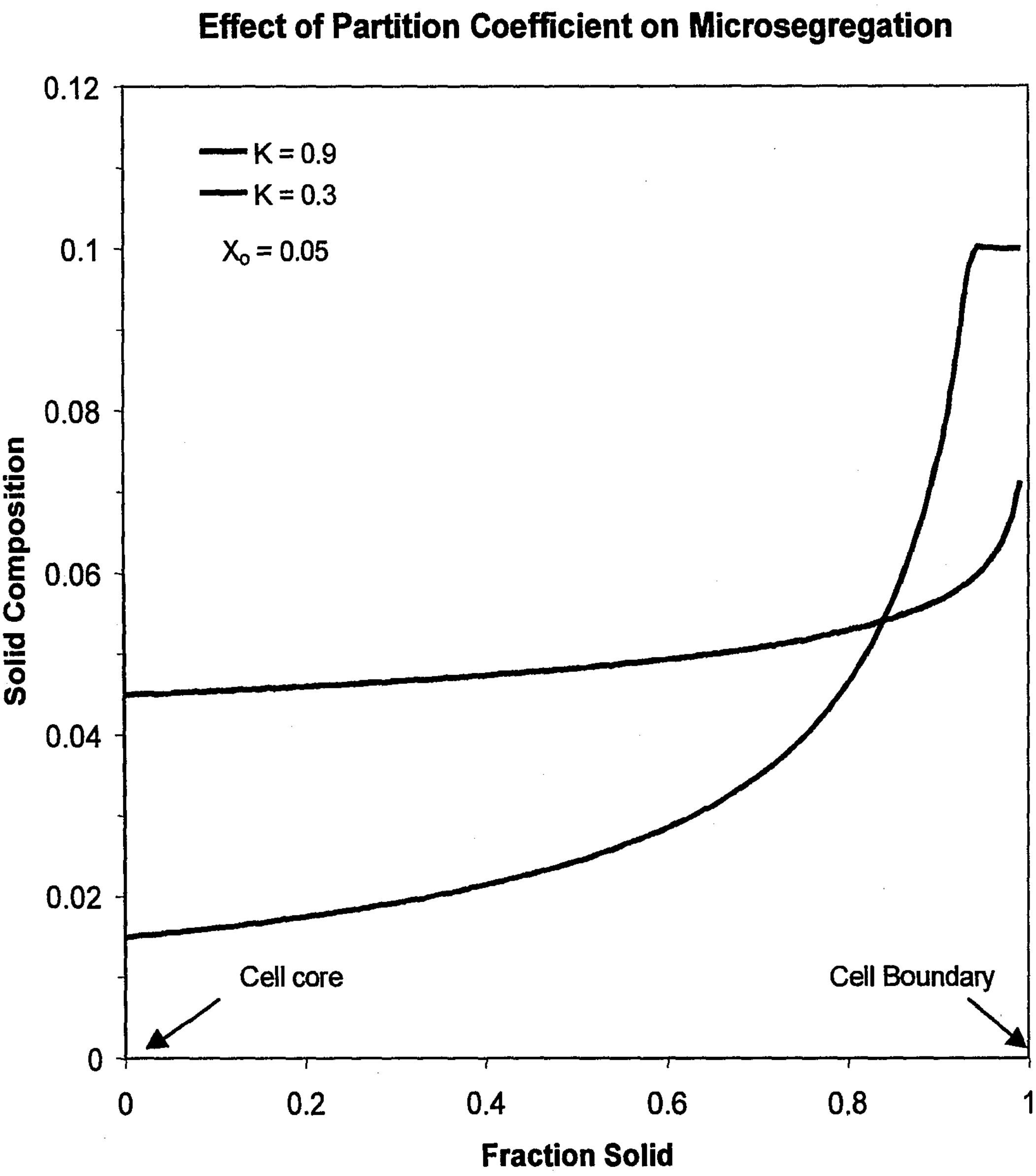

Figure 2.20 – Solidification profiles for a low k value and high k value material to illustrate the effect of k on microsegregation.

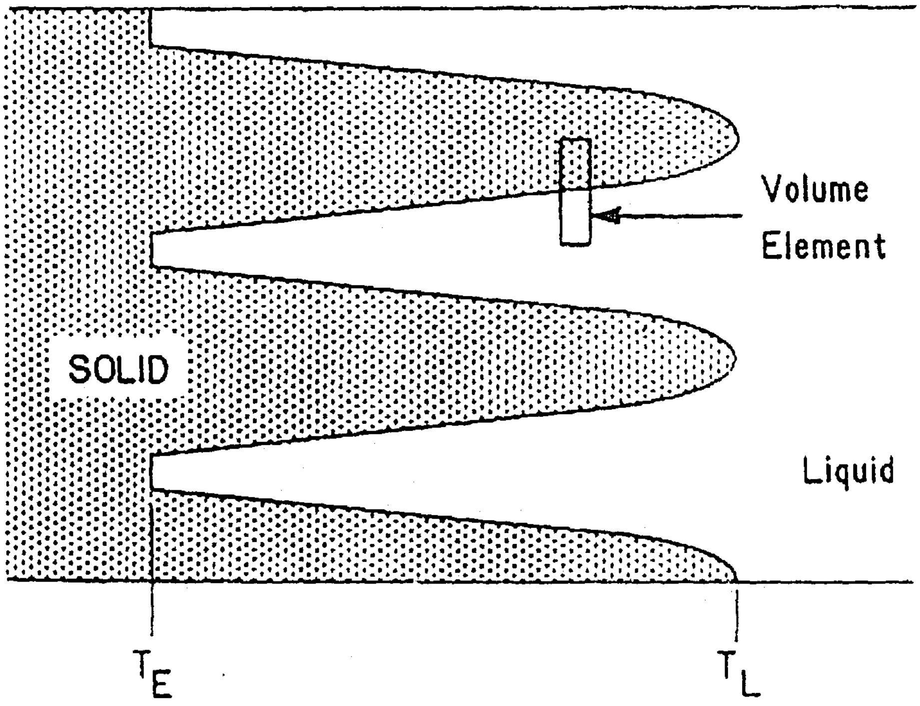

Figure 2.21 – Physical definition of the volume element used in the Scheil model [2.17].

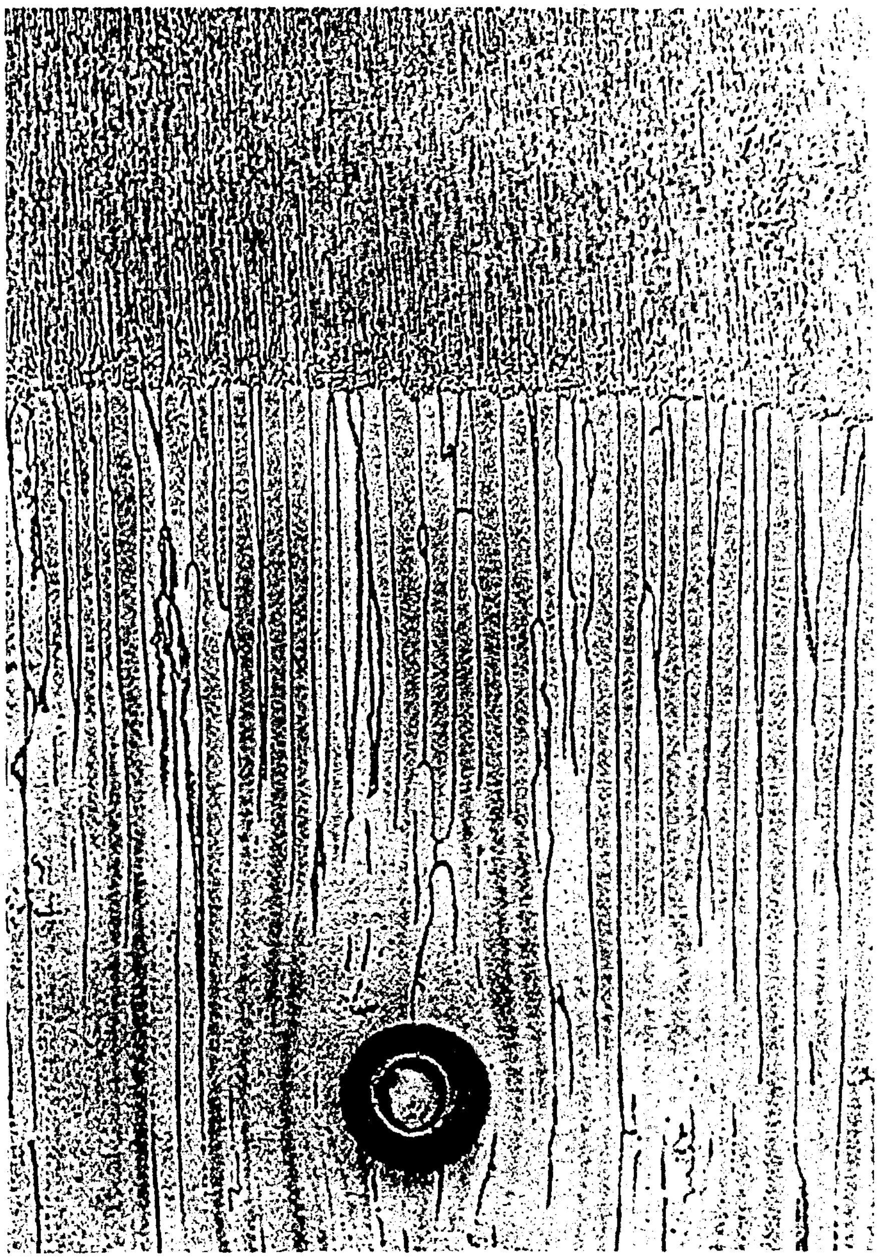

Figure 2.22 – Microstructure for Al-0.5 wt% Cu alloy used in Burden and Hunt experiment, growth rate is 3.3 x 10^{-3} cm/sec and temperature gradient is 60 °C/cm. The "knot" is the location of thermocouple used to measure the interface temperature as it grew past the thermocouple [2.25].

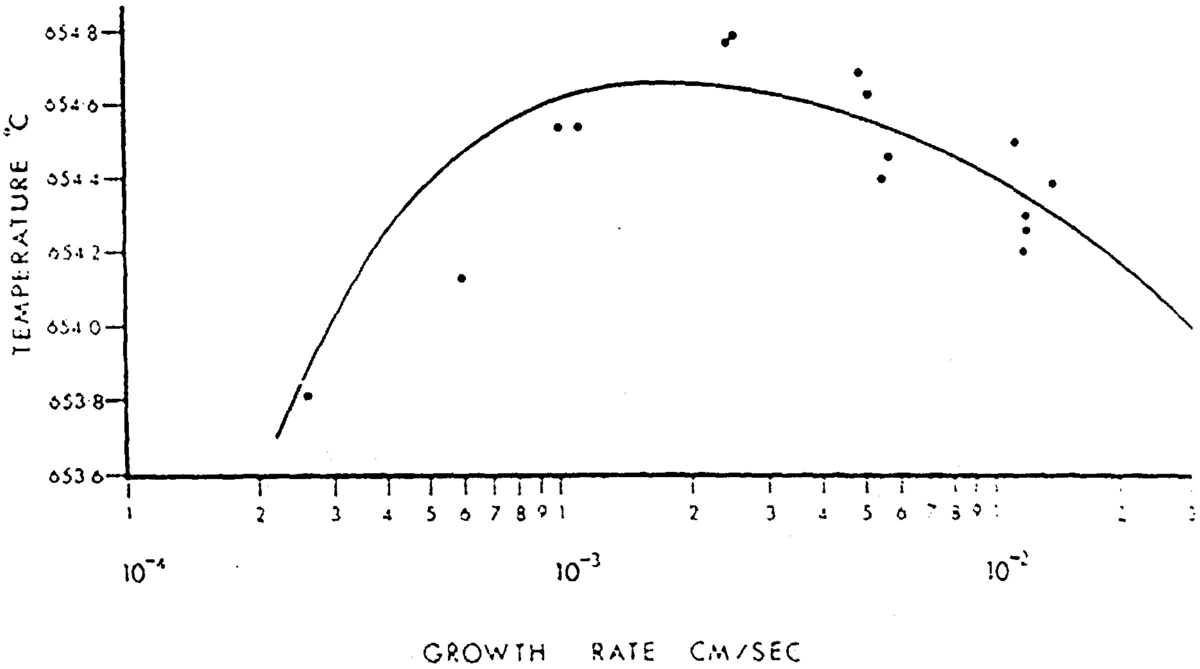

Figure 2.23 – Graph of temperature versus growth rate for Al-2wt%Cu with temperature gradient of 10 °C/cm [2.25].

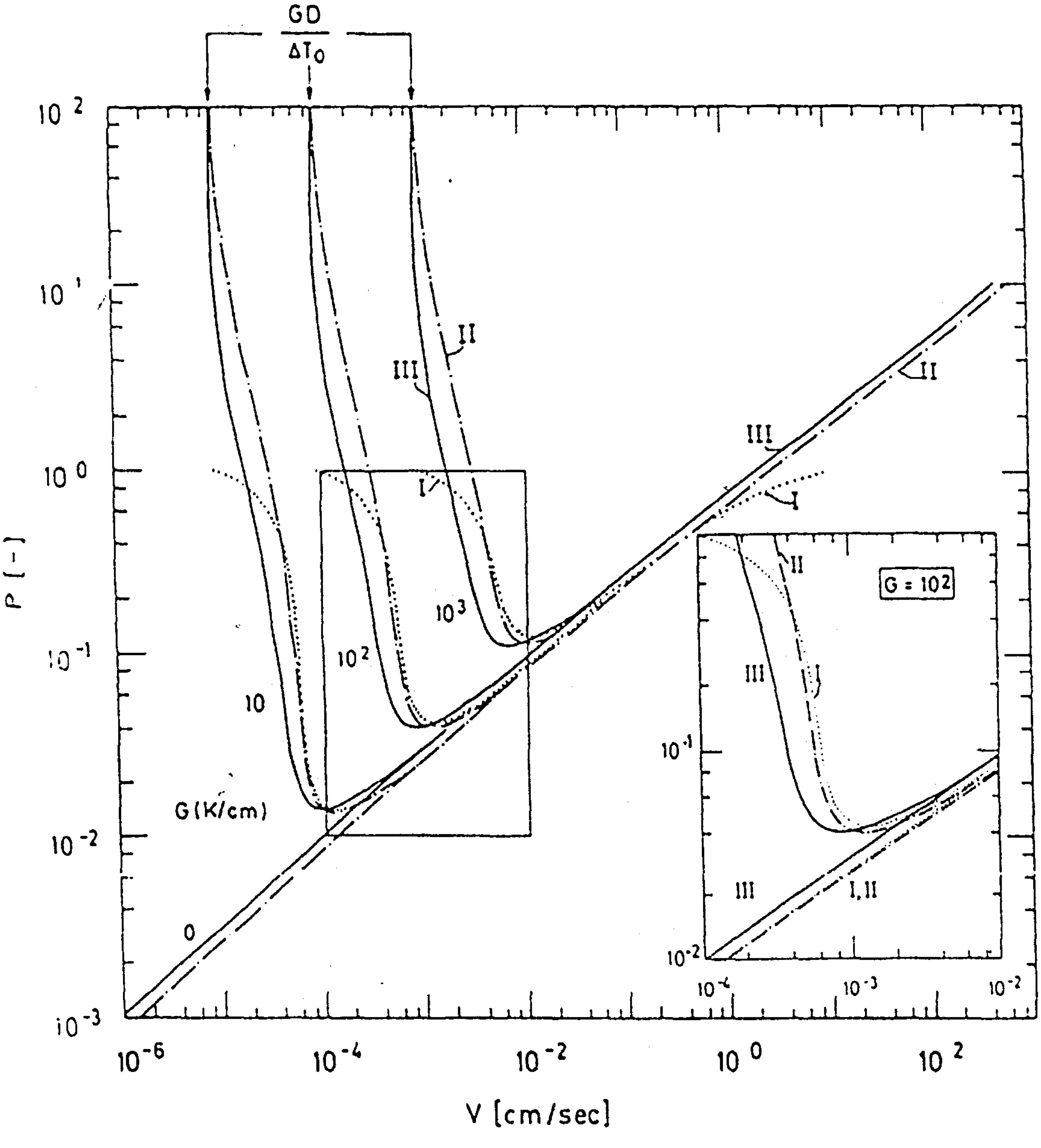

Figure 2.24 – Graph of peclet number versus growth rate illustrating behavior of models I, II, and III as defined by Esaka and Kurz [2.29].

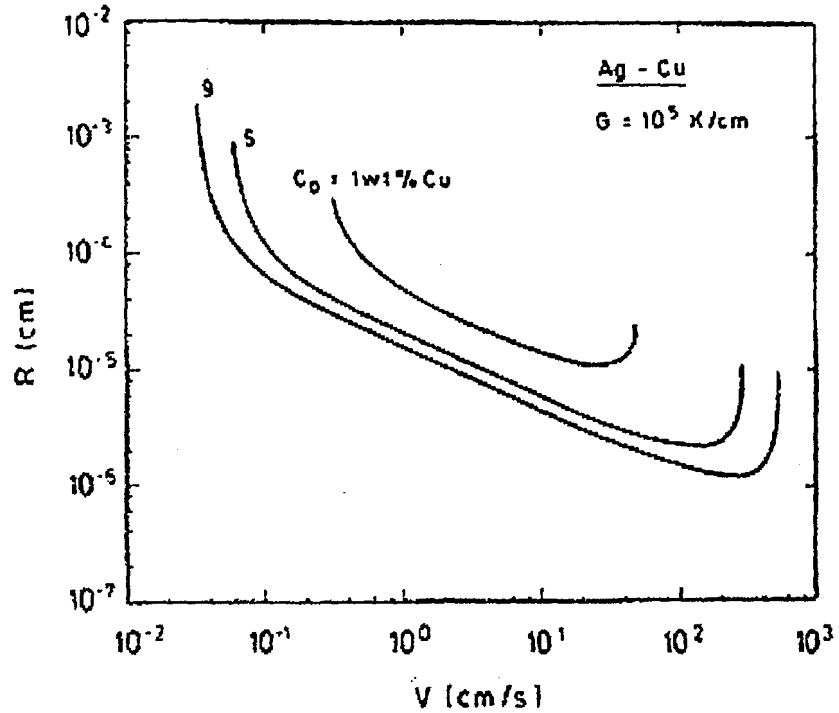

Figure 2.25 – Graph of dendrite tip radius versus growth rate illustrating breakdown of dendrite growth front to planar growth front [2.31].

3.0 Experimental Procedures

3.1 Materials System

Hastelloy B2 was chosen as a model system for nickel-based alloys. The composition of the material used in this study is seen in Table I as determined by chemical analysis. The results found in this study shall be applicable to most nickel-based alloys that the same or similar alloying elements as found in B2 (as discussed in Section 2.1.1). Ni200 was chosen for the dissimilar metal welds with B2 because it is commercially pure nickel. Thus, when melted with B2 it will act as a filler metal giving various dilutions (dependent on the beam position as discussed below) of Mo (the main alloying element in B2) in the weld. This technique allows the production of various dilutions without having to use a wire feed system with the laser welds.

Table I - Chemical Composition of Hastelloy B2

Element	Actual wt. %
C	0.01
Mn	0.7
Fe	1.7
P	0.01
S	<0.01
Si	0.02
Ni	REMAINDER
Co	0.1
Cr	0.7
Mo	27.3

3.2 Thermodynamic Database Validation and Application

The ThermoCalc program was used to calculate phase diagrams and pertinent data required to model the solidification of Hastelloy B2 [3.1]. However, before the thermodynamics calculation package was applied, it was validated for accuracy. A literature search was performed for experimentally determined thermodynamic data (liquidus and solidus temperatures, liquidus and solidus slopes, etc.) for alloy systems that the Ni-based superalloy database could model. ThermoCalc was then used to model these systems to predict the temperatures known experimentally, and the predicted data was compared to the experimentally measured data.

Once validated, the ThermoCalc program shall be used to predict phase diagrams, solidus and liquidus temperatures, solidus and liquidus slopes, solidification temperature ranges, and pertinent data for Hastelloy B2. This data was then used as inputs in the KGT model as described below.

3.3 Microstructural and Microsegregation Modeling

The KGT model was used to predict the cell spacing and dendrite tip undercooling of the autogenous laser B2 welds. The amount of dendrite tip undercooling shall then be coupled with the phase diagram to determine the dendrite tip composition (composition of the first solid to form). The materials inputs required for the KGT model were calculated from the ThermoCalc package as discussed above. The predicted cell spacing and tip composition values were compared to values measured experimentally.

3.4 Weld Sample Preparation

3.4.1 Dissimilar Laser Welds

Weld coupons of Hastelloy B2 and Ni200 alloys were produced to act as base metal for the dissimilar metal welds. The coupons were rough cut on a table saw and milled to final dimensions of 4.5 x 0.5 x 0.125 inches. Laser beam welds were then performed on the weld coupons oriented in the geometry shown in Figure 3.1. The beam placement was varied to be –0.9 mm, -0.3 mm, -0.15 mm, 0 mm, 0.15 mm, 0.3 mm from the B2/Ni200 interface (negative being in the B2 base metal). By varying the beam placement, varying amounts of Ni200 and B2 would be melted, thus giving a range of dilution of Mo. The dissimilar metal welds were performed at the processing conditions listed below in Table II, giving a total of 108 welds.

Table II – Dissimilar Metal Laser Weld Processing Variables

Travel Speed, mm/s	Power, W	Beam Position, mm*
8.5	600	-0.9
16.9	1200	-0.3
25.4		-0.15
33.9		0
42.3		0.15
50.8		0.3
59.3		
67.7		
76.2		

*Negative values denote B2 base metal side

3.4.2 Hastelloy B2 Laser Welds

Laser beam welds were also performed on Hastelloy B2 base metal to study the rapid solidification microstructure and microsegregation profiles in the as welded microstructure. Weld coupons 12 x 1 x 0.25 inches were produced by plasma cutting from Hastelloy B2 sheet stock. Autogenous welds were then performed on the face of the plate as shown in Figure 3.2. Welds were performed under the following conditions as listed in Table III below, giving a total of 9 welds.

Table III – B2 Autogenous Weld Processing Variables

Travel Speed, mm/s	Power, W
8.5	1200
16.9	
25.4	
33.9	
42.3	
50.8	
59.3	
67.7	
76.2	

3.4.3 Autogenous GTA B2 Welds

GTA welds were also performed on Hastelloy B2 base metal to study the rapid solidification microstructure in the as welded microstructure. These high speed welds allowed for direct comparison between high energy density welding processes (laser welding) to traditional arc processes (GTA welding). Weld coupons 12 x 1 x 0.25 inches were produced by plasma cutting from Hastelloy B2 sheet stock. Autogenous welds were then performed on the face of the plate in the same orientation as the laser welds, shown in Figure 3.2. Welds were at 1370 W from 5 to 75 mm/s in increments of 5 mm/s, giving a total of 15 welds. The welding power was larger than the laser welding, but was as close as possible given welding equipment limitations.

3.5 Characterization

Macroscopic photographs of the as welded samples were taken using an Olympus SZH10 Stereoscope and Leco 2001 Image Analysis System. Once documented, the welds were sectioned and mounted in cold setting epoxy to view the cross section metallographically. The cross section samples were ground in these steps: 240 grit, 320 grit, 400 grit, and 600 grit. After 600 grit grinding the samples were polished with 6 μm diamond compound, 0.3 μm alumina slurry, and a final polish of 0.03 μm colloidal silica. The samples were then etched in a chromic acid solution for 3-10 seconds (depending on etchant age) to reveal the cellular microstructure of the fusion zone. Care was taken after the final polish not to let the sample dry before etching, as a surface oxide can form and inhibit the etching step [3.2].

Photomicrographs of the cross sections of the welds were taken using a Reichert-Jung MeF3 Metallograph. The weld penetration, width, and cell spacing was measured using a Nikon Microphot light optical microscope coupled to the Leco 2001 Image Analysis program.

For the autogenous B2 laser and GTA welds, samples were mounted in plate surface and weld centerline geometries in addition to the cross sections discussed above as shown in Figure 3.3. These samples were sectioned utilizing the Struers Accutom 50 high-speed cutting wheel since it allows precise sectioning. The samples were mounted in thermosetting epoxy (rather than cold setting epoxy) for the mounts increased hardness which gives better edge retention. The grinding, polishing, and etching stages were the same.

The solidification velocity was determined for the autogenous B2 laser and GTA welds via microstructural analysis. The cellular growth angles relative to the welding direction were measured and related to the travel speed to determine solidification velocity.

3.6 Melting Efficiency Measurement

It is often important to know the melting efficiency of the welding process to ensure optimum operating conditions. Fuerschbach has derived a method to determine the melting efficiency via dimensionless analysis [3.3]. Fuerschbach defines two dimensionless parameters, ***Ch*** and ***Ry***, as:

$$Ch = \frac{v^2 A}{\alpha^2} \qquad (3.4)$$

$$Ry = \frac{q_i v}{\alpha^2 \delta h} \qquad (3.5)$$

where v is the travel speed, A is the weld cross-sectional area, α is the thermal diffusivity at the liquidus temperature, δh is the melting enthalpy, and q_i is the heat input into the base metal. The melting efficiency can then be defined as:

$$\eta_m = \frac{vA\delta h}{q_i} = \frac{Ch}{Ry} \qquad (3.6)$$

From equation (3.6) it is seen that to calculate the melting efficiency directly knowledge of v, A, δh, and q_i is needed. The v term is a user defined parameter, A can be measured metallographically, and δh is a measurable materials property. However, without tedious experimental techniques it is difficult to determine q_i. It is also noted that if Ch and Ry are known, the melting efficiency is just their ratios. Ch can be found from equation (3.4), all required values are measured or controlled. However, one must know q_i to calculate Ry as seen in equation (3.5). Fuerschbach also established the empirical relation:

$$Ch = Ry\left[0.48 - 0.29\exp\left(\frac{-Ry}{6.8}\right) - 0.17\exp\left(\frac{-Ry}{59}\right)\right] \qquad (3.7)$$

So that if Ch is known Ry can be back calculated.[3] Using this technique values for Ch and Ry were found for all welds studied and the melting efficiency was calculated from equation (3.6).

3.7 Microsegregation Measurement

The degree of microsegregation across the cells was measured using Analytical Electron Microscopy (AEM) in a JEOL 2000FX TEM on the autogenous laser B2 welds. AEM is required for the laser welds due to the small cell size produced by the high temperature gradient and growth rate. The measured cell core composition shall be compared to the composition predicted from the KGT model (taking undercooling into consideration).

3.7.1 TEM Sample Preparation

The bulk weldment was cut into a thin strip with the weld oriented at the center of the strip. The strip was then ground to 500 μm thick using 300 grit and 600 grit SiC paper. The strip was further thinned to 150 μm using 800, 1000, and 1200 grit SiC papers. 3 mm diameter discs were then punched from the strip, with the welding direction indicated on the discs. It is important to know the welding direction on the TEM sample so that the growth velocity is known for the examined regions of the sample. After the samples were punched, the center of the disc was thinned to 10 μm using a VGR dimpler. Final thinning was performed on a Gatan Precision Ion Polishing System (PIPS) until a small hole appeared at the center. The sample was then ready for TEM examination.

3.7.2 AEM Analysis

A JEOL 2000FX TEM was used to examine the cellular structure of the Hastelloy B2 laser welds. The microscopy was performed at an accelerating voltage of 200KV in bright field mode. X-Ray Energy Dispersive Spectroscopy (EDS) was used to measure the composition of Mo and Ni in line scans across the cellular microstructure. The EDS system used was an Oxford QX2000i. A standard sample of the unwelded base metal was prepared in the same method as the samples to be analyzed. A chemical analysis was performed on the material to accurately determine the composition. This standard sample was then analyzed under the same conditions as the weld samples. A factor, K_{AB}, was then determined to relate the EDS peak intensities to the sample composition:

$$\frac{X_A}{X_B} = K_{AB} \frac{I_A}{I_B} \qquad (3.8)$$

where $X_{A,B}$ is the composition of A or B and $I_{A,B}$ is the intensity of the A or B element peak. Thus, when the intensities of the weld samples were analyzed the compositions of Mo or Ni could be determined with the aid of the following relation:

$$X_A + X_B + X_{bal} = 1 \qquad (3.9)$$

where X_{bal} is the sum of the compositions of the rest of the elements in Hastelloy B2. The lowest composition of the trace across a cell corresponds to the cell core, the first solid to form. This value was compared to the cell core composition predicted by the KGT model.

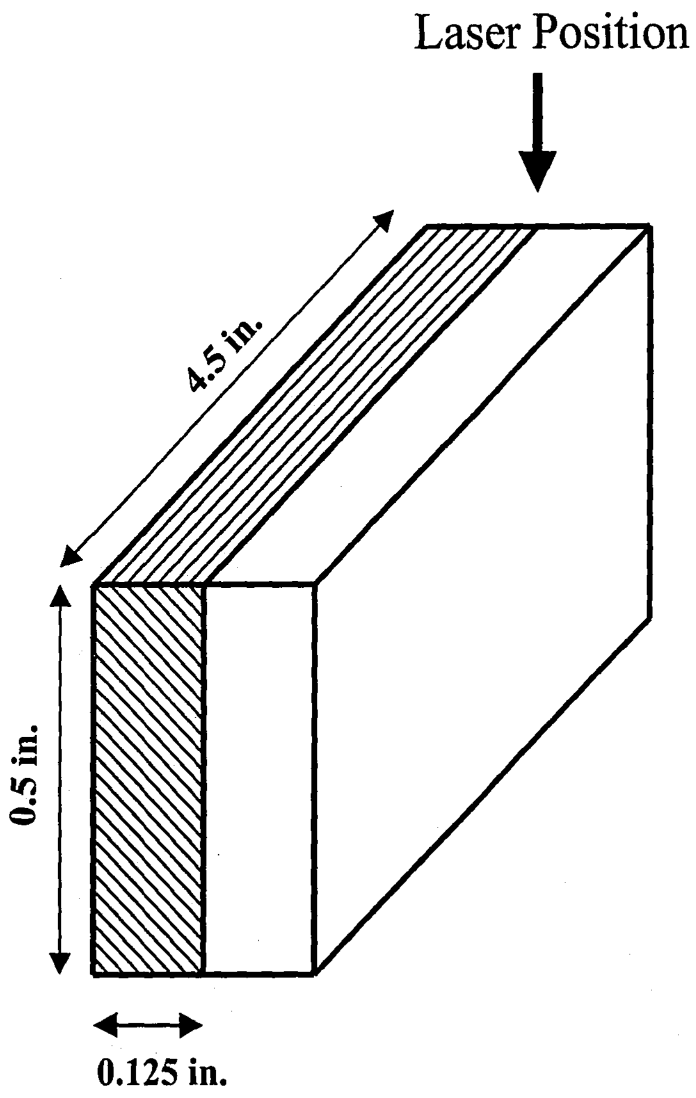

Figure 3.1 – Dissimilar metal laser weld sample geometry. The shaded bar represents Ni200 while the white bar represents B2 alloy.

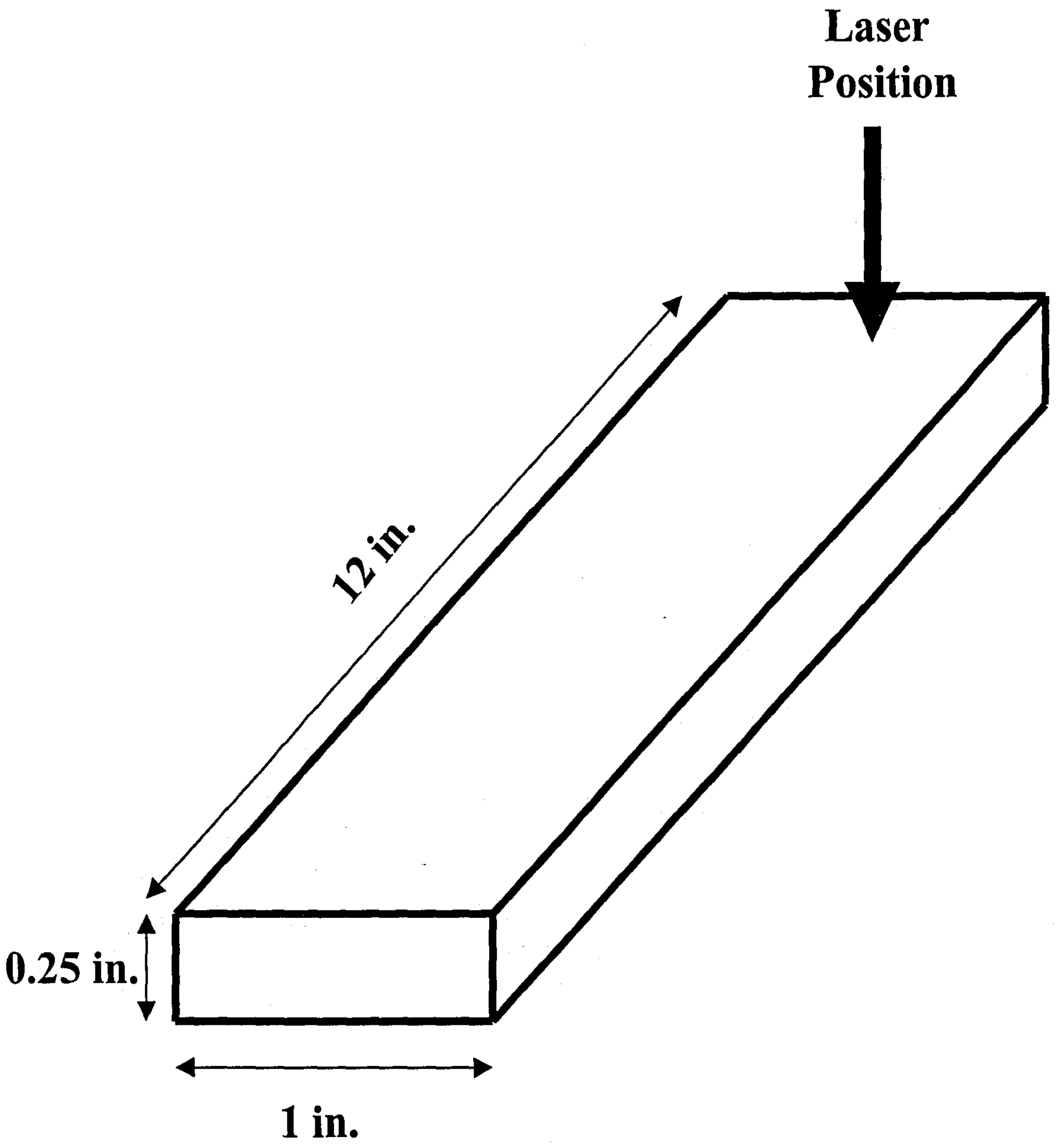

Figure 3.2 – Autogenous laser weld sample geometry

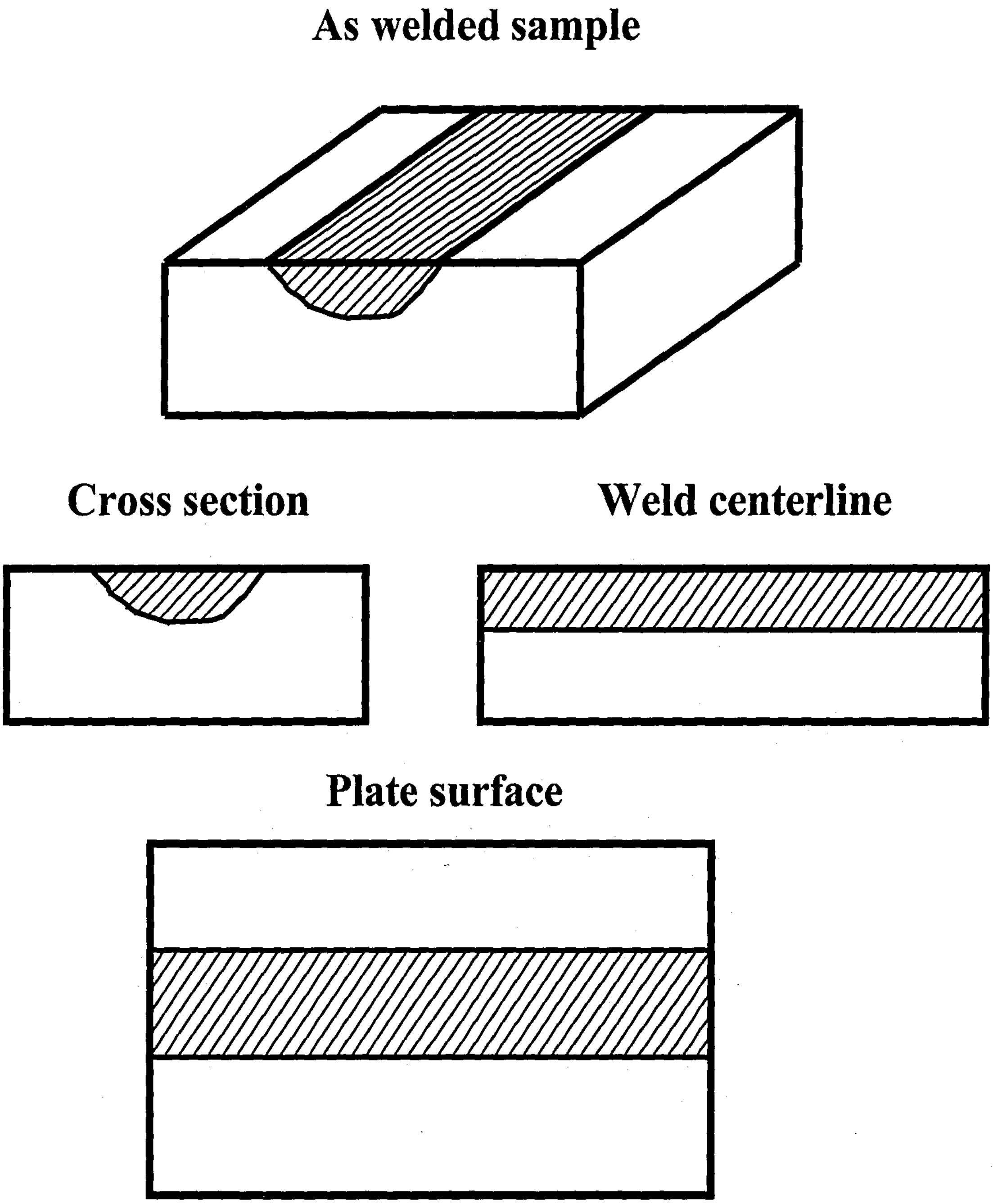

Figure 3.3 – Schematic illustrating as received welded autogenous B2 sample and mounting perspectives. Shaded regions represent weld fusion zone.

4.0 Experimental Verification of ThermoCalc

The ThermoCalc thermodynamics calculation software package has been used to study the solidification behavior of several nickel-based superalloys. If proven accurate through comparison to experimentally determined data, the program will aid in the study of experimental nickel alloy systems. Using the ThermoCalc program to predict thermodynamic data for unknown alloy systems is advantageous over repetitive and time consuming physical experiments. ThermoCalc can calculate many thermodynamic values not easily measured experimentally, so verification of its accuracy is crucial to determine if it is a useful tool for modeling nickel super alloy solidification.

4.1 Liquidus and Solidus Temperatures

The liquidus and solidus temperatures for a number of commercial and experimental nickel based superalloys are listed in Table I. Experimental values for these temperatures have been researched in the literature and are compared to the ThermoCalc calculated values in Table I. The liquidus and solidus data listed in Table I have been graphed to show the deviation from calculated to measured data, as seen in Figures 4.1 and 4.2. The straight line on both graphs represents a 1:1 ratio; if the points corresponded perfectly they would all lay on the line. The average deviation for the liquidus is 7.9 °C while the average deviation for the solidus is 22.6 °C.

The Hastelloy C series of alloys (C-4, C-22, and C-276) provide the largest deviation from the line in Figure 4.1 [4.1]. This could be caused by the exclusion of Mn, P, S, Si, V, and W from the ThermoCalc database, as seen in Table II. Table II lists the elements included in the ThermoCalc database along the top of the table and compares this to the elements included in the alloys studied. The alloys excluded from the database are in bold along the right hand side of the table. While P and S are only tramp elements always kept to a minimum, the others are present in significant amounts and their exclusion from the calculation would most likely affect the end result.

The experimental data presented above can be corrected to eliminate the effect of silicon, thus allowing it to be directly compared to the ThermoCalc values. To do this, the equation for the liquidus line of Silicon must be known for the alloys. Table III indicates measured experimental Si liquidus slopes for some of the alloy systems studied [4.2, 4.3]. By knowing the slope of the liquidus and the amount of silicon in the alloy, it is possible to calculate the temperature depression caused by the addition of the silicon. This is illustrated in the example partial phase diagram shown in Figure 4.3 (only the liquidus line is represented). If the alloy solidifies at T_0 without any silicon, the silicon liquidus shows that with higher silicon concentrations the alloy will solidify at a lower temperature. If the slope of the liquidus and the amount of silicon in the alloy are known, it is possible to predict the amount of this depression by the equation:

$$\text{temperature depression} = m_L(C_{Si}) \qquad (4.1)$$

where m_L is the silicon liquidus slope, and C_{Si} is the alloy's silicon composition. The temperature depression values are listed in Table III. If one refers to Figure 4.1, it is seen that the ThermoCalc liquidus values for the Inconel 625 alloys are already lower than the experimentally measured values. Therefore, with the Si effect taken into account the actual deviation from experimental to calculated values increases. When one examines the experimental niobium bearing alloys, it is seen that the majority (11 versus 8) of liquidus temperatures are over predicted by ThermoCalc [4.2]. Therefore, for these alloys its seems that correcting for silicon increases the accuracy of the results. This suggests that for the Inconel 625 alloys it is not the exclusion of Si that is causing the deviation in liquidus temperatures. From Table II it is seen that Mn is excluded from the Inconel 625 alloys but is not present in the experimental niobium alloys. Correcting for Mn is not possible for this data since the experimental Mn liquidus slope is not known [4.3]. Examination of Figure 4.1 and Table II shows that the alloys that provide the largest deviation all have Mn present. This deviation might be blamed by the exclusion of Mn from the alloy, but Hastelloy W is one of the most accurate points in Figure 4.1 and it contains Mn as well. Also, the effect of Mn would be to depress the liquidus temperature further, decreasing the accuracy of ThermoCalc. At this point it is not known what causes these deviations.

When studying the solidus temperatures plot in Figure 4.2, the Thermo-Span data provides the largest deviation. This could be due to the very low nickel content of the alloy (24.42 wt %). The ThermoCalc database warns against using Ni compositions lower than 55 wt %, however the results for Incoloy 909 are decent even though its nickel content is only 37.30 wt %. When its composition is examined, it is seen that again Si, P, and S are excluded from the calculation; however the alloy is low in all elements and the effect is most likely not that large.

A general trend is seen that ThermoCalc calculates the liquidus temperatures with more accuracy than the solidus temperatures, as witnessed by the average deviations mentioned above. It is also seen that ThermoCalc predicts solidus temperatures that are generally lower than the experimentally measured values. However, it should be noted that the agreement is generally good and provides a useful technique to predict thermal properties that would take much longer to experimentally determine.

4.2 Liquidus and Solidus Slopes and Partition Coefficients

ThermoCalc was used to calculate the liquidus and solidus slopes for the alloy systems listed in Table IV and Figure 4.4. To calculate the liquidus and solidus slopes the alloy composition was systematically varied. The liquidus and solidus temperature were calculated for the original alloy composition. Since these temperatures correspond to only one point on the liquidus or solidus surface, more information is needed to measure the slope of the surface. The element that the liquidus or solidus is being calculated for is systematically varied (holding the rest of the alloy composition constant). By varying the composition of the element being studied, a range of liquidus and solidus temperatures can be obtained, thus giving the slope of the liquidius or solidus for that element in the alloy. Since the remaining elements are held at constant composition, only the effect of the element of interest is measured. Figure 4.4 shows the measured and calculated liquidus and solidus lines for the experimental Nb bearing alloys. This figure shows that the slopes do not change appreciable for varying amounts of C or Nb, which has been confirmed experimentally [4.4]. The calculated values for these slopes are listed in Table V, and compare well with the experimentally measured values listed as well. It is interesting to note that the Nb slopes agree fairly well, while the C slopes are approximately one half the measured values. For the 625 alloy series, an average of the 8 alloys was reported for the Nb and C slopes. In this study, only the low

Si alloys (1,2 5, and 6) were studied since Si is not included in the ThermoCalc database. The average over the four compositions that were calculated are as follows:

Solidus and Liquidus Slopes for Low Si 625 Alloy Systems

Measurement Type	Element	Solidus Slope	Liquidus Slope
Experimental	Nb	-20.6	-11.1
Calculated	Nb	-30.6	-11.4
Experimental	C	-507.4	-108.6
Calculated	C	-467.5	-45.4

It is possible to compare the experimental data to the calculated data (even though Si is not accounted for in the calculated data) since there are no interactive effects of Si. This was proven by regression analysis by Cieslak et al. They measured corellation coefficients to be 0.97 and above, indicating Si has a minimal affect on the data for Nb and C. It is seen the data agrees within reason. The four alloys studied show the effect of varying the carbon and niobium content holding all other elements constant.

The partition coefficients were determined by the ratio of the liquidus slope to the solidus slope. This assumes linear liquidus and solidus lines, which was found to be accurate for the alloys studied, as seen in Figure 4.4. The values calculated for the experimental Nb bearing alloys are compared to measured values in Table V. The calculated Nb and C partition coefficients agree well with the measured data. The binary partition coefficients are shown for comparison, it is seen that the coefficients are lower in the multicomponent system, an indication of decreased solubility. This indicates a possible source of error when applying binary data to real world multi-component alloy systems. The partition coefficients for the Thermo-Span, Incoloy 909 and Inconel 718 alloys reported in Table IV show good agreement.

4.4 Scheil Simulations

ThermoCalc was utilized to calculate Scheil simulations of Hastelloy Alloys C-22, B2, W, and C-276. The Scheil simulation takes into account non-equilibrium solidification, whereas all other calculations up to this point have been equilibrium calculations (See Section 2.4.1 for a more in-depth discussion of the Scheil model). Since most real life applications fall under non-equilibrium solidification, it is important to verify ThermoCalc's accuracy in predicting non-equilibrium calculations. As an example of a Scheil calculation, Figure 4.5 shows temperature versus weight fraction solid for both C-22 and C-276 alloys. The calculated reaction sequence agrees with measured data. The C-22 plot predicts $L \rightarrow L + \gamma \rightarrow L + \gamma + \sigma$, while the C-276 plot predicts $L \rightarrow L + \gamma \rightarrow L + \gamma + P$, both of which are the reaction sequences seen experimentally [4.1]. These plots illustrate the fraction of solid formed (and what phases are forming it) for a given temperature

By plotting the variation in the primary solidification phase of an element's composition it is easy to validate the accuracy of the results by direct comparison to the microprobe data taken experimentally. These calculations were made for Mo, Cr, and Ni in alloy C-22. Figure 4.6 compares this calculation favorably to the findings of Cieslak et al [4.1]. In Cieslak's data, a microprobe trace was performed across one dendrite. Figure 4.6b shows the data measured, where the 1 micron point represents the core of the dendrite. The higher the position, the further towards the edge of the dendrite the microprobe measured its composition. Therefore, the left hand side of the Figure 4.6b represents the beginning of solidification at the dendrite core (DC in the Cieslak data) while the right hand side represents the end of solidification just before the interdendritic eutectic is reached (labeled ID in the Cieslak data). The ThermoCalc data represented in Figure 4.6A shows good quantitative agreement with the physical data. The "weight fraction gamma" shows the fraction of solid formed, which can be directly compared to the position in Figure 4.6b. At just above 0 weight fraction gamma, solidification is just beginning, corresponding to the 1 micron position in Figure 4.6b. As the weight fraction increases, this is physically represented by the dendrite growing (or the position in Figure 4.6b increasing). At the end of the curve in Figure 4.6a (approximately 0.9 weight fraction gamma), solidification is about to end as the terminal reaction is reached. This corresponds to the 8 micron position in Figure 4.6b, the edge of the dendrite. The remaining liquid (approximately 0.05 weight fraction in Figure 4.6a) solidifies at the terminal solidification reaction.

Figures 4.7 and 4.8 illustrate the Scheil simulations for B-2 and W. For all of the calculations except Hastelloy B-2 the phases of interest were included in the ThermoCalc database. For B-2, experimental data suggests that the carbide Ni_2Mo_3C forms, which is not in the ThermoCalc database. However, this phase has not yet been proven experimentally. To calculate the Scheil simulation for B-2 two calculations were made. The first specifying that liquid, gamma, P, σ and μ were present, the other allowing ThermoCalc to choose the phases that precipitate. It is seen that the liquidus temperature of 1411 °C does not change between the two simulations. This is because the primary solidification phase gamma is the same for both simulations. It is the end of primary gamma solidification that differs between the two simulations. In the specified phases (P, σ, and μ) plot ThermoCalc predicts that only P phase will form at 1285 °C, which agrees well with the experimentally determined 1277 °C secondary constituent precipitation. However, if the user allows ThermoCalc to predict from all the phases in its database which phases will form it is seen that it predicts M_6C and NiMo. These phases are not present in this alloy system. This result shows that some knowledge of the alloy system is required for ThermoCalc to be accurate in its predictions.

4.5 Solidification Diagrams

ThermoCalc was also used to calculate solidification diagrams, or liquidus projections for multi-component alloys. The experimental niobium-bearing alloys (compositions can be seen in Table VI) were used to make two solidification diagrams: one pertinent to the nickel rich alloys and one pertinent to the iron rich alloys. The nickel superalloy database supplied with the ThermoCalc program is designed for alloys with a nickel content between 55-100%. The nickel rich alloys are within these compositions and the predicted diagram shows reasonably accurate prediction of the $L \rightarrow L + NbC +$ Laves reaction point (23.1 wt % Nb, 0.04 wt % C experimentally measured versus 23.4 wt % Nb, 0.02 wt % calculated), as seen in Figures 4.9 and 4.10 [4.5]. However, ThermoCalc does calculate the line of two-fold saturation between the NbC and gamma phases at lower composition than measured experimentally, as seen in the expanded view of the eutectic region (Figure 4.10). An interesting result predicted by ThermoCalc is the saddlepoint located at 6.5 wt % Nb, 0.7 wt % C in Figure 4.9. This states that if an alloy has a composition such that its primary solidification path intersects the line of two-fold saturation above the saddlepoint, the alloy shall never form laves. Instead of following the line of two-fold saturation towards the gamma/NbC/laves triple point it shall go the opposite direction. This could not be experimentally verified since this was out of the compositional range of the alloys studied.

The solidification diagram for the iron rich alloys shows more deviation from the experimentally measured eutectic. The measured γ-NbC-Laves triple point composition was 20.4 wt % Nb and 0.04 wt % C, while the calculated composition was 15.3 wt % Nb, 0.05 wt % C as seen in Figure 4.11 [4.5]. The point labeled as 2 in Figure 4.11 corresponds to the triple point. The region between point 2 and 3 show gamma, NbC, and laves precipitating from the liquid. This deviation could be a result of the compositions of the alloys that were studied. As mentioned above, ThermoCalc was optimized to calculate data for alloys where the nickel composition was between 55-100%. The average nickel composition for the iron rich alloys studied was 31.9 wt %. ThermoCalc was consistent in predicting the line of two-fold saturation between the NbC and gamma phases at lower compositions that the experimentally determined location.

4.6 Summary

ThermoCalc has been used to model many aspects of the solidification of nickel-based superalloys. It has been found to be accurate when the phases present in the microstructure are known. ThermoCalc has proven to be accurate for predicting liquidus temperatures, with an average deviation of approximately 7 °C. It is slightly less accurate in predicting solidus temperatures, where it was found that the majority of the time it underpredicts temperatures. When it deviates by >10 °C it was found that it always underpredicts the solidus temperature. There are two major elements not included in the ThermoCalc program, Si and Mn. However, through the example of Si it was found that the presence of these elements would further depress the liquidus and solidus temperature, increasing deviation for the experimental data. ThermoCalc was found to be relatively accurate in determining partition coefficients and liquidus and solidus slopes. Nb and C slopes were accurate in the experimental Nb bearing alloys, while Nb, Ti, and C were accurate in Thermo-Span, Incoloy 909, Inconel 718, and Inconel 625. Under Scheil conditions, the model predicted very accurate results when the phases in the microstructure were known previously and added in the calculation. However, when the phases were not entered in the calculation ThermoCalc often predicted phases that were not witnessed experimentally in the alloy system. ThermoCalc prediced the line of two-fold saturation for solidification diagrams in the experimental niobium bearing alloys with decent agreement. ThermoCalc was accurate in predicting the final liquid composition for the solidification diagram. It has been shown that with some knowledge of the alloy system (phases present), it is possible to get accurate results utilizing the ThermoCalc thermodynamics package.

Table I – Calculated and Experimentally Measured Liquidus and Solidus Temperatures (all values in Celsius)

Alloy	Exp. Solidus	ThermoCalc Solidus	Exp. Liquidus	ThermoCalc Liquidus
Hastelloy B2 [4.6]	1376	1392	1431	1410.9
Hastelloy W [4.6]	1333	1380.2	1396	1394.4
Hastelloy C-4 [4.1]		1370	1425	1389.3
Hastelloy C-22 [4.1]		1355.3	1395	1380
Hastelloy C-276 [4.1]		1370.2	1410	1389.9
Inconel 625 #1 [4.3]	1380	1372.3	1406.5	1391.8
Inconel 625 #2 [4.3]	1369.3	1360.8	1403	1390.8
Inconel 625 #3 [4.3]	1366.5	1373.5	1395.5	1392.6
Inconel 625 #4 [4.3]	1347.5	1359.8	1390.8	1391.6
Inconel 625 #5 [4.3]	1308	1260	1363.3	1350.3
Inconel 625 #6 [4.3]	1289.3	1247.6	1362	1349
Inconel 625 #7 [4.3]	1287.8	1263.6	1356	1351.9
Inconel 625 #8 [4.3]	1275.7	1252.8	1352	1351.1
Incoloy 909 [4.7]	1263	1270.5	1400	1381.5
Inconel 718 [4.7]	1230	1211.4	1351	1363.1
Exp. Nb #1 [4.2]	1374.4	1358.7	1420	1420.3
Exp. Nb #1.5 [4.2]	1371	1342.2	1418	1417.5
Exp. Nb #2 [4.2]		1316	1416.7	1414.2
Exp. Nb #3 [4.2]	1365.3	1363.8	1412.3	1421.7
Exp. Nb #3.5 [4.2]	1353.5	1336.2	1410.5	1416.4
Exp. Nb #4 [4.2]		1311	1407.3	1413.1
Exp. Nb #5 [4.2]	1316.5	1275.3	1391	1387.4
Exp. Nb #6 [4.2]		1292.1	1390	1383.2
Exp. Nb #7 [4.2]	1307.7	1281.7	1387.7	1390.2
Exp. Nb #7.5 [4.2]		1259.5	1382	1387.6
Exp. Nb #8 [4.2]		1295.5	1379.3	1384.3
Exp. Nb #9 [4.2]		1294.7	1430.4	1434.8
Exp. Nb #10 [4.2]		1322.3	1426.1	1427.5
Exp. Nb #11 [4.2]		1284.9	1423.9	1432.8
Exp. Nb #11.5 [4.2]		1317.6	1419.6	1424.9
Exp. Nb #12 [4.2]		1209.8	1418.8	1425.5
Exp. Nb #13 [4.2]		1227.2	1401.1	1397.1
Exp. Nb #14 [4.2]		1229	1392	1386.6
Exp. Nb #15 [4.2]		1229.8	1392.6	1390.9
Exp. Nb #16 [4.2]		1229.4	1385.6	1383
Knorovsky 718 #1 [4.8]	1320	1182	1361	1355.4
Knorovsky 718 #2 [4.8]	1315	1183.5	1363	1357.5
Knorovsky 718 #3 [4.8]	1319	1183.4	1365	1356.9
Knorovsky 718 #4 [4.8]	1324	1186	1354	1353.7
Thermo-Span [4.9]	1217	1140.5	1413	1390

Table II – Elements Included in the ThermoCalc Database and the Alloys Studied

Alloy	Ni	Al	Co	Cr	Fe	Mo	Nb	Ti	B	C	**Excluded**
Hastelloy B2	X		X	X	X	X				X	**Mn, P, S, Si**
Inconel 625	X			X	X	X	X	X		X	**Mn, P, S, Si**
Incoloy 909	X	X	X		X		X	X		X	**Si, S**
Inconel 718	X	X	X	X	X	X	X	X		X	**Si, S**
Thermo-Span	X	X	X	X	X	X	X	X	X	X	**P, S**
Exp. Nb alloys	X			X	X		X			X	**Si, S**
Hastelloy C-4	X		X	X	X	X		X		X	**Mn, P, S, Si, V, W**
Hastelloy C-22	X		X	X	X	X		X		X	**Mn, P, S, Si, V, W**
Hastelloy C-276	X		X	X	X	X		X		X	**Mn, P, S, Si, V, W**

Table III – Measured Experimental Si Liquidus Slopes and Temperature Depression

Alloy	Si m_L (^oC/wt. %)	Alloy Si Composition	Temperature Depression
Inconel 625 #1 [4.3]	-27.8	0.03	-0.8
Inconel 625 #2 [4.3]	-27.8	0.03	-0.8
Inconel 625 #3 [4.3]	-27.8	0.35	-9.7
Inconel 625 #4 [4.3]	-27.8	0.39	-10.8
Inconel 625 #5 [4.3]	-27.8	0.03	-0.8
Inconel 625 #6 [4.3]	-27.8	0.03	-0.8
Inconel 625 #7 [4.3]	-27.8	0.38	-10.6
Inconel 625 #8 [4.3]	-27.8	0.46	-12.8
Exp. Nb #1 [4.2]	-23.4	0.08	-1.9
Exp. Nb #1.5 [4.2]	-23.4	0.03	-0.7
Exp. Nb #2 [4.2]	-23.4	0.06	-1.4
Exp. Nb #3 [4.2]	-23.4	0.38	-8.9
Exp. Nb #3.5 [4.2]	-23.4	0.41	-9.6
Exp. Nb #4 [4.2]	-23.4	0.40	-9.4
Exp. Nb #5 [4.2]	-23.4	0.05	-1.2
Exp. Nb #6 [4.2]	-23.4	0.08	-1.9
Exp. Nb #7 [4.2]	-23.4	0.52	-12.2
Exp. Nb #7.5 [4.2]	-23.4	0.46	-10.8
Exp. Nb #8 [4.2]	-23.4	0.52	-12.2
Exp. Nb #9 [4.2]	-7.6	0.10	-0.8
Exp. Nb #10 [4.2]	-7.6	0.01	-0.1
Exp. Nb #11 [4.2]	-7.6	0.57	-4.3
Exp. Nb #11.5 [4.2]	-7.6	0.67	-5.1
Exp. Nb #12 [4.2]	-7.6	0.61	-4.6
Exp. Nb #13 [4.2]	-7.6	0.02	-0.2
Exp. Nb #14 [4.2]	-7.6	0.08	-0.6
Exp. Nb #15 [4.2]	-7.6	0.66	-5.0
Exp. Nb #16 [4.2]	-7.6	0.64	-4.9

Table IV – Calculated and Measured Liquidus and Solidus Slopes and Partition Coefficients

Alloy	Calc. liquidus slope	Meas. liquidus slope	Calc. solidus slope	Meas. solidus slope	Calc. partition coefficient	Meas. partition coefficient
625	-12.2 (Nb)	-11.1 (avg)	-23.8 (Nb)	-20.6 (avg)	0.51	0.54 (avg)
625	-46.8 (C)	-108.6 (avg)	-428.4 (C)	-507.4 (avg)	0.11	0.21 (avg)
Thermo -Span	-10.4 (Nb)		-29.3 (Nb)		0.36	0.42
Thermo -Span	-17.9 (Ti)		-34.8 (Ti)		0.51	0.58
Incoloy 909	-9.7 (Nb)		-26.7 (Nb)		0.36	0.49
Incoloy 909	-17.2 (Ti)		-32.9 (Ti)		0.52	0.65
Inconel 718	-12.1 (Nb)	-10	-30.0	-21	0.41	0.47

Table V – Measured and Calculated Solidus and Liquidus Slopes and K Values

Element	Data	m_l (°C/wt%)	m_s (°C/wt%)	K (unitless)	Reference
Multi-Component Alloys					
Nb	Calculated	-11.0	-24.0	0.46	This work
Nb	Measured	-8.3	-17.9	0.46	
C	Calculated	-54	-339	0.16	This work
C	Measured	-109	-507	0.21	
Binary Alloys					
Nb	Measured	-8.4	-11.2	0.75	
C	Measured	-70	-250	0.28	

Table VI – Experimental Nb-Bearing Alloy Compositions [4.5]

Alloy	Fe	Ni	Cr	Nb	Si	C	P	S
1	10.49	68.53	18.90	1.93	0.08	0.017	0.004	0.003
1.5	10.75	67.95	19.21	2.00	0.03	0.052	0.004	0.003
2	11.12	68.20	19.12	1.95	0.06	0.132	0.004	0.002
3	10.70	68.11	19.02	1.82	0.38	0.010	0.004	0.003
3.5	10.39	66.80	19.29	1.94	0.41	0.075	0.004	0.003
4	10.72	67.60	19.08	1.91	0.40	0.155	0.004	0.001
5	10.84	65.79	18.98	5.17	0.05	0.013	0.005	0.010
6	10.88	65.22	18.89	4.87	0.08	0.161	0.005	0.007
7	10.70	65.53	19.30	4.86	.52	0.010	0.005	0.009
7.5	10.82	63.93	18.54	4.92	0.46	0.081	0.005	0.004
8	10.8	64.96	18.90	4.72	0.52	0.170	0.005	0.007
9	46.03	33.56	19.31	1.66	0.10	0.003	0.006	0.003
10	46.69	32.80	19.70	1.66	0.01	0.108	0.006	0.002
11	45.38	32.80	19.53	1.77	0.57	0.004	0.006	0.002
11.5	47.38	31.05	19.64	1.84	0.67	0.116	0.006	0.001
12	45.28	32.39	19.89	1.93	0.61	0.079	0.006	0.002
13	44.55	31.24	19.63	4.42	0.02	0.015	0.007	0.003
14	44.05	31.93	19.52	4.51	0.08	0.210	0.006	0.002
15	45.40	30.03	19.54	4.88	0.66	0.010	0.007	0.003
16	44.47	30.89	19.45	4.77	0.64	0.216	0.006	0.002

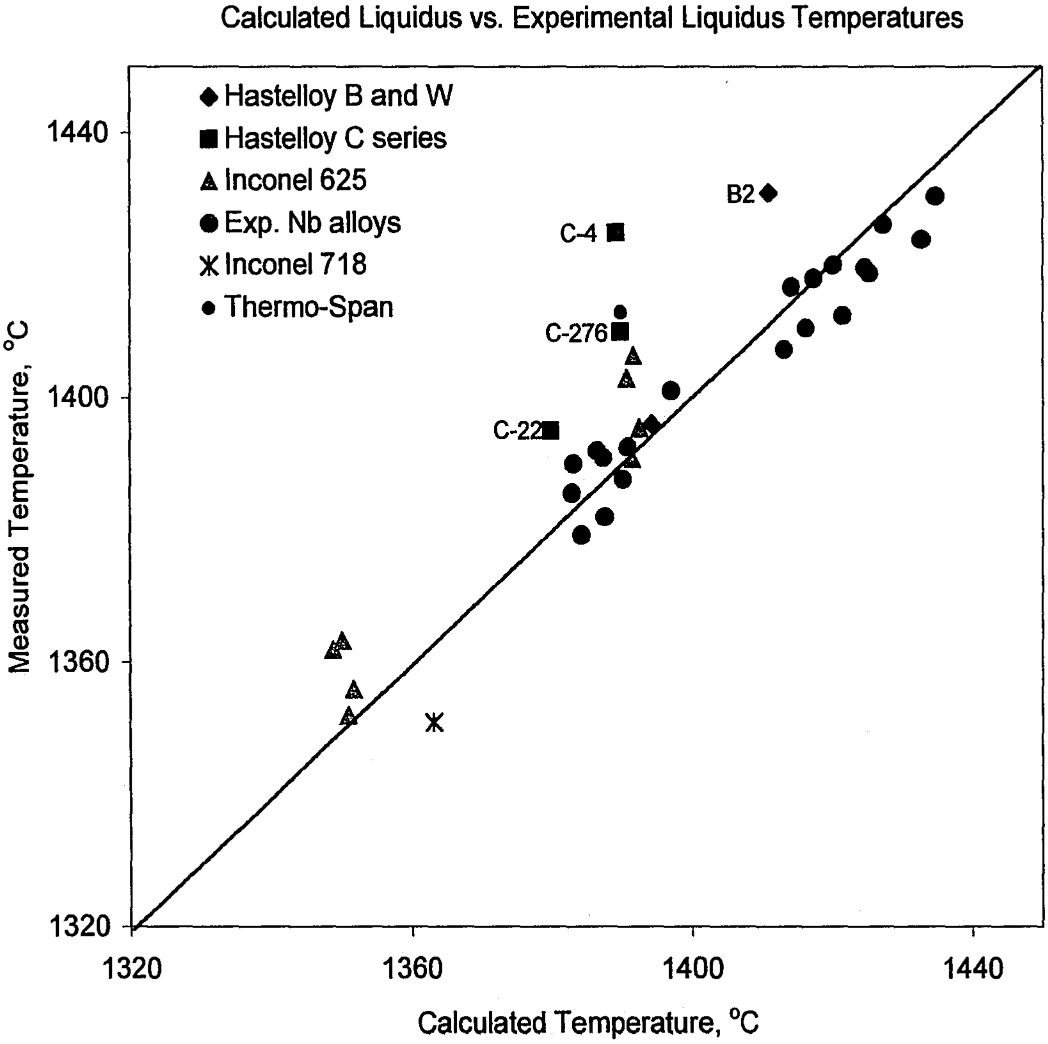

Figure 4.1 – Comparison between calculated and measured liquidus temperatures.

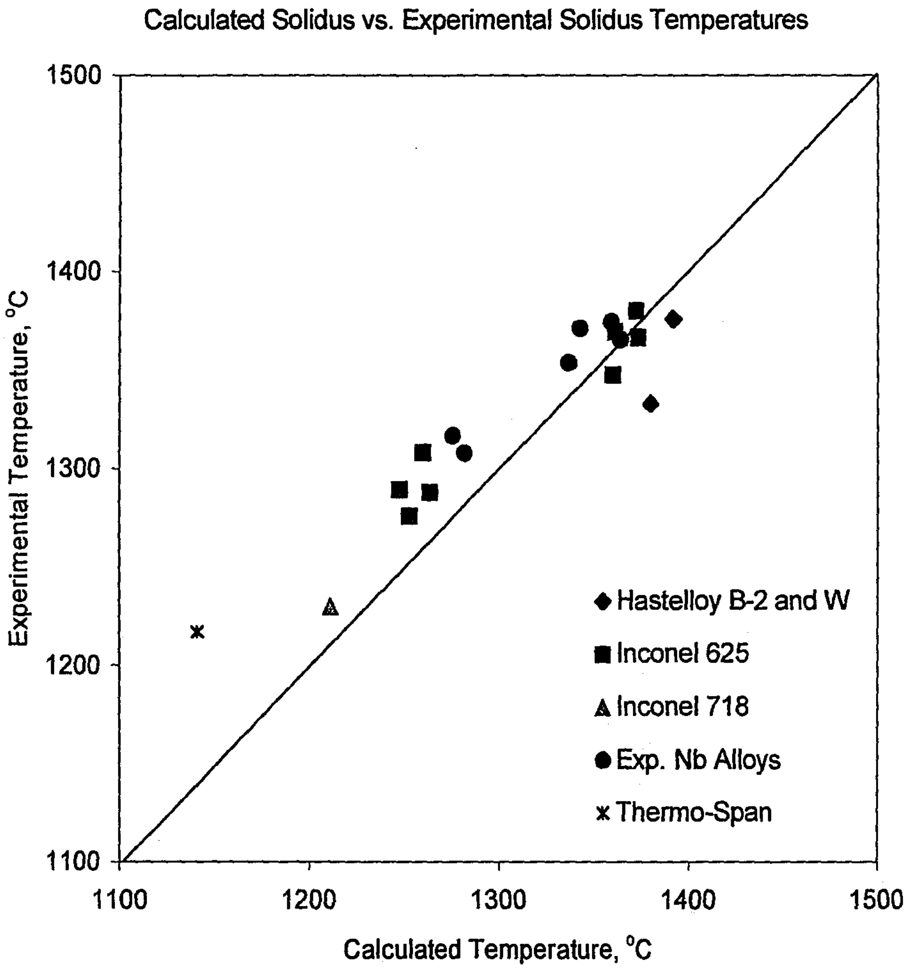

Figure 4.2 – Comparison between calculated and measured solidus temperatures.

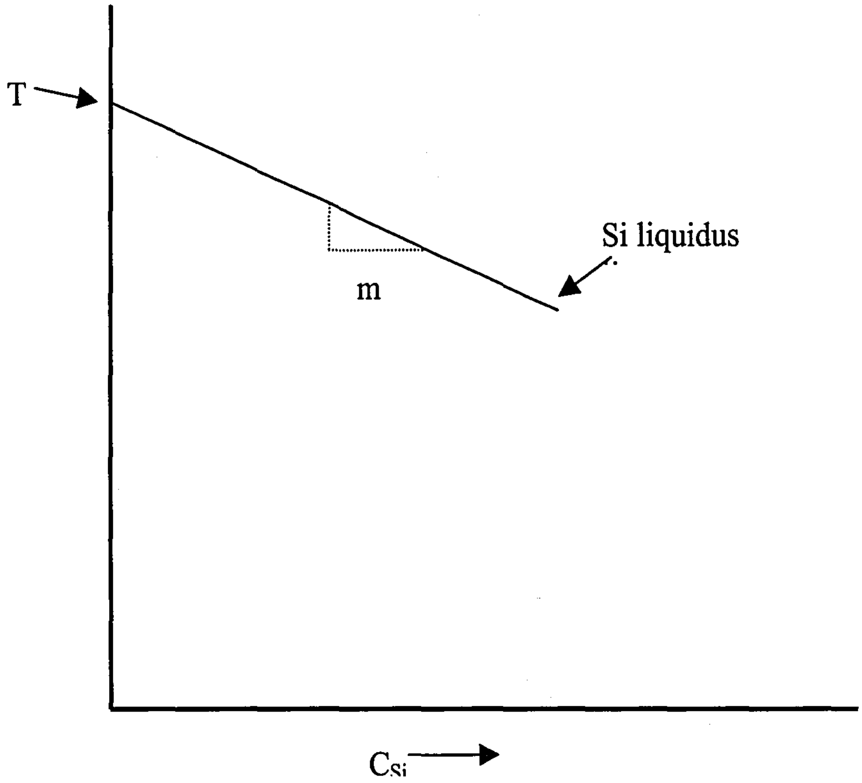

Figure 4.3 – Schematic of the liquidus line for Si.

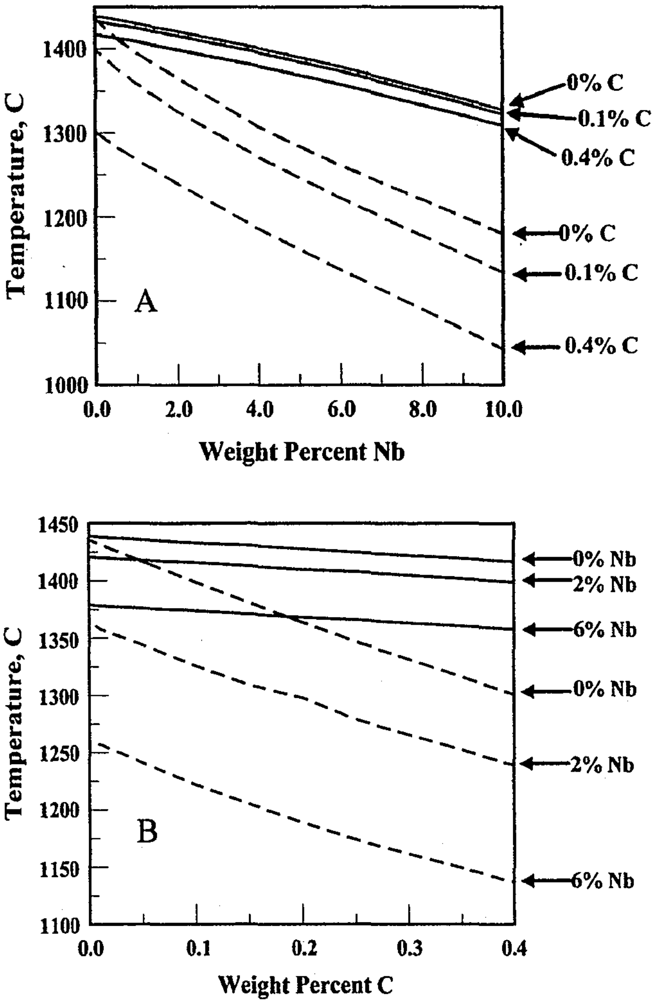

Figure 4.4 – A) Liquidus (solid) and solidus (dashed) lines for Nb as a function of C content. B) Liquidus (solid) and solidus (dashed) lines for C as a function of Nb content.

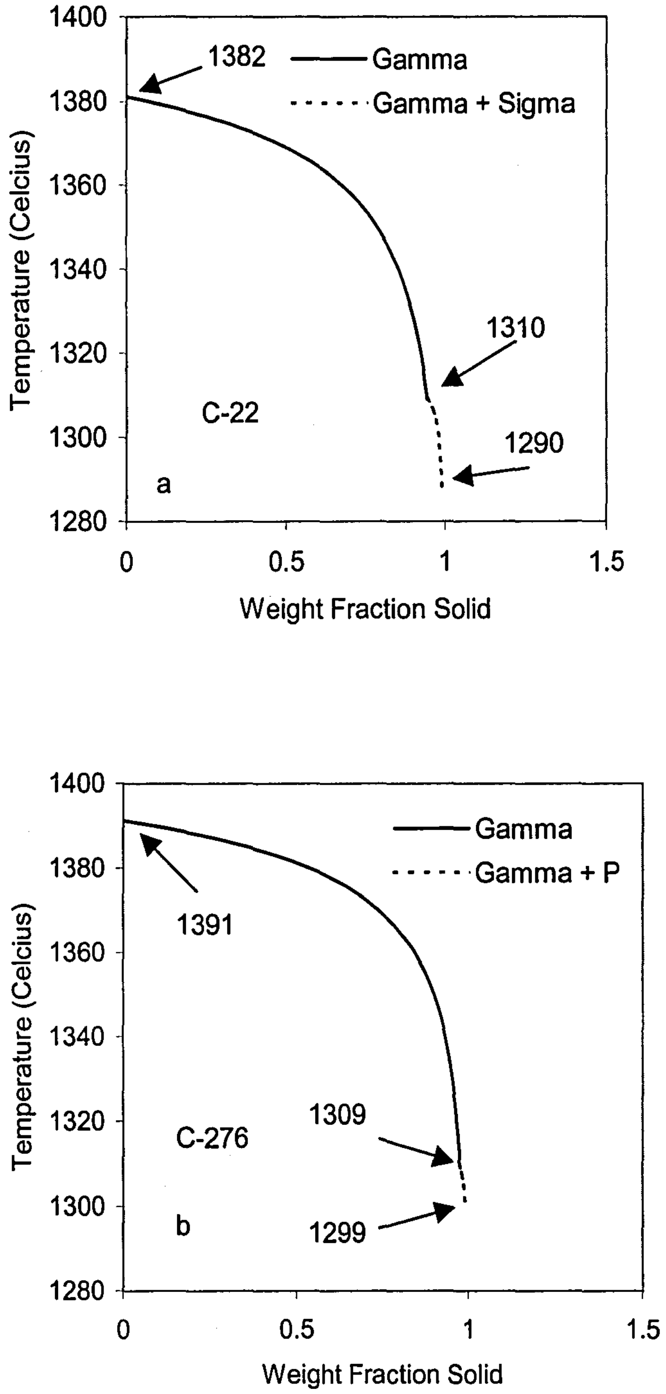

Figure 4.5 – Temperature versus weight fraction plots for Hastelloy Alloys C-22 (A) and C-276 (B). The calculations were performed assuming Scheil solidification.

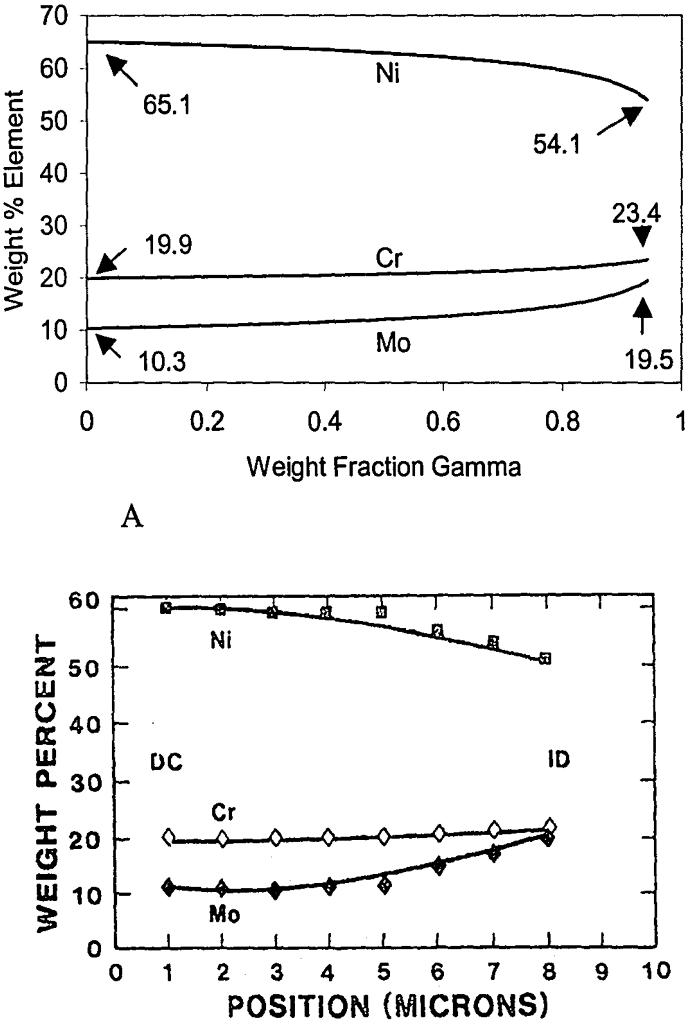

A

B

Figure 4.6 – Variation of Cr, Ni, and Mo in the primary gamma phase during Scheil solidification of C-22. A) calculated data, B) measured data.

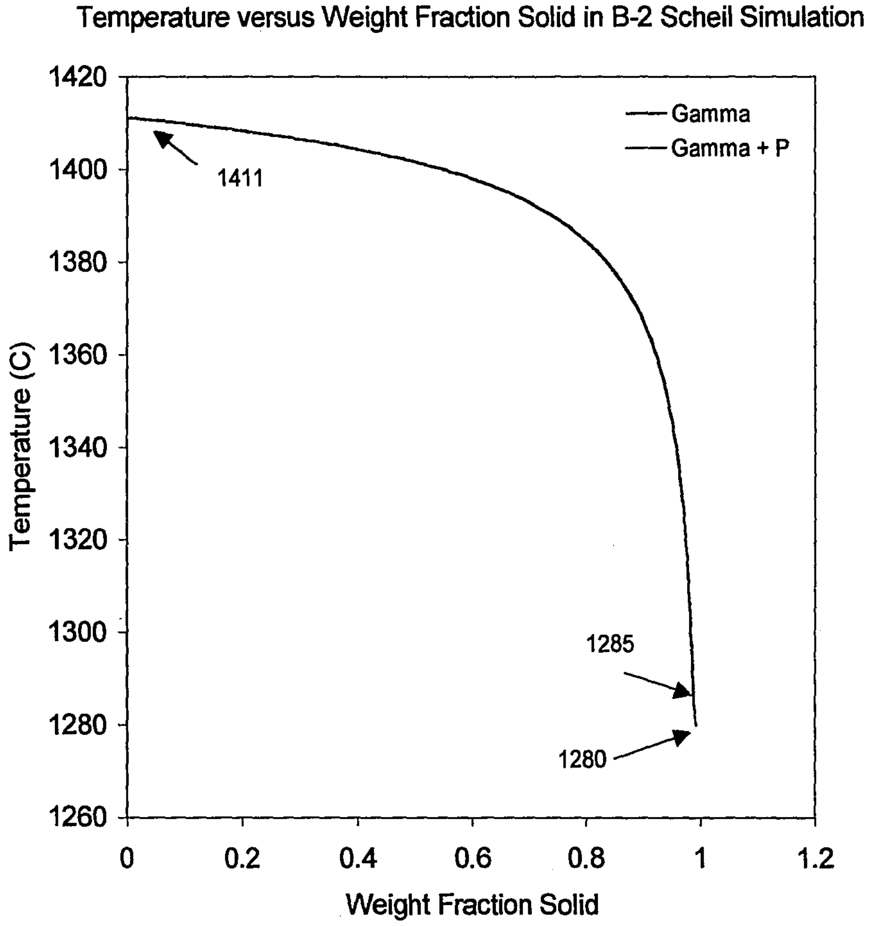

Figure 4.7a – Temperature vs. weight fraction solid for Hastelloy B2 Scheil simulation.

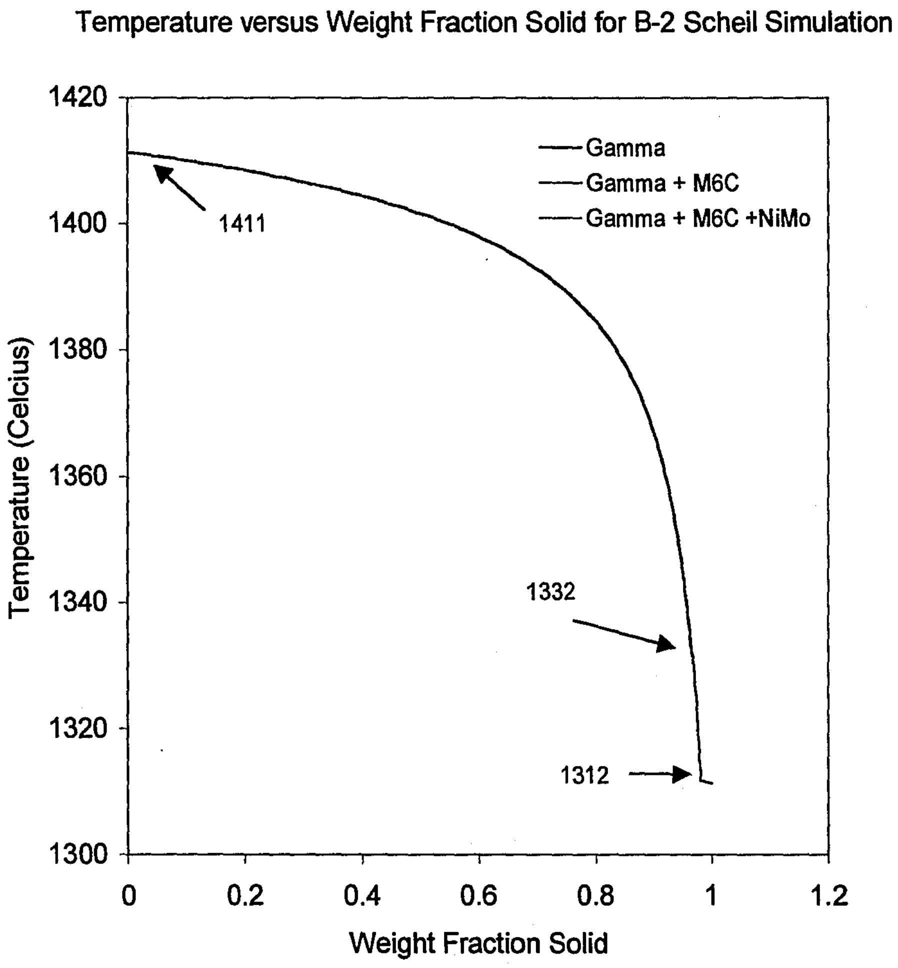

Figure 4.7b - Temperature vs. weight fraction solid for Hastelloy B2 Scheil simulation (all phases included).

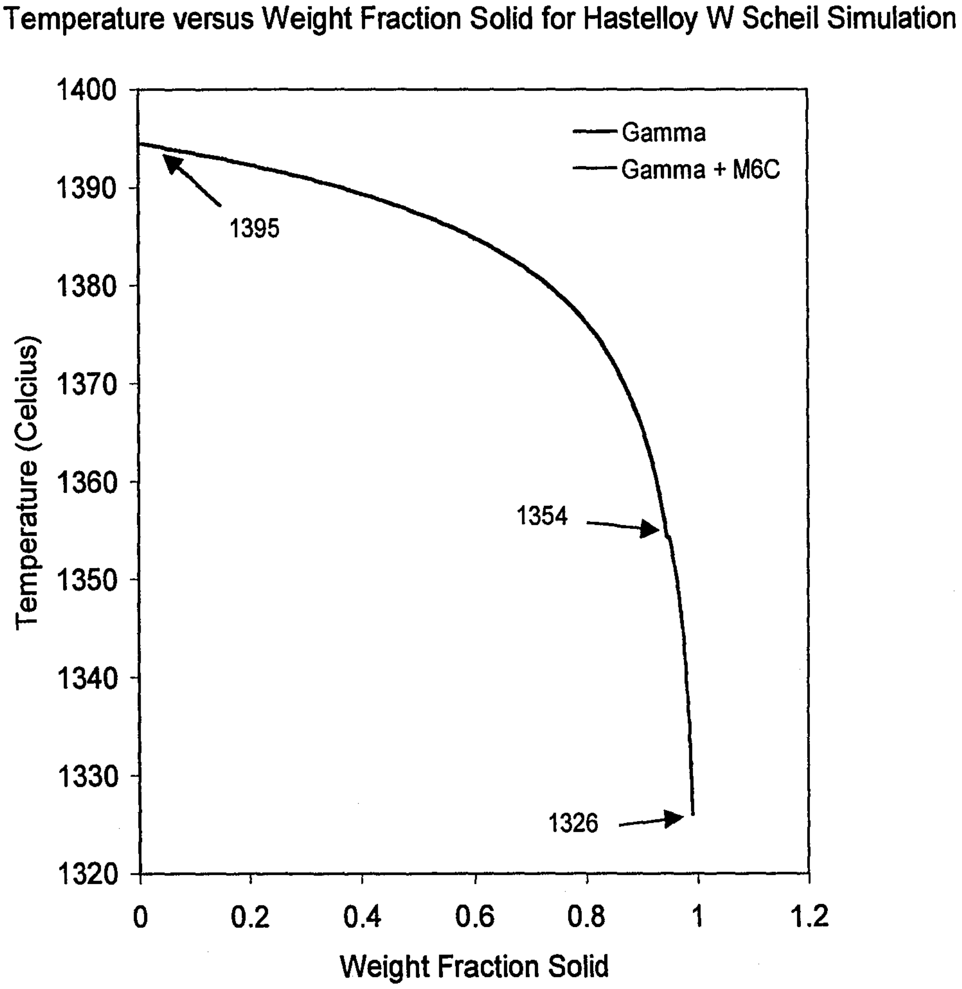

Figure 4.8 – Temperature versus weight fraction solid for Hastelloy W Scheil simulation.

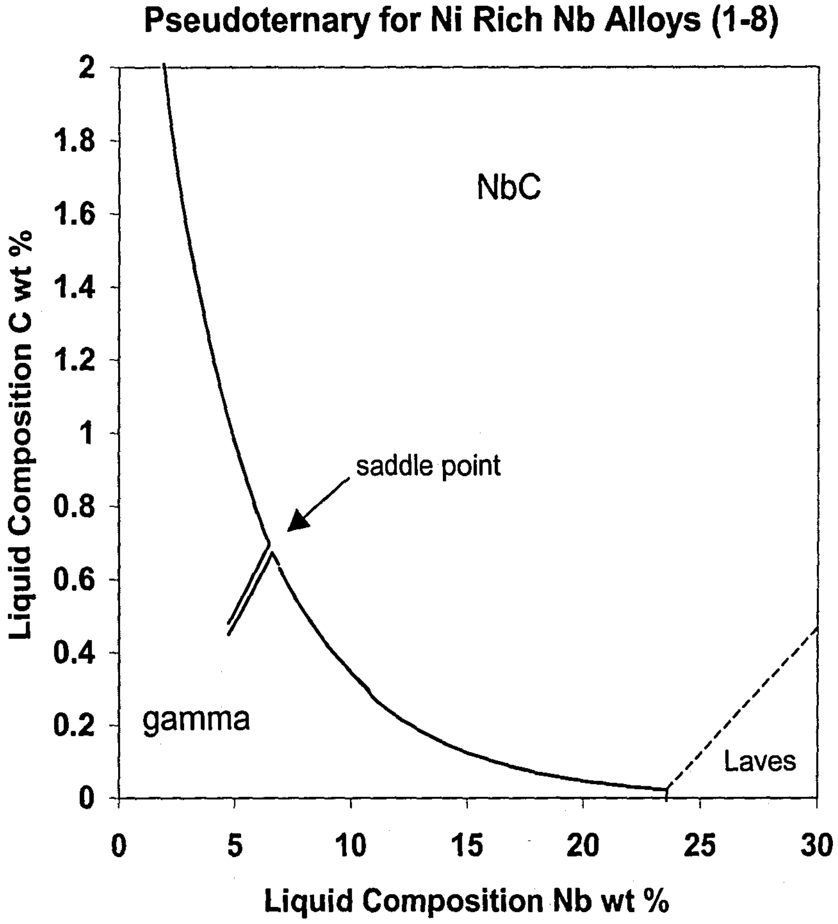

Figure 4.9 – Solidification diagram for Ni rich experimental Nb alloys. Triple point between γ, NbC, and Laves phases is at 23.4 wt% Nb and 0.02 wt% C.

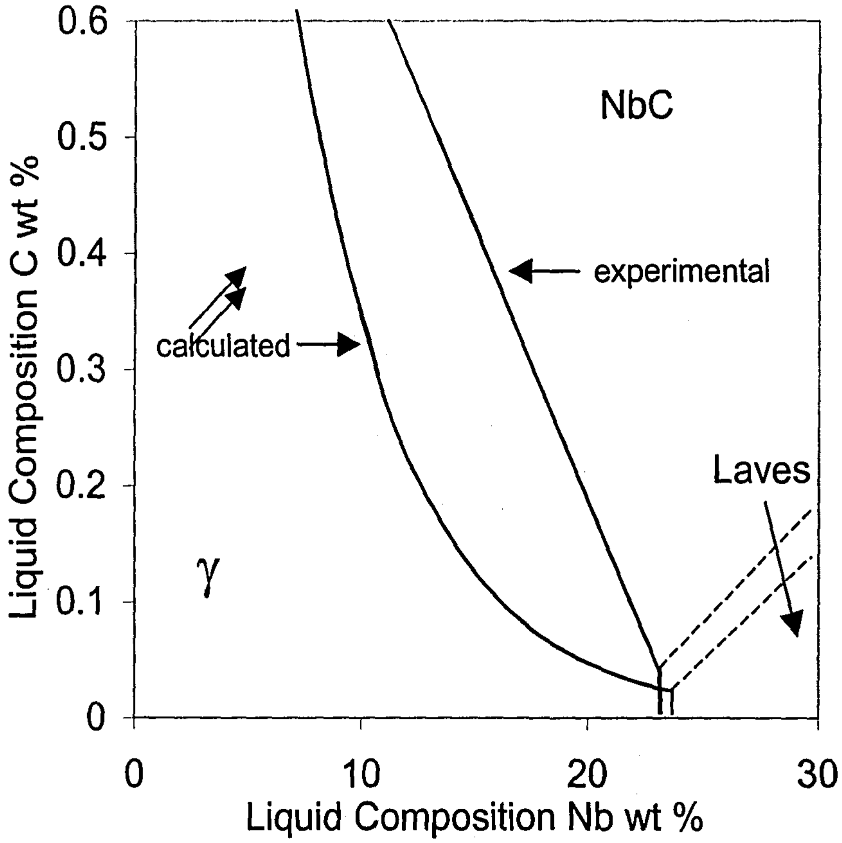

Figure 4.10 – Closeup of Ni rich diagram. The experimental triple point between γ, NbC, and Laves was 23.1 wt% Nb, 0.04 wt% C while the calculated triple point was 23.4 wt% Nb, 0.02 wt% C.

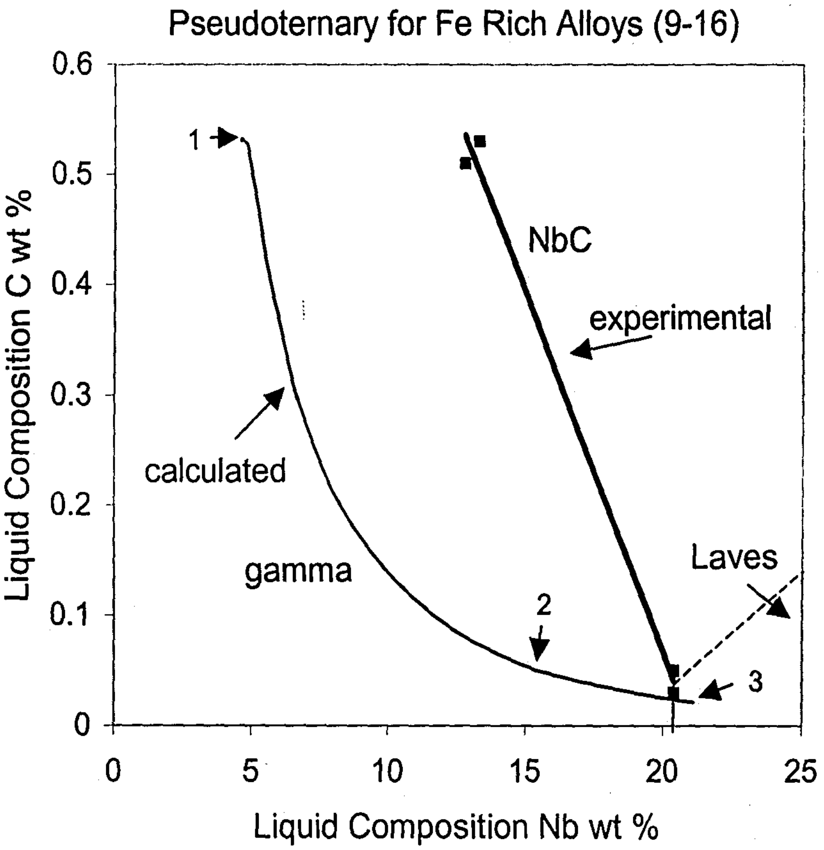

Figure 4.11 – Fe rich experimental Nb alloy solidification diagram.

5.0 Results and Discussion

5.1 Melting Efficiency

The melting efficiency is a very important process characteristic. The melting efficiency is defined as the ratio of the energy entered into the base metal to the energy used to melt the base metal, or:

$$\eta_m = \frac{Q_m}{Q_i} \qquad (5.1)$$

where Q_m is the energy used in melting the base metal and Q_i is the total energy imparted on the base metal. It is important to maximize the melting efficiency so that no excess heat is imparted on the base metal. η_m is always less than one since energy is lost to the base metal through thermal conduction (this heat creates the heat affected zone as well as raise the base metal above ambient temperature) [5.1]. The maximum melting efficiency is 0.48 for 2D heat flow and 0.37 for 3D heat flow. Laser welding is often thought to possess an inherently high melting efficiency value since it is a high energy density process. The extreme depth of penetration seen in laser welding can create heat flow conditions that are or approach pure 2D heat flow, thus maximizing melting efficiency. It is desirable to measure the melting efficiency for the welds studied to determine if the maximum melting efficiency (and thus optimum processing parameters) have been attained.

A direct technique to measure the Q_m term is to measure the volume of the weld fusion zone and multiply it by the enthalpy change, δh, required to bring the base metal to the liquidus temperature:

$$\delta h = \Delta h_f + \int_{T_r}^{T_l} c_p(T)dT \qquad (5.2)$$

where Δh_f is the heat of fusion, T_r is room temperature, T_l is the liquidus temperature, and c_p is the specific heat [5.6]. The weld volume is measured by multiplying the weld length by the cross-sectional area, detemrined metallographically. Thus, it follows that the melting efficiency can be expressed as:

$$\eta_m = \frac{V\delta h}{Q_i} \qquad (5.3)$$

where V is weld fusion zone volume.

It has been shown before that the melting efficiency depends on weld power, travel speed, and base material [5.6]. It is therefore useful to determine a parameter that accounts for these variables. Fuerschbach has devised a method for determining the melting efficiency via dimensionless analysis, a powerful technique to determine the efficiencies under which a welding process is operating [5.6]. In this technique, Fuerschbach defines two dimensionless parameters, Ry and Ch:

$$Ry = \frac{Q_i v}{\alpha^2 \delta h} \qquad (5.4)$$

$$Ch = \frac{v^2 A}{\alpha^2} \qquad (5.5)$$

where v is the travel speed, α is the thermal diffusivity, δh is the melting enthalpy, and A is the weld cross sectional area. The melting efficiency is determined to be the ratio of Ch to Ry:

$$\eta_m = \frac{Ch}{Ry} = \frac{vA\delta h}{q_i} \qquad (5.6)$$

Thus, it is possible to determine the melting efficiency of a process by knowing Ch and Ry.

Figure 5.1 illustrates the melting efficiency versus the travel speed. In this graph it is seen that the melting efficiency increases with travel speed. It is also noticed that for a given travel speed, there are two distinct groupings for the melting efficiency. This is the effect of weld power on the melting efficiency. As the power is increased, the melting efficiency increases as well. In general, there has been relative difficulty relating the melting efficiency to the travel speed alone; there is seen to be considerable scatter in the data due to other parameters (the effect of weld power is seen distinctly here) [5.1].

To eliminate these two variances, plotting the melting efficiency versus the product of the net power and travel speed has been suggested in the literature [5.2]. Fuerschbach [5.6] and DuPont and Marder [5.1] found that the melting efficiency does depend on this product and is independent of welding process used. Figure 5.2 shows this plot and it is seen that the wide variances in melting efficiency for a given travel speed are eliminated. It is also noticed that the melting efficiency reaches a maximum value of 0.43, which is between the maximum values of 0.37 for 3D and 0.48 for 2D heat flow. However, the data is still increasing and has not reached an asymptotic limit. Since the data is still increasing, there is a chance that it will approach pure 2D heat flow. To prove that the welds will not reach the 0.48 melting efficiency limit, the weld cross section was examined. It is expected that the weld pool would be in between 3D and 2D shapes since the melting efficiency was greater than 0.37 but less than 0.48. As seen in Figure 5.3, this is the case. Figure 5.3 illustrates a typical weld for the dissimilar metal weld series, where the 2D and 3D regions have been mapped out and labeled. The 2D heat flow regions correspond to the vertical sections of the fusion zone. In these regions it is known that there is no heat flow in the z direction since the weld fusion line is parallel to the z direction. Since the fusion line represents an isotherm of constant temperature, there is no temperature change (and thus no heat flow) in the z direction in these regions. Since there is not heat flow in the Z direction, heat flow is only in two dimensions (the X and Y directions) and 2D heat flow arises. Wherever the fusion line is not vertical corresponds to the 3D heat flow regions. In these regions heat flow does occur in the z (as well as x and y) directions.

It is important to understand why the melting efficiency increases with travel speed and power as shown in Figure 5.2. This can be explained if the weld is thought of as a competition between energy input being used to melt base metal and energy output conducted away from the fusion zone. If the rate of energy transport to the base metal is increased, less time is available to conduct this energy away and the melting efficiency increases [5.1]. Thus, holding all other weld variables constant, increasing the weld power will increase the melting efficiency of the weld.

The same argument can be made for increasing travel speed and holding weld power constant. Consider a point in the fusion zone for a slow travel speed. As the laser passes over this point, energy is conducted away into the base metal. If the travel speed is increased, there is less time to conduct the same amount of energy away from the weld and a larger fraction of the energy is used to melt base metal. As a result the melting efficiency increases [5.1]. This concept can be thought of as a laser dwell time. At slow travel speeds the laser remains at an arbitrary point in the weld pool longer than at high travel speeds. Thus, there is more time for energy to disperse into the base metal due to the larger laser dwell time.

It is important to remember that while the melting efficiency increases with travel speed the actual amount of base metal melted decreases. Figure 5.4A and Table I illustrates the penetration depth and weld pool width as a function of travel speed (holding beam position constant) for the two laser powers used. It is seen that both the depth and width decrease with increasing travel speed at a fixed power level. This can be explained by from the concept of laser dwell time discussed above. As the dwell time decreases (travel speed is increased), less total energy is introduced into the base metal. Therefore, there is less total energy to melt the material, resulting in smaller widths and penetration depths. Physically this can be seen in Figure 5.4B, which illustrates weld pool shapes at three different travel speeds. For a given beam position and weld power, increasing the travel speed increases the melting efficiency but decreases the total energy input in the base metal.

Table I – Laser Weld Dimensions as a Function of Travel Speed

Power, W	Travel Speed, mm/s	Width, μm	Penetration, μm
1200	8.5	3026	2621
600	8.5	2014	1461
1200	16.9	2070	2177
600	16.9	1404	1239
1200	25.4	1745	2099
600	25.4	1140	1161
1200	33.9	1529	1877
600	33.9	1001	1074
1200	42.3	1283	1780
600	42.3	892	919
1200	50.8	1170	1712
600	50.8	883	803
1200	59.3	1096	1625
600	59.3	848	880
1200	67.7	1094	1655
600	67.7	843	909
1200	76.2	1079	1683
600	76.2	857	880

Another factor affecting weld pool size was the laser beam position and resultant dilution of the dissimilar metal welds. As beam position was varied relative to the interface between the Ni200 and Hastelloy B2, different amounts of each base metal were melted. Figure 5.5 and Table II portray weld dimension (width and depth) vs. dilution for constant travel speed (34 mm/s). It is seen that the weld dimensions decrease with increasing fraction of Ni200 melted, indicating that the thermal properties for Ni200 are different than those for Hastelloy B2. It is important to note that this effect is not caused by the physical interface between the Hastelloy B2 and the Ni200. The only welds that did not melt across the interface were those performed at –1 mm. All other welds melted Ni200 and thus the Ni200 thermal properties played a role in weld pool size.

Table II – Laser Weld Dimensions as a Function of Dilution

Power, W	Area % Ni200	Width, μm	Depth, μm
1200	0	1694	2147
600	0	1167	1287
1200	0.026	1544	2079
600	0.005	1054	1229
1200	0.168	1563	1964
600	0.107	1073	1200
1200	0.37	1460	1954
600	0.288	1036	1171
1200	0.544	1529	1877
600	0.52	1001	1074
1200	0.693	1426	1906
600	0.789	989	1064

The thermal properties that affect the weld pool size are the thermal diffusivity and the melting enthalpy. Given constant energy input, if the thermal diffusivity increases less base metal shall melt. The increased thermal diffusivity allows the energy to be removed quicker, which will have the effect of melting less base metal. The melting enthalpy refers to the energy required to bring the material up to the liquid state from room temperature. If a material has a high melting enthalpy, more energy will be required to melt a given amount of material. Examining Figure 5.5 and 5.6A show a decrease in weld dimensions as more Ni200 is melted. This suggests increased thermal diffusivity and/or increased melting enthalpy over Hastelloy B2. These trends can be seen physically in Figure 5.6B-G. As more Ni200 is melted, weld fusion zone size decreases visibly. The thermal properties of Ni200 are shown in Table III below. Thermal properties for Hastelloy B2 could not be found, however, it is assumed that they will be similar to the Ni200.

Table III – Thermal Properties for Ni200

Material	Thermal Diffusivity (mm^2/s) at T_m	Melting Enthalpy (J/mm^3)
Ni200	22.0*	2.7**

*Fuerschbach, P.W. *The Metal Science of Joining*, ed. M.J. Cieslak, TMS, 1992, pp.25.
**Baricco, M., L. Battezzati, and P.Rizzi. *Journal of Alloys and Compounds*, Vol. 220, 1995, pp. 214.

Examination of Figures 5.5 and 5.6 show that as more Ni200 is melted the weld pool size decreases. Close examination of Figures 5.6B-G shows that there is a material interface that will affect the heat flow, and thus the shape of the weld pool. The interface shall inhibit heat flow, and thus increase the size of the weld pool. However, in this study there is only one position (1mm from materials interface) as shown in Figure 5.6B that does not bridge the materials interface. Thus, it is impossible to prove the effect of the materials interface on weld pool size. However, for all other laser locations (Figures 5.6C-G) this interface is crossed, indicating that the Ni200 plays a role in thermal conduction in the weld pool. According to Figure 5.6A the weld pool dimensions decrease as soon as Ni200 is melted, proving that the thermal properties are different than B2.

Figure 5.7 illustrates the weld dilution as a function of travel speed holding position constant (laser located at B2/Ni200 materials interface). It is seen that there is no discernable trend as travel speed is increased. It is also noticed that the dilution is approximately the same for both the 600 W and 1200 W welds.

5.2 Solidification Velocity

The solidification velocity was determined by measuring the growth direction of the cellular microstructure. This was then related to the travel speed to get the actual solidification velocity:

$$V = R\cos\theta \qquad (5.7)$$

where V is the solidification velocity, S is the travel speed, and θ is the angle between the cell growth direction and the welding direction, as shown in Figure 5.8. The maximum solidification velocity was found by measuring the θ angle for cells that grew closest to the welding direction. The average solidification velocity was found by measuring the solidification velocity according to equation 5.7 in 20 to 25 locations throughout the weld pool in the plate surface and weld centerline geometries.

The solidification velocity was also predicted via the weld pool shape:

$$\theta = \left(90^o - \tan^{-1}\left(\frac{w/2}{L}\right)\right) \qquad (5.8)$$

and

$$\theta = \left(90^o - \tan^{-1}\left(\frac{D}{L}\right)\right) \qquad (5.9)$$

where w is the weld width, L is the weld pool length, and D is the weld penetration depth as shown in Figure 5.9A The physical derivation of equations (5.8) and (5.9) is seen in Figures 5.9B and C, where the angle α is the inverse tangent value in equations (5.8) and (5.9). It is possible to define θ as:

$$\theta = 90^o - \alpha \qquad (5.10)$$

where α is defined as:

$$\alpha = \tan^{-1}\left(\frac{D}{L}\right) \qquad (5.11a)$$

and

$$\alpha = \tan^{-1}\left(\frac{w/2}{L}\right) \qquad (5.11b)$$

for the tear drop and hemispherical weld pool shapes respectively. It is important to note that Elmer defines equations (5.8) and (5.9) differently due to a geometrical error [5.3].

Figure 5.10 illustrates how the weld pool shape affects the cell growth morphology. The trailing edge of the weld pool determines the growth direction of the cells. In the hemispherical case of Figure 5.10, the trailing edge is very curved. Thus, the normal to this surface (the direction in which cells grow) changes with position along the liquid/solid interface. If this edge is very straight and elongated as in the teardrop condition of Figure 5.10, there is very little driving force for the cells to reorient. Given constant welding power, the hemispherical weld pool shape shall occur at slow travel speeds while the teardrop shape occurs at high welding speeds. Equation (5.8) is used when the weld pool shape is hemispherical, while (5.9) is applicable for teardrop weld pool shapes. The criterion for choosing which equation is pertinent is that for teardrop shaped weld pools the depth is shallower than the width. The measured solidification velocity is compared to the calculated solidification velocity predicted by the weld pool shape as described above in Equations 5.8 and 5.9.

Table VIIIA and VIIIB lists the maximum solidification velocity and the weld travel speeds for the autogenous B2 laser welds and GTA welds respectively. It is seen in Table IVA that the plate surface solidification velocity deviates from the travel speed near travel speeds in excess of 20 mm/s and then increases at a very slow rate with travel speed, as seen in Figure 5.11A for the laser welds. The weld centerline view solidification velocity increases to a point and then decreases at the higher travel speeds (above 50.8 mm/s). This is an important result, as it is often assumed that high solidification rates can be obtained by increasing the travel speed.

It is interesting to note that it was impossible to measure the solidification velocity in the plate surface orientation for the GTA welds, as listed in Table IVB. This is because the cells grew vertically from the bottom of the weld throughout the whole range of travel speeds, preventing measurement in the plate surface orientation. Figure 5.12A-C illustrates the GTA welds in the plate surface orientation at various travel speeds. It is seen that there are no regions of cellular growth from the weld pool sides, and thus no opportunity to measure growth velocity in this orientation.

It is also peculiar to note that the GTA welds solidified at higher solidification velocities than the laser welds (55.7 mm/s for GTA vs. 44.0 mm/s for laser), as seen in Tables IVA and IVB and Figure 5.13. It should be noted that the GTA welds were performed at a higher power (1370 W) than the laser welds (1200 W), which will affect the weld pool shape. Since the weld pool shape has a drastic effect on the solidification velocity, this will play a role in the solidification velocity differences.

Figures 5.11B-D illustrate laser weld centerline microstructures while Figures 5.14A and B portray the GTA weld centerline microstructures with cell growth directions marked. It is seen that as the travel speed increases, the angle θ between the cell growth direction and the welding direction approaches 90°. Since $\cos 90^{\circ}$ is zero, the growth velocity approaches zero in the laser welds. It is noticed that some of the angles indicated are greater than 90°, which would give a negative growth speed according to equation (5.7). This is obviously not correct since it is impossible to have a negative growth speed. These growth angles arise from the orientation of the grains in the base metal. In FCC materials, cells will preferentially grow along the six <100> directions. Whichever direction is closest to the direction of heat flow will be the direction the cells grow.

Table IVA – Maximum Solidification Velocity of Autogenous Laser Welds

Travel Speed, mm/s	Solidification Velocity, mm/s Plate Surface	Solidification Velocity, mm/s Weld Centerline
8.5	8.5	8.4
16.9	16.9	16.8
25.4	20.8	22.8
33.9	19.4	27.0
42.3	31.5	38.4
50.8	26.2	44.0
59.3	34.8	42.6
67.7	38.9	35.9
76.2	38.1	28.5

Table IVB – Maximum Solidification Velocity of Autogenous GTA Welds

Travel Speed, mm/s	Solidification Velocity, mm/s Plate Surface	Solidification Velocity, mm/s Weld Centerline
10	Not Measurable	5.9
20	Not Measurable	14.9
30	Not Measurable	12.7
40	Not Measurable	31.9
50	Not Measurable	32.1
60	Not Measurable	47.3
70	Not Measurable	41.1
75	Not Measurable	55.7

It is interesting to note that after the initial increase, the solidification velocity decreases at high travel speeds for the laser weld centerline samples. This series of autogenous welds were performed at the same power, only varying the travel speed. Thus, the lower speeds would have larger heat input and a larger, more penetrating weld pool size. This can be seen in Table VA and VB below. The weld pool length for the 25.4 mm/s travel speed laser weld could not be measured. The laser beam was not terminated while traveling at 25.4 mm/s, thus the steady state weld pool shape was not retained at the end of the weld. The GTA 70 mm/s weld pool length could not be measured because the end of the weld pool was not discernable. At the higher travel speeds, the weld pool depth is seen to be very shallow for both GTA and laser welds, while the weld pool length is very long. This can be used to explain the decrease in solidification velocity in the laser weld centerline samples, but first it is useful to describe the weld pool shape as the travel speed is increased to understand the microstructure development.

Table VA – Weld Pool Geometry of Autogenous Laser Welds

Travel Speed, mm/s	Width, mm	Length, mm	Depth, mm
8.5	2.4	1.58	0.61
16.9	2.0	1.60	0.51
25.4	1.8		0.41
33.8	1.6	1.67	0.39
42.3	1.5	1.70	0.35
50.8	1.4	1.71	0.31
59.3	1.4	1.79	0.3
67.7	1.3	1.84	0.29
76.2	1.3	1.88	0.25

Table VB - Weld Pool Geometry of Autogenous GTA Welds

Travel Speed, mm/s	Width, mm	Length, mm	Depth, mm
10	4.51	4.49	0.77
20	3.54	4.57	0.52
30	3.29	3.03	0.43
40	3.16	2.97	0.33
50	2.85	3.41	0.31
60	2.42	2.81	0.19
70	2.02		0.14
75	2.27	2.4	0.17

Figures 5.10A and B illustrate a schematic of the weld pool for hemispherical and tear drop shaped weld pool welds. As the weld pool solidifies, the solid generates a heat of fusion. The transition in weld pool shape occurs when the minimal thermal gradient (which occurs at the weld centerline) cannot dissipate the generated heat of fusion quickly [5.7]. This forces the shape of the weld pool to change to the teardrop shape. The shape of the weld pool plays a major role in the microstructural evolution of the weld. In Figure 5.10, the grain morphology is shown (the cell morphology shall be similarly oriented). The hemispherical weld pool shape provides greater driving force for cell/grain competitive growth due to the hemispherical shape. Grains growth rate varies according to their orientation. Grains with <100> directions perpendicular to the solid/liquid interface will growth faster than grains with higher misorientations. Thus, the grains that grow faster will "crowd out" slower growing grains [5.7]. If the weld pool shape is hemispherical, this grain selection shall occur continuously throughout the weld pool. For teardrop shaped weld pools there is less driving force for competitive growth once growth starts. Examination of Figure 5.10B shows that the tear drop weld pool shape welds have a solid liquid interface that is relatively straight. Since this θ angle does not vary, there is no driving force for cell/grain competitive growth after growth begins. Thus, the initial high θ angle growth of initial solidification remains throughout the weld. Since the θ angle is large, solidification velocity approaches zero in the laser welds according to equation 5.7. This trend is seen in Figure 5.11A in the laser weld centerline orientation.

Figure 5.15 compares a slow travel speed to fast travel speed laser weld microstructure in the weld centerline geometry. The effect of weld pool shape can be clearly seen. Examining Figure 5.15A closely shows that new grains grow in a more preferable orientation at approximately 0.3 mm from the fusion line, while the microstructure in Figure 5.15B shows no competitive growth. Examining the shape of the laser weld pool in the plate surface orientation as seen in Figures 5.16A-H show that the weld pool shape for the 8.6 mm/s weld is hemispherical, while the 76.2 mm/s weld has a very straight trailing edge. Examining the welds incrementally shows that the transition from hemispherical to teardrop shaped weld pool occurs between 16.9 and 33.8 mm/s. Thus, welds performed at travel speeds higher than 33.8 mm/s will have growth predominantly from the bottom of the weld pool. As the travel speed is increased above 33.8 mm/s, the weld pool length increases as seen above in Table VA. Thus, the angle θ increases with travel speed in the centerline geometry and there is less driving force for cellular competitive growth.

Figures 5.17A-O illustrate the weld pool shape for the GTA weld samples. It is interesting to note that the weld pool shape is tear drop shaped at the slowest travel speed, 5 mm/s. However, this is not surprising since laser beam welding is a high energy density process. Therefore, it shall produce welds of greater depth holding all variables constant. This is verified through examination of Tables VA and VB. Even though the depths are similar, the GTA welds are approximately twice as wide. This creates a geometry that favors the tear drop shaped weld pool even at the slower travel speeds.

It is important to note that the welds studied were extremely small at the higher travel speeds. The small amount of base metal melted combined with the geometry (the width is much larger than the depth) create the decrease in solidification velocity described previously for the laser welds. It has been seen previously that the shallow penetration of tear drop shape weld pool welds has the effect of decreasing the growth velocity substantially [5.3]. Had the power been increased to create more weld penetration this trend may not have been seen.

Figure 5.18 and 5.19 compare the average solidification velocity to the travel speed for the laser welds and GTA welds respectively. The average solidification velocity was determined by averaging 20-25 measured values from various regions of the weld from the fusion line to the weld surface. The calculated curves correspond to predicted solidification velocity from the θ angle shown in equations (5.8) and (5.9). In the GTA case, only the weld centerline data is plotted (and corresponding data calculated via equation 5.9) since the plate surface orientation could not be measured. Along with the predicted solidification velocity the average solidification velocity is plotted. It is seen that there is good agreement between the predicted velocity and the measured average velocity in Figure 5.18 and reasonable agreement in Figure 5.19. One interesting point is that Elmer's teardrop shaped weld pool equation predicts solidification velocities that are lower than the hemispherical shaped weld pool equation for the laser welds. This makes sense when one examines the nature of the equations. From equations (5.8) and (5.9) above we see that:

$$\theta = \left(90^{o} - \tan^{-1}\left(\frac{w/2}{L}\right)\right) \qquad (5.8)$$

for hemispherical weld pool shapes and

$$\theta = \left(90^{o} - \tan^{-1}\left(\frac{D}{L}\right)\right) \qquad (5.9)$$

for tear drop weld pool shapes, where w is the weld pool width, D is the depth, and L is the weld pool length. Physically, these equations state that hemispherical weld pool shapes promote growth directions that are predominantly from the sides of the weld pool. Thus the angle θ is controlled by $^{w/2}\!/_{L}$. However, when the welding conditions promote tear drop shape weld pools (the weld pool depth is less than the width), the growth direction is dominated by growth from the bottom of the weld and the depth controls the solidification rate. Since the depth is so shallow for the tear drop shaped weld pool welds, this leads to slower rates. This can be seen directly in laser weld microstructures shown in Figure 5.20. In Figure 5.20A, cell growth is predominantly from the side of the weld pool rather than the bottom. For the high speed weld shown in Figure 5.20B the majority of the cells are growing in an orientation "out of the page" from the bottom of the weld. This arises from the very shallow penetration depth of the welds performed, as discussed above. Since this orientation creates a very high angle (approaching 90°) with the welding direction, growth is predicted (and measured) to be slower than the growth conditions in the hemispherical weld pool shape equation.

The weld pool shape is outlined in Figures 5.20A and B. For Figure 5.20A, the shape is very hemispherical. It is also possible to see the cell competitive growth easily, which shows the cells growing roughly perpendicular to the weld pool edge. Figure 5.20B shows hemispherical behavior at the very edge of the weld however, it then starts to form the "V" shape at the very edge of the micrograph. This transition marks the boundary between cell growth predominantly from the side to cell growth from the bottom of the weld.

The results discussed above for solidification velocity disprove the common assumption that the high growth velocities can be obtained relatively easily by increasing the travel speed. As shown in the average growth speed data the highest growth speed was on the order of 25 mm/s, where the travel speed was 76.2 mm/s. What is perhaps more important is the rate of increase in growth speed with travel speed. Considering the average growth speed as shown in Figure 5.18, the slope of the measured data from 42.3 to 76.2 mm/s had a slope of 0.19, meaning if the travel speed were increased an additional 100 mm/s the solidification velocity would increase only 19 mm/s. Thus, to get truly high solidification rates in this materials system impractical travel speeds would have to be employed, or increase power to increase depth. By increasing the weld penetration cell growth from the weld pool sides would dominate and increase solidification velocity.

5.3 Microstructural Modeling

Figure 5.21 illustrates cell spacing as a function of solidification velocity. Lines of constant temperature gradient are indicated to represent the predicted cell spacing according to the KGT model, previously discussed in section 2.4.4. The red triangles are the measured cell spacings from the autogenous laser welds at different solidification velocities. It is seen that there is good agreement between the experimental and measured data for a temperature gradient of 10,000 to 50,000 K/cm. Experimentally determined temperature gradients in electron beam welding of stainless steels of similar solidification rates have been found to be between 1.3×10^4 °C/cm to 8.0×10^4 °C/cm [5.4]. While electron beam welding is a different process, it is also a high energy density process and has similar weld pool characteristics [5.5]. Thus, the temperature gradients utilized in these KGT model calculations, while not proven with experimental measurement, are likely correct on an order of magnitude scale. Figure 5.22 compares the laser and GTA weld cell spacings. It is seen that the GTA cell spacings are approximately twice the size of the laser welds for similar growth rates. This is to be expected since cell spacing is inversely related to the cooling rate. Laser welding is a higher energy density process than GTA welding, therefore one would expect smaller cell spacings for laser welding than GTA.

The maximum solidification velocity was used when plotting the experimentally measured data. This arises from the geometry measuring the cell spacing. When measuring the cell spacing, the group of cells to be measured must be parallel to the plane of observation to give an accurate value. When the cells are parallel to the plane of viewing, this almost always corresponds to the direction of maximum growth speed as well. This is supported by the good agreement between experimental and predicted values as seen in Figure 5.21.

It is seen that the KGT predictions shows a maximum velocity of 33 mm/s for the 50,000 K/cm and 40 mm/s for the 10,000 K/cm calculations. Above these solidification velocities the cell spacing approached infinity, indicating that the KGT model predicts reversion to planar front growth above these maximum growth speeds.

Figure 5.23A illustrates the AEM measured cell core compositions as compared to the core compositions predicted by the KGT model. Figure 5.23B portrays the TEM micrograph with the compositional trace location marked. This is representative of the areas examined by AEM. Figure 5.23C illustrates the full compositional traces corresponding to the microstructure in Figure 5.23B. Figure 5.23D and E illustrate another region analyzed and a compositional trace from that region. It should be noted that the cells are oriented out of the page, thus giving a "honeycomb" appearance. It is seen that the measured compositions are consistently higher than the calculated compositions in Figure 5.23A, however there is good agreement between the measured and calculated core compositions. Figure 5.24 shows the phase diagram calculated in ThermoCalc for the Hastelloy B2 alloy. Without undercooling, it is predicted that the cell core composition would be 23 wt% Mo. However, referring to Figure 5.23A indicates that in fact the core compositions are near the nominal alloy composition of 27.3 wt% Mo, thus proving that the cells were undercooled as they solidified. Measuring off of Figure 5.24 indicates that the degree of undercooling was approximately 18.5 °C. The results from Figures 5.21 and 5.23 prove that it is possible to couple thermodynamics models and solidification models to accurately predict microstructural features of laser welded nickel alloys.

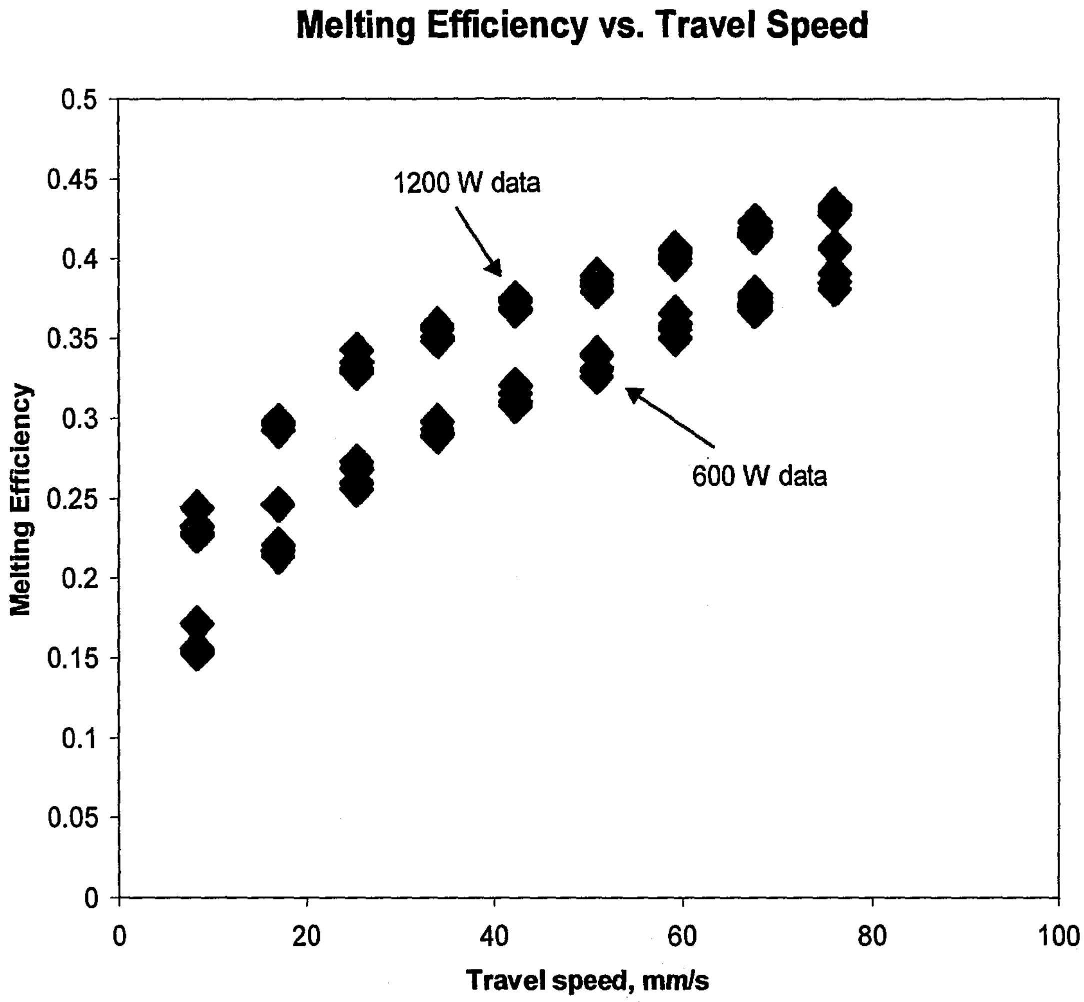

Figure 5.1 – Melting efficiency vs. travel speed for dissimilar metal laser welds.

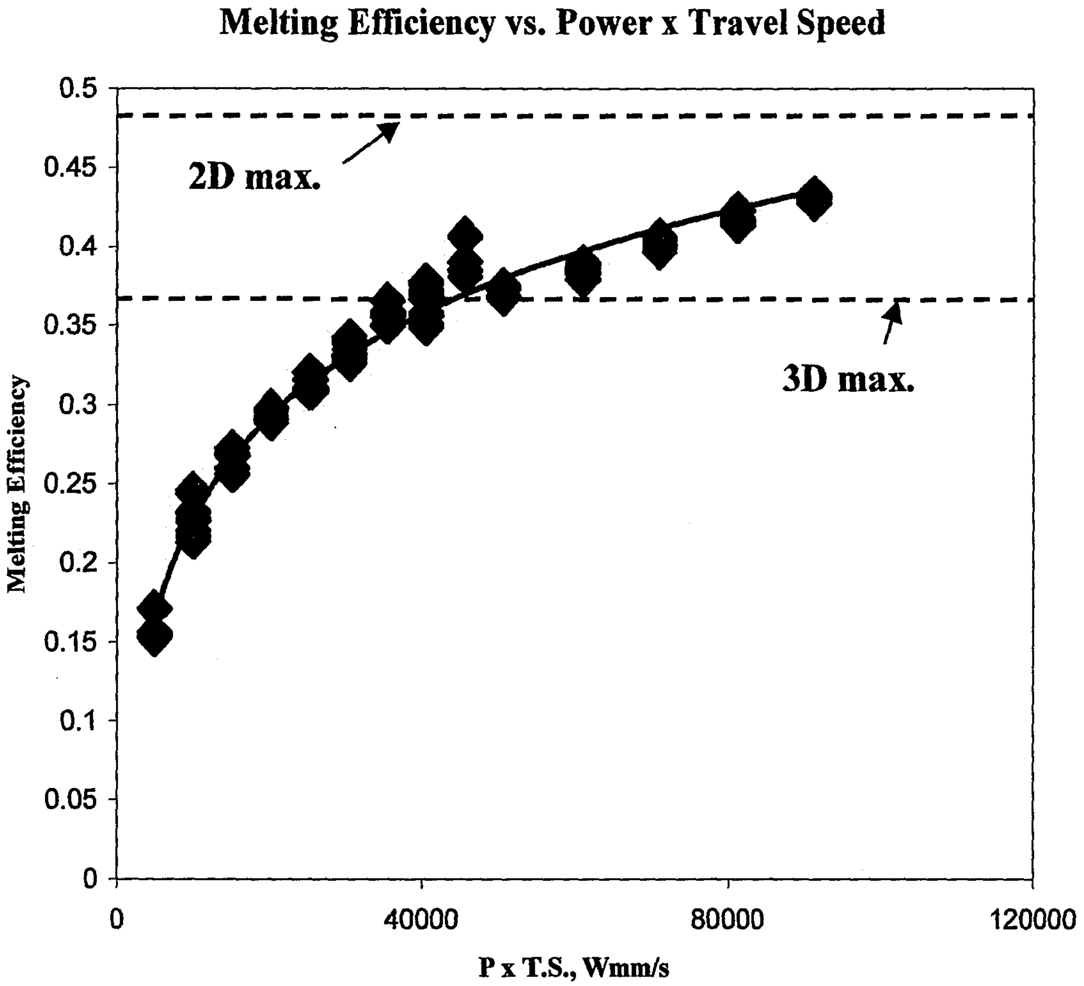

Figure 5.2 – Melting efficiency vs. product of power and travel speed for dissimilar metal laser welds.

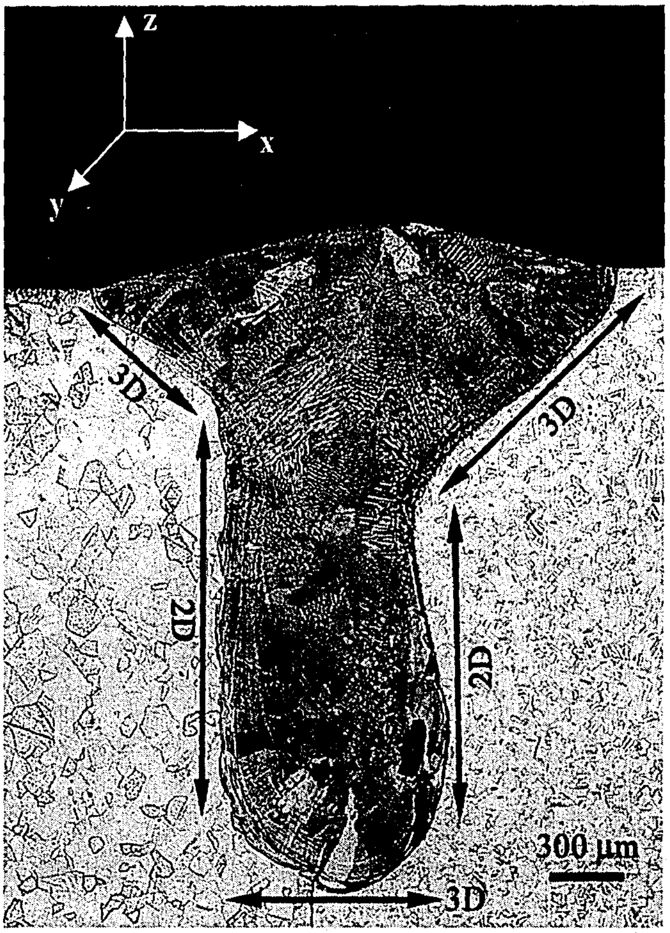

Figure 5.3 – Typical dissimilar metal laser weld with Ni200 base metal on the left. The weld pool shape is a combination of 3D and 2D heat flow conditions. Y direction is out of the page.

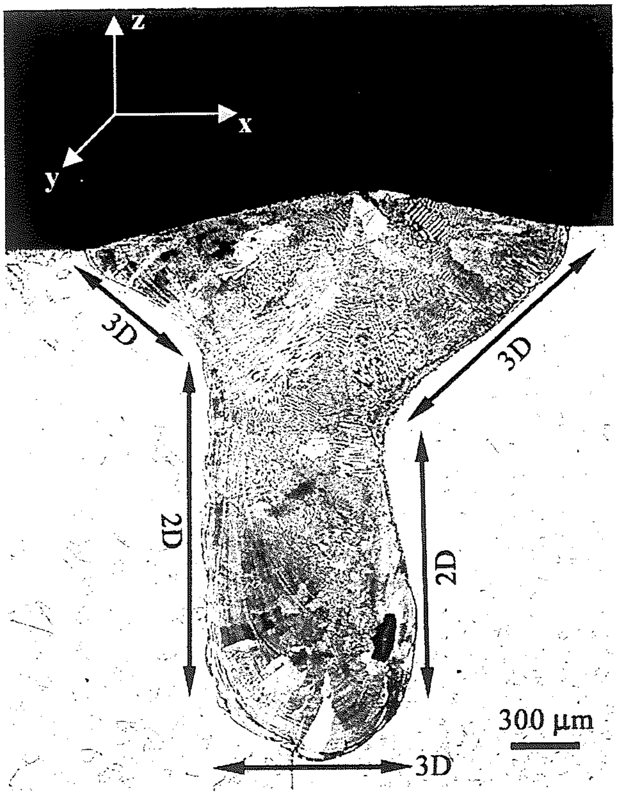

Figure 5.3 – Typical dissimilar metal laser weld with Ni200 base metal on the left. The weld pool shape is a combination of 3D and 2D heat flow conditions. Y direction is out of the page.

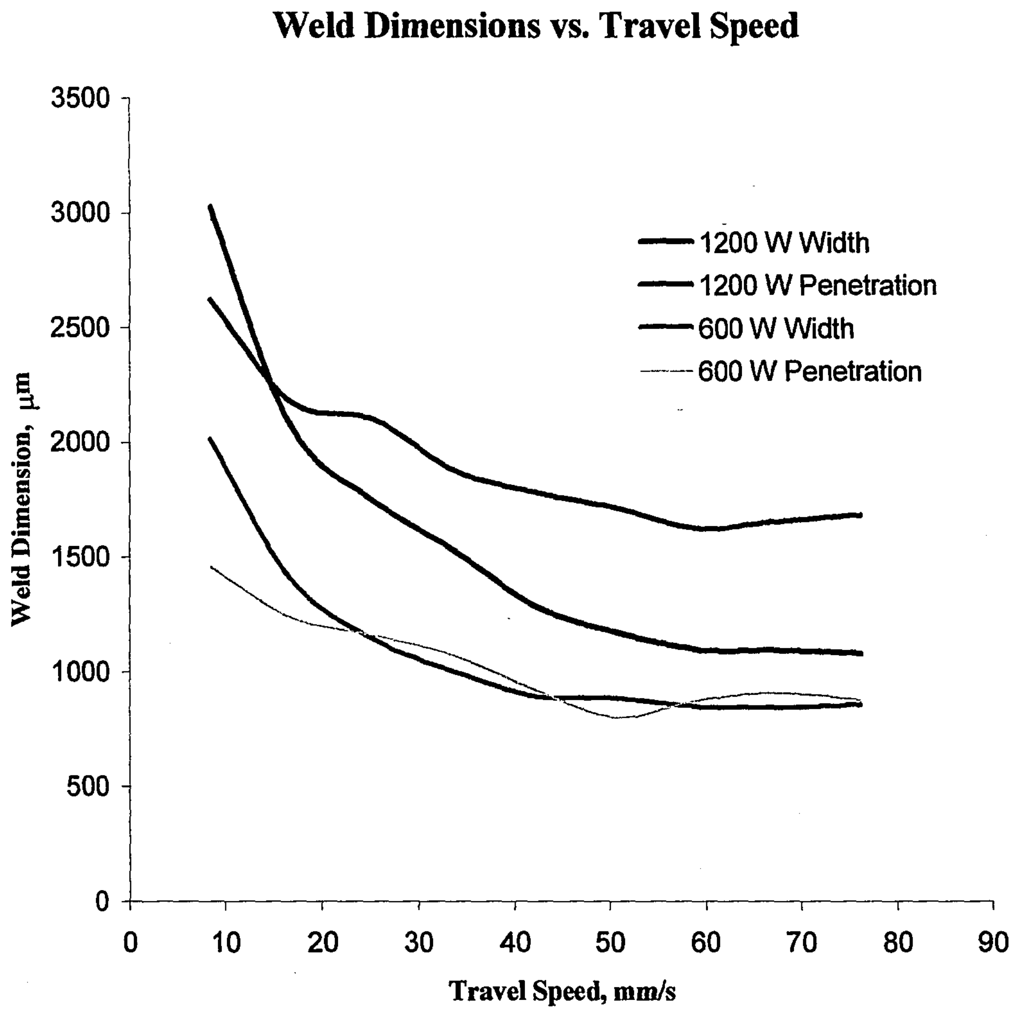

Figure 5.4 –A) Travel speed vs. weld dimensions illustrating decrease in weld size as travel speed is increased.

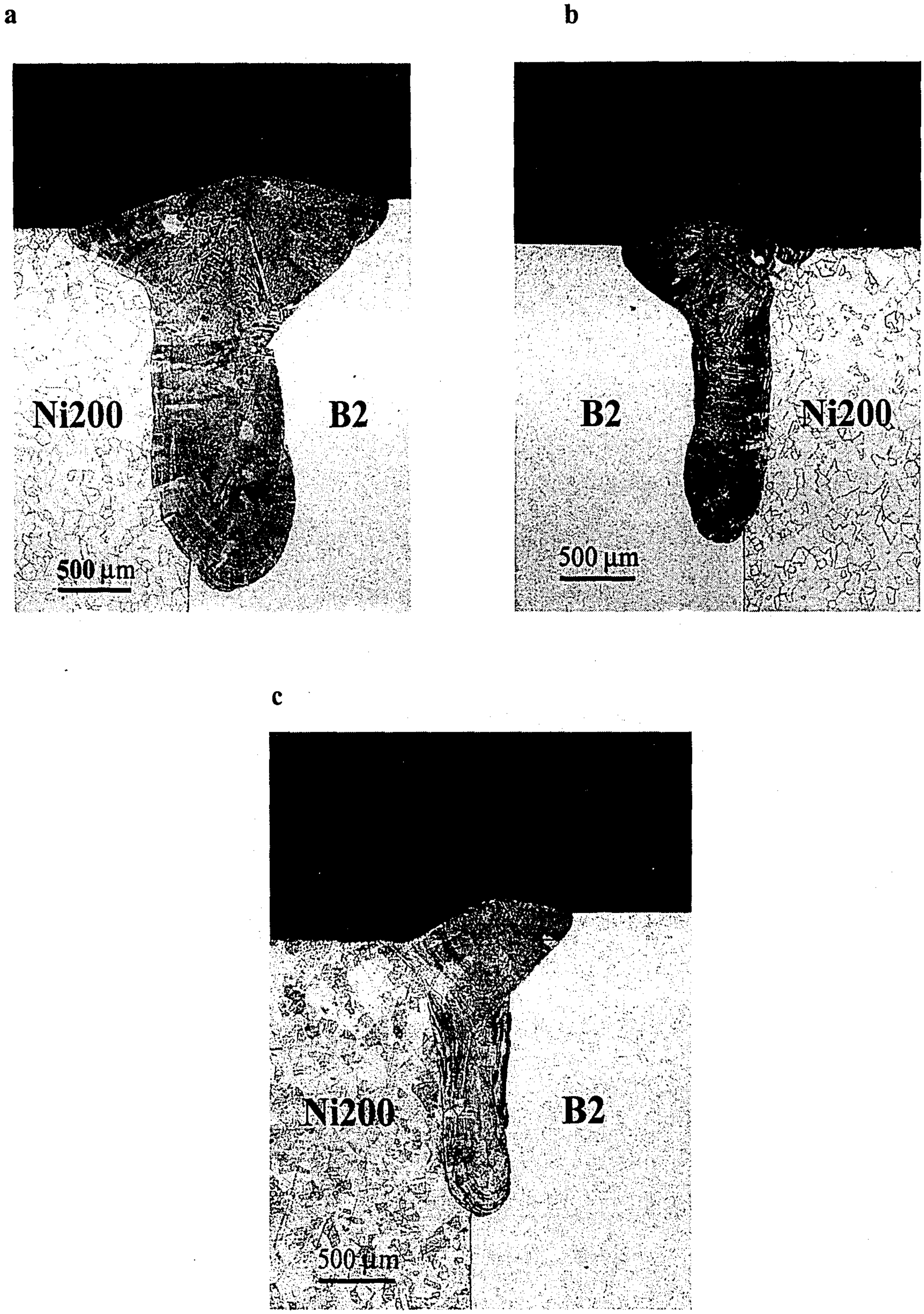

Figure 5.4 – B) Dissimilar metal welds showing dimensional changes with travel speed. a) 8/5 mm/s, b) 42.3 mm/s, c) 76.2 mm/s.

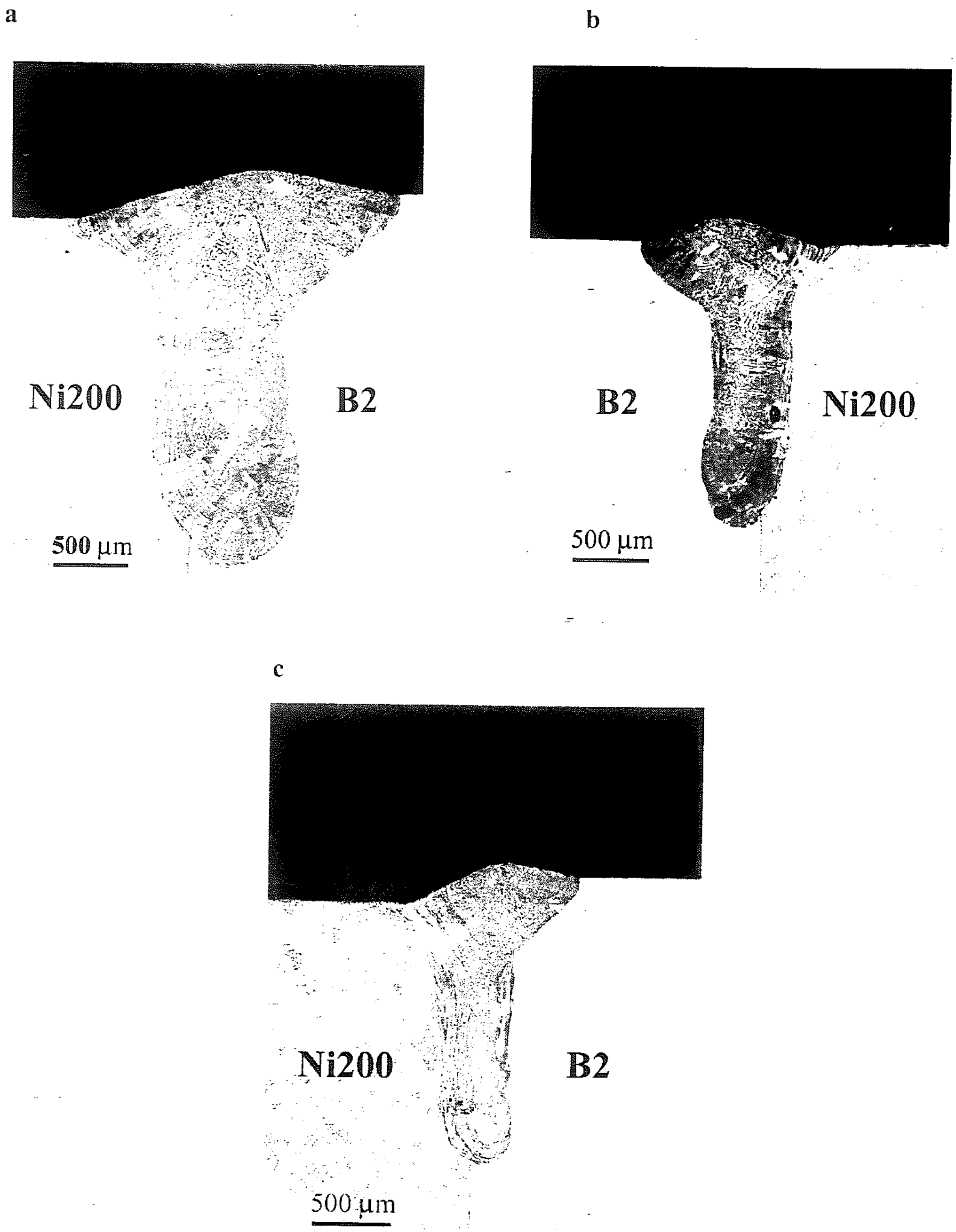

Figure 5.4 – B) Dissimilar metal welds showing dimensional changes with travel speed. a) 8/5 mm/s, b) 42.3 mm/s, c) 76.2 mm/s.

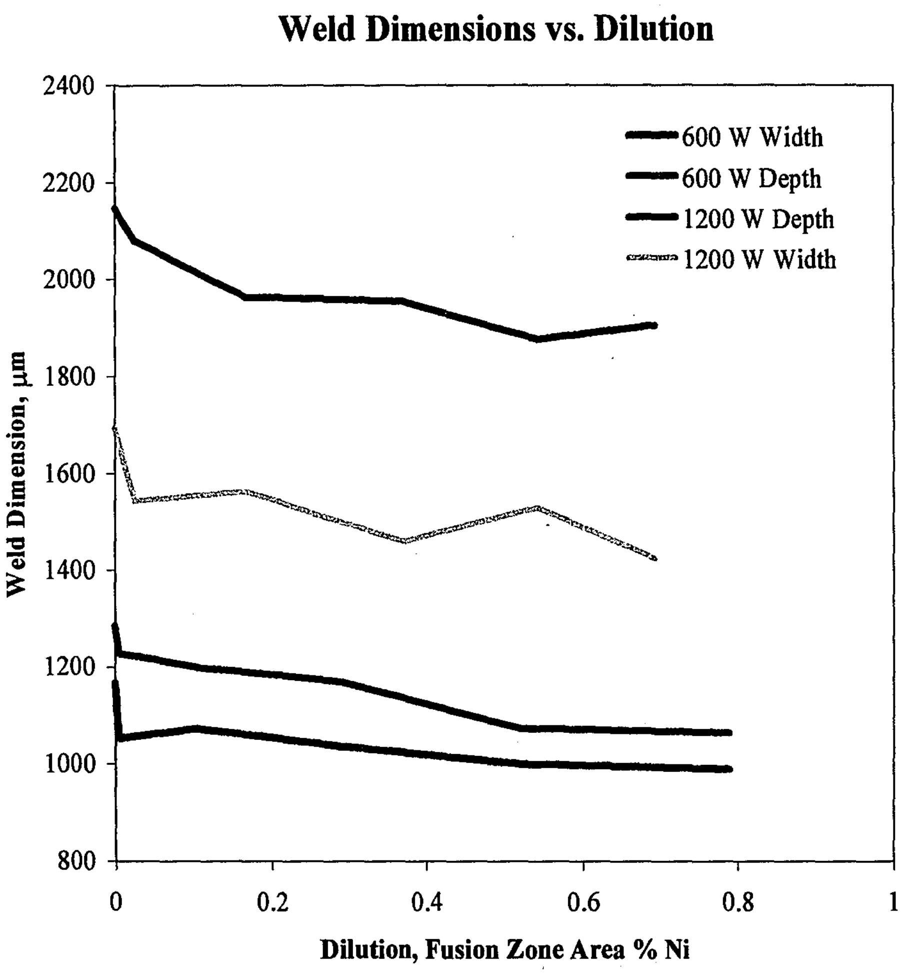

Figure 5.5 – Weld dilution vs. weld dimensions illustrating decrease in weld size as fusion zone area % Ni is increased.

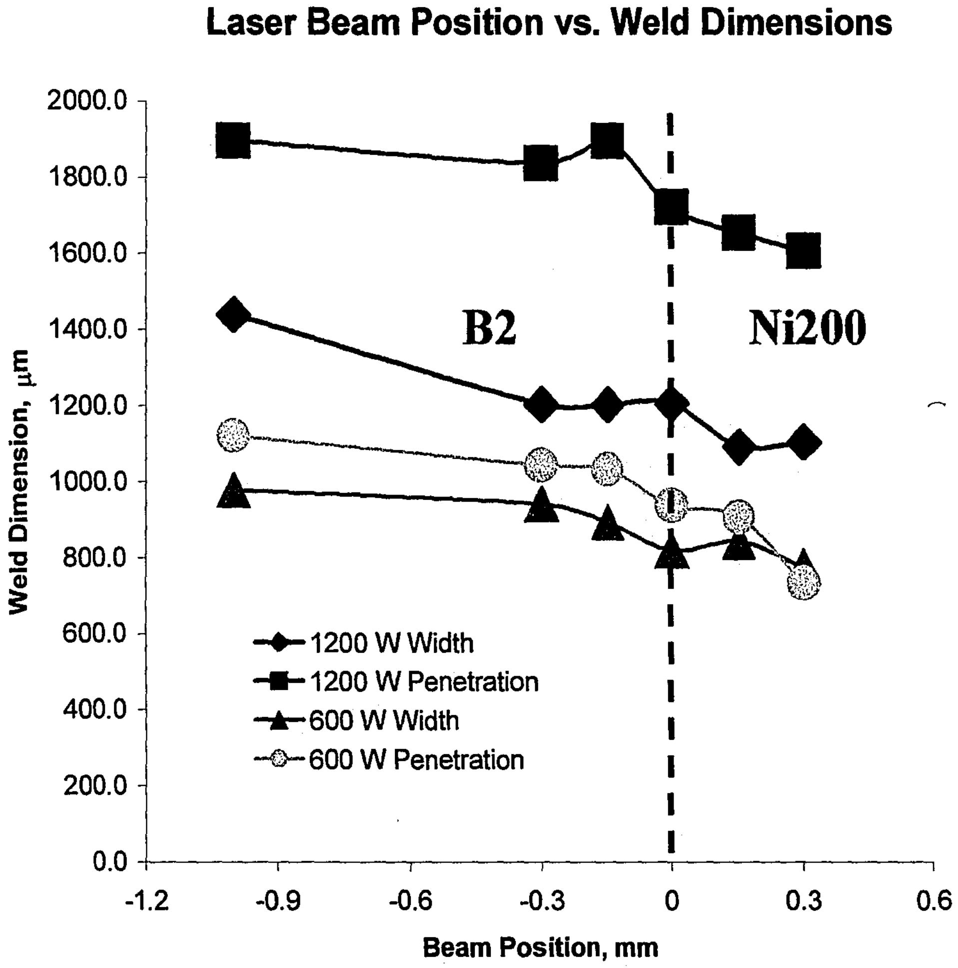

Figure 5.6 – A) Weld dimensions vs. beam position showing decrease in weld dimensions as beam is moved closer to Ni200 base metal. Negative beam position denotes beam located in Hastelloy B2 base metal.

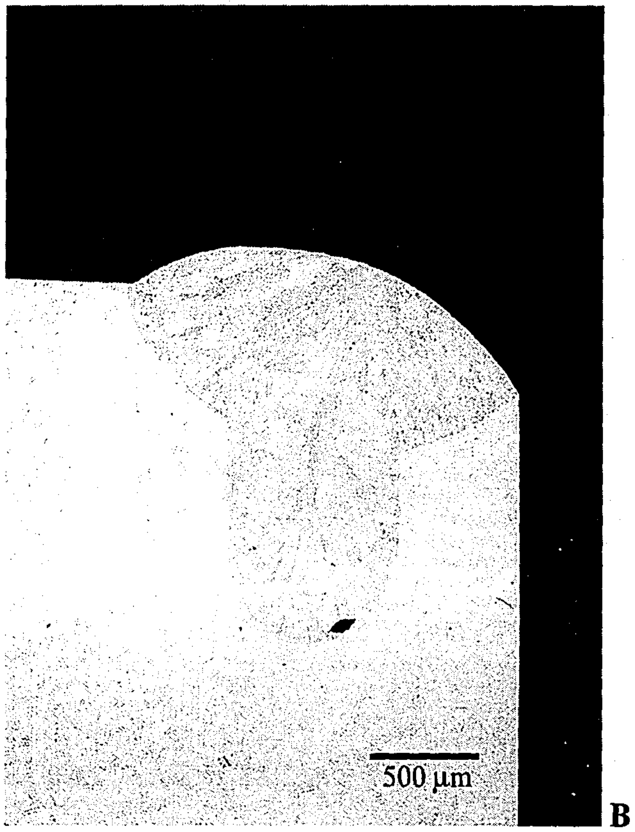

Figure 5.6 – B) Micrograph of dissimilar metal laser welds illustrated effect of changing beam position relative to base metal interface. 1 mm from materials interface (no Ni200 joined).

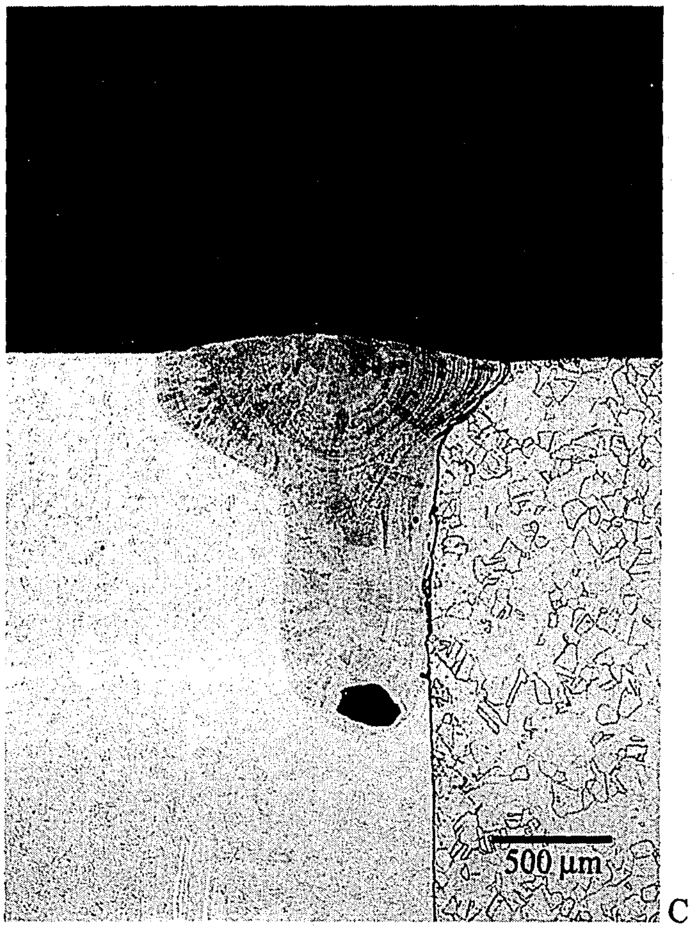

Figure 5.6 – C) Micrograph of dissimilar metal laser welds illustrated effect of changing beam position relative to base metal interface. 0.3 mm from materials interface, B2 is on left.

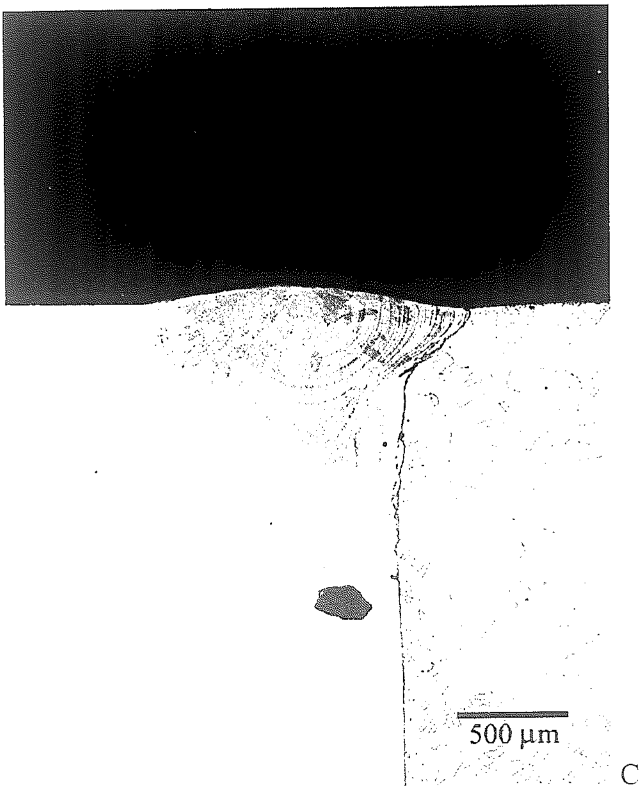

Figure 5.6 – C) Micrograph of dissimilar metal laser welds illustrated effect of changing beam position relative to base metal interface. 0.3 mm from materials interface, B2 is on left.

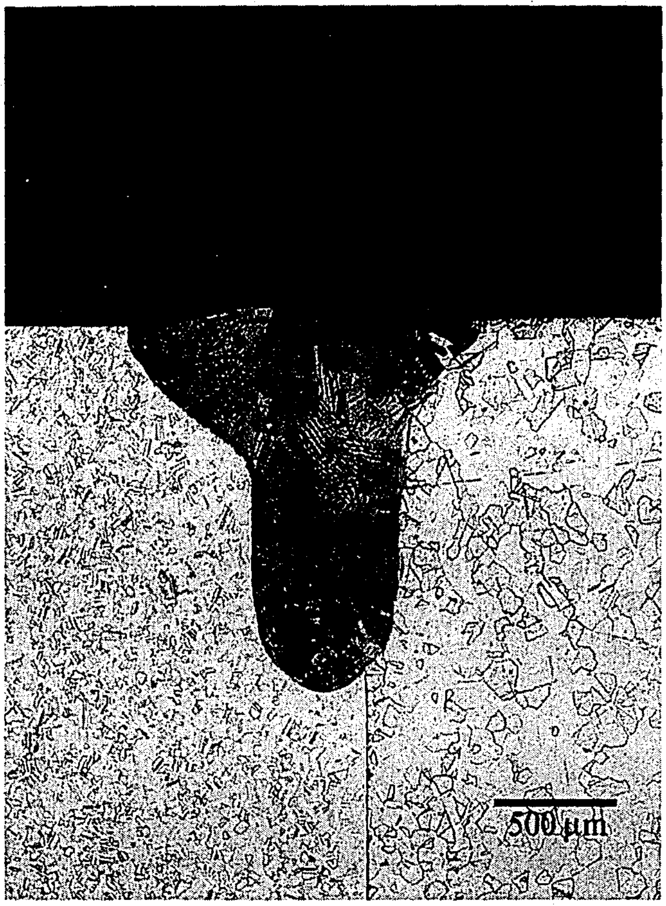

Figure 5.6 – D) Micrograph of dissimilar metal laser welds illustrated effect of changing beam position relative to base metal interface. 0.15 mm from materials interface, B2 is on the left.

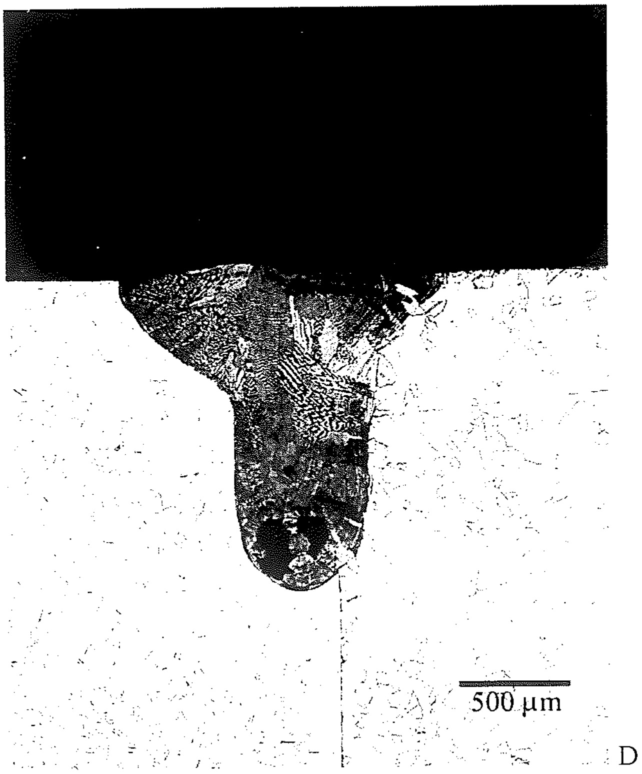

Figure 5.6 – D) Micrograph of dissimilar metal laser welds illustrated effect of changing beam position relative to base metal interface. 0.15 mm from materials interface, B2 is on the left.

Figure 5.6 – E) Micrograph of dissimilar metal laser welds illustrated effect of changing beam position relative to base metal interface. Laser at materials interface, B2 is on the left.

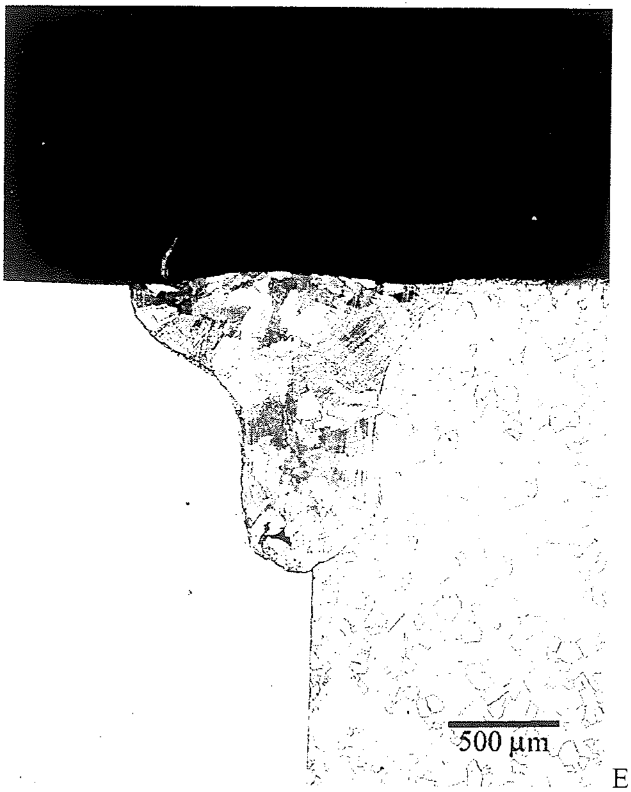

Figure 5.6 – E) Micrograph of dissimilar metal laser welds illustrated effect of changing beam position relative to base metal interface. Laser at materials interface, B2 is on the left.

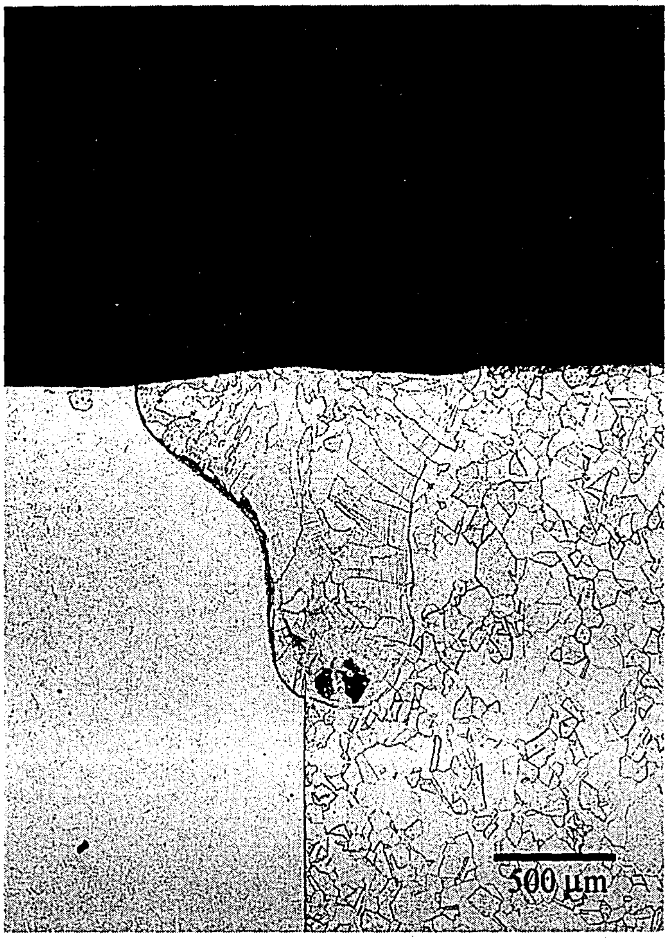

Figure 5.6 – F) Micrograph of dissimilar metal laser welds illustrated effect of changing beam position relative to base metal interface. –0.15 mm from materials interface, B2 on left.

Figure 5.6 – G) Micrograph of dissimilar metal laser welds illustrated effect of changing beam position relative to base metal interface. –0.3 mm from materials interface, B2 on the left.

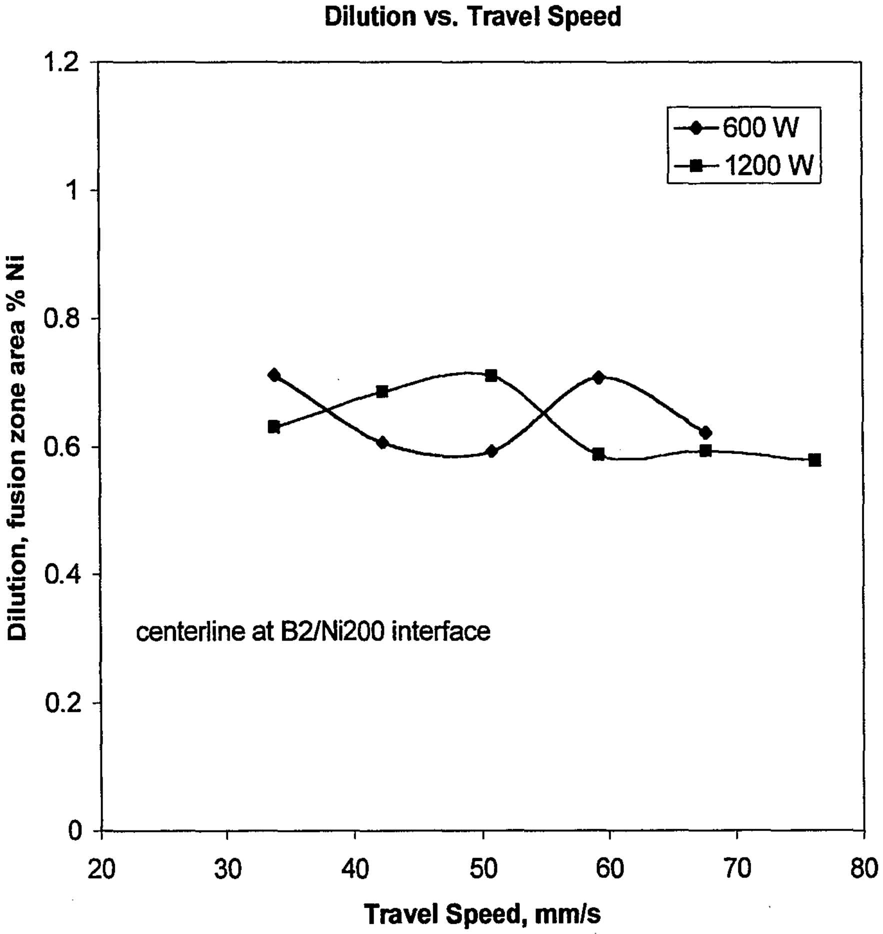

Figure 5.7 – Dilution vs. travel speed plot illustrating lack of trend as travel speed is increased.

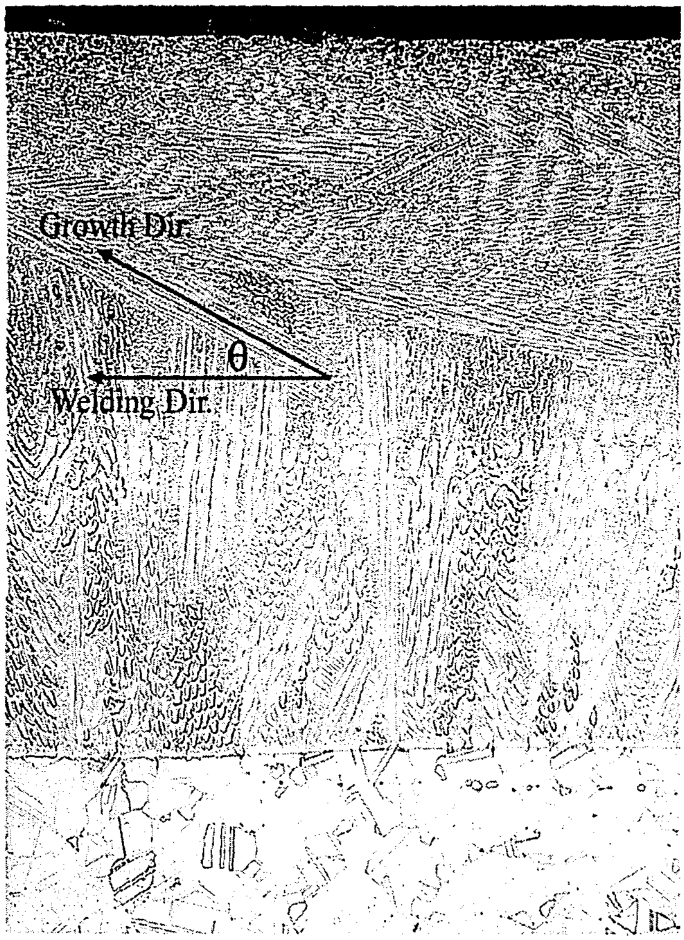

Figure 5.8 – Illustration of angle θ.

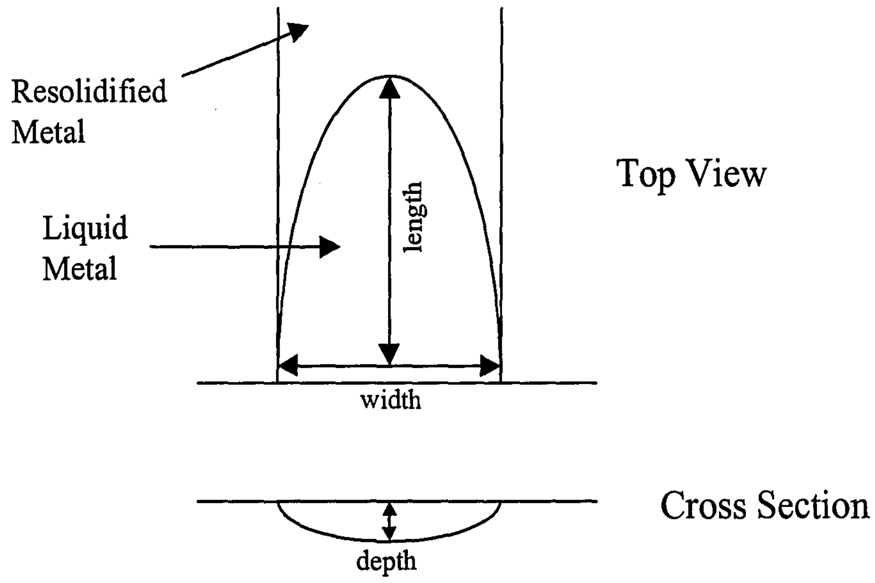

Figure 5.9A - Definition of weld pool shape dimensions.

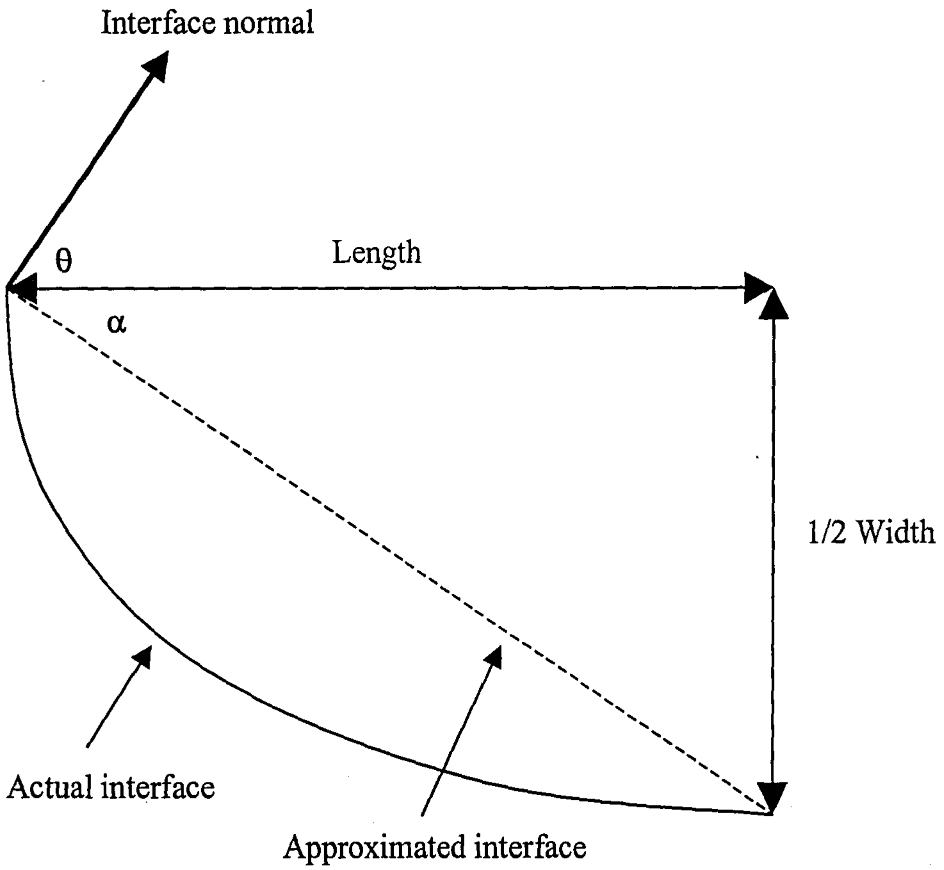

Figure 5.9B – Physical derivation of θ angle for hemispherical weld pool shape conditions.

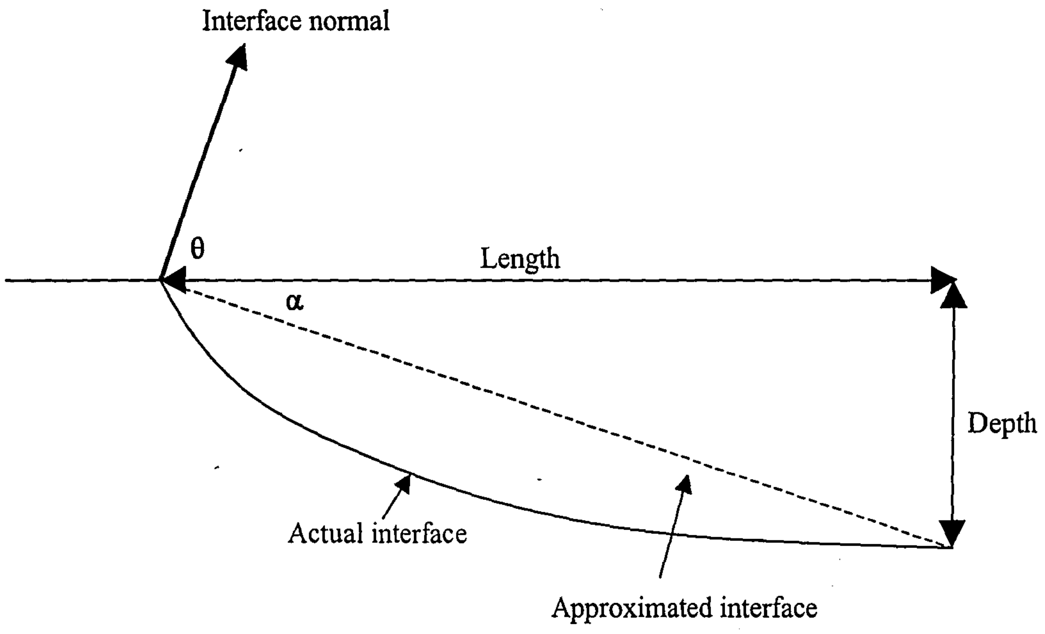

Figure 5.9C - Physical derivation of θ angle for teardrop weld pool shape conditions.

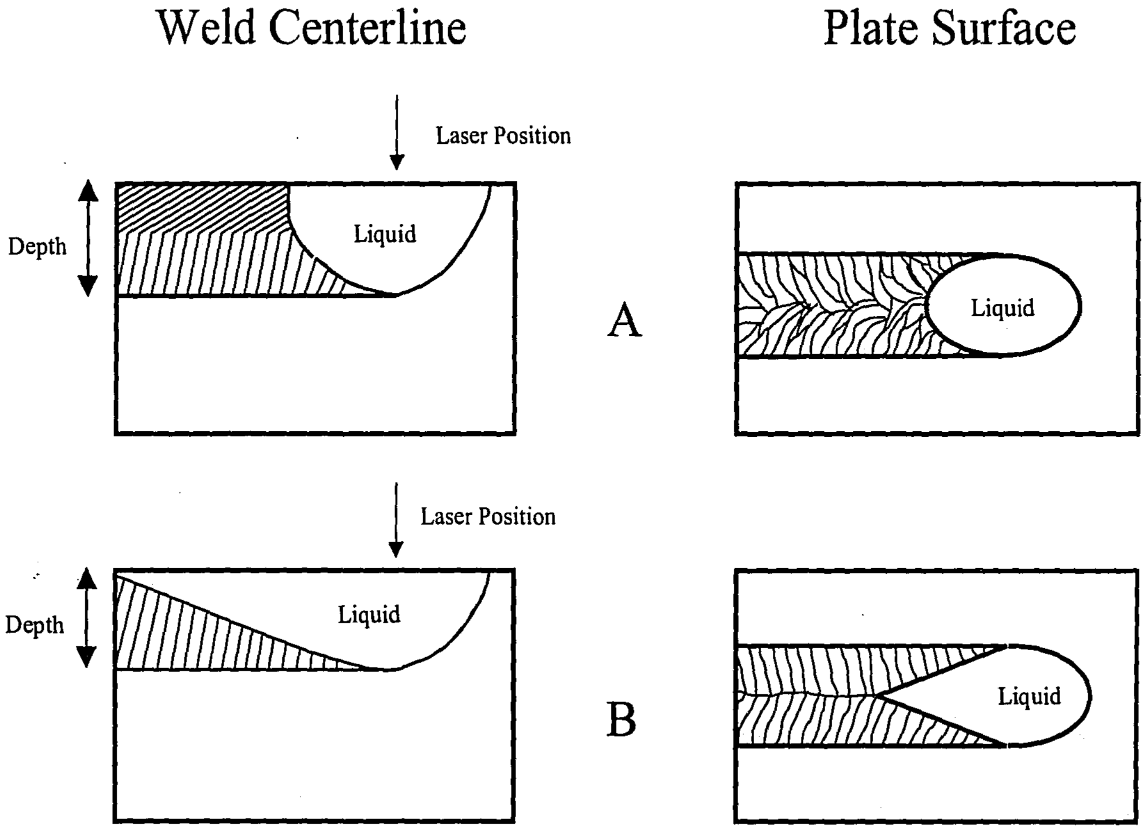

Figure 5.10 – Schematic of solidification sequence for A) hemispherical weld pool shape laser welds and B) tear drop shape weld pool laser welds.

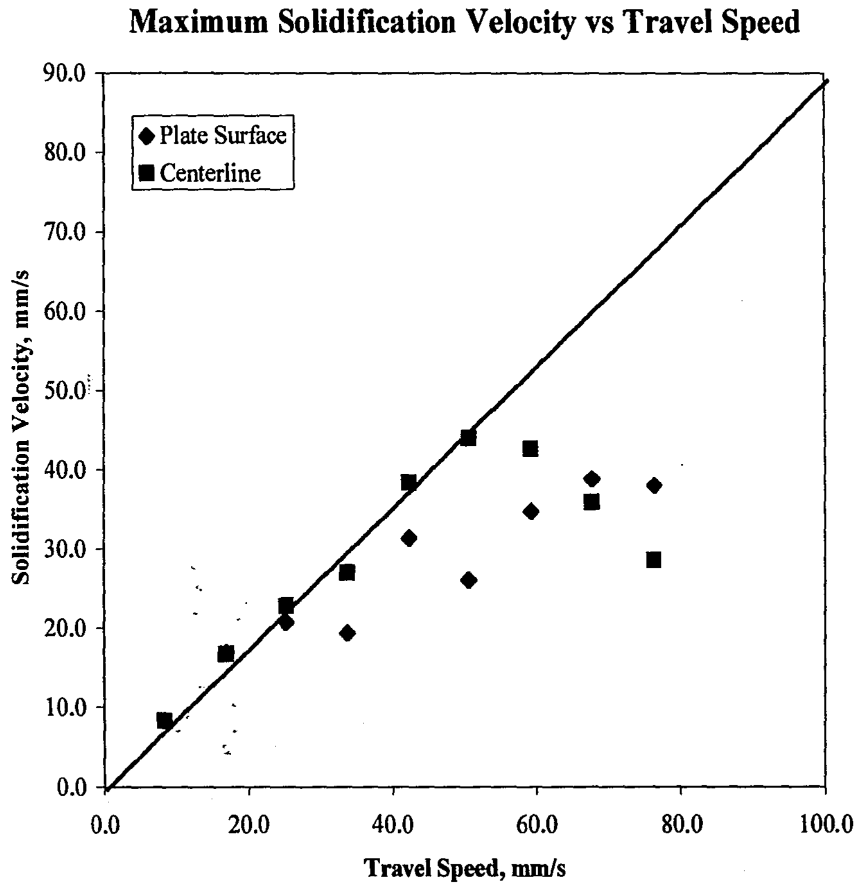

Figure 5.11A – Solidification velocity vs. travel speed for autogenous laser welds.

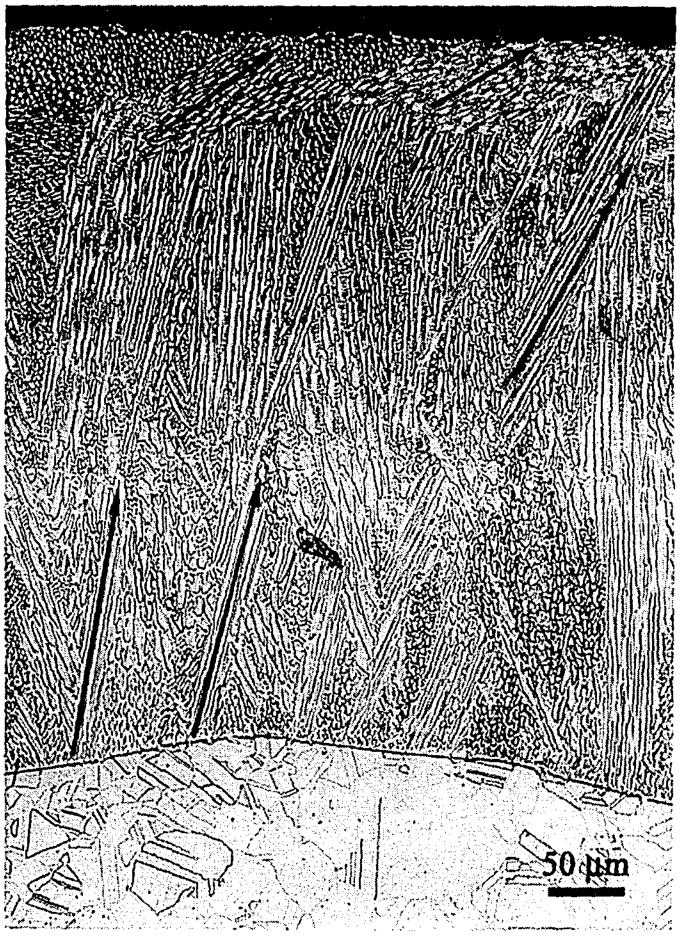

Figure 5.11B – Laser weld performed at 25.4 mm/s travel speed illustrating cell competitive growth. Welding direction is to the right.

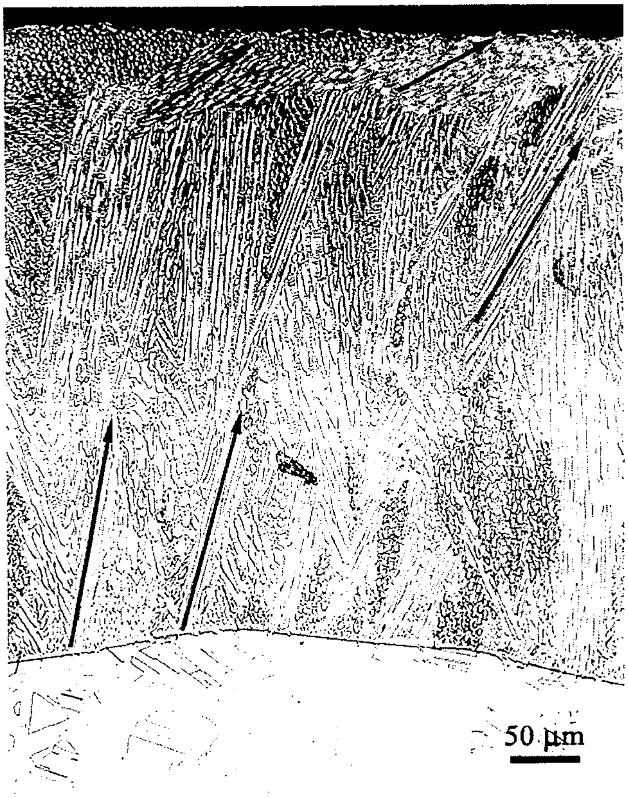

Figure 5.11B – Laser weld performed at 25.4 mm/s travel speed illustrating cell competitive growth. Welding direction is to the right.

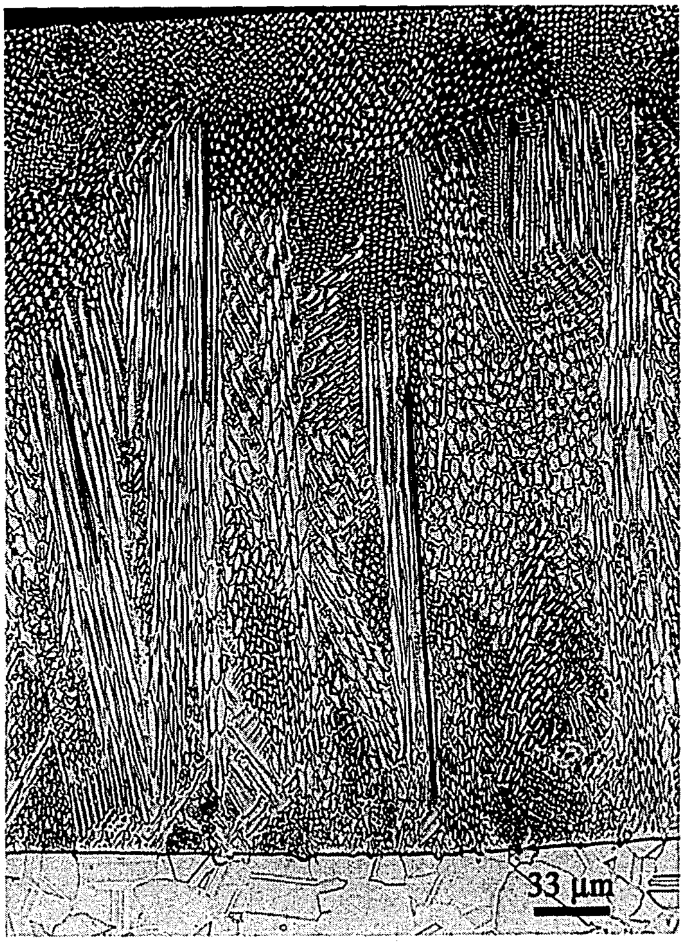

Figure 5.11C - Laser weld performed at 50.8 mm/s travel speed illustrating no cell reorientation. Welding direction is to the right.

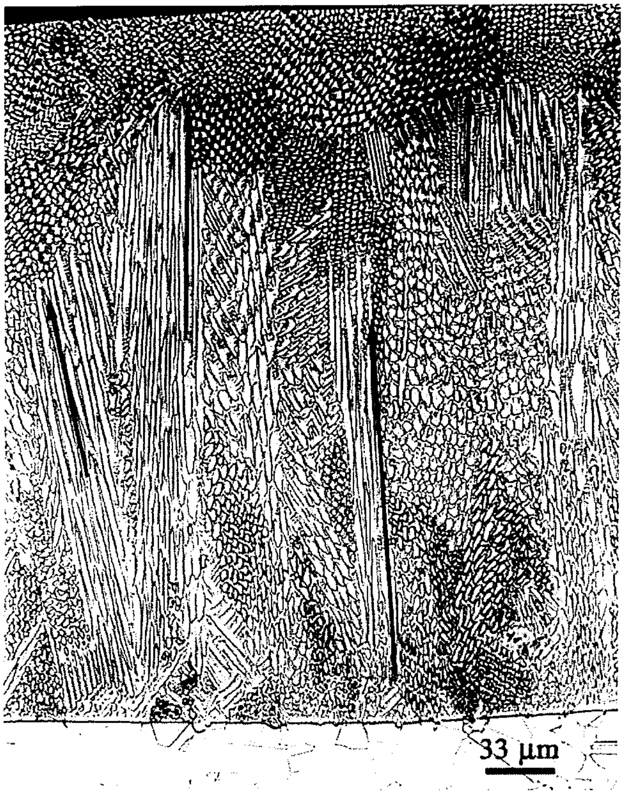

Figure 5.11C - Laser weld performed at 50.8 mm/s travel speed illustrating no cell reorientation. Welding direction is to the right.

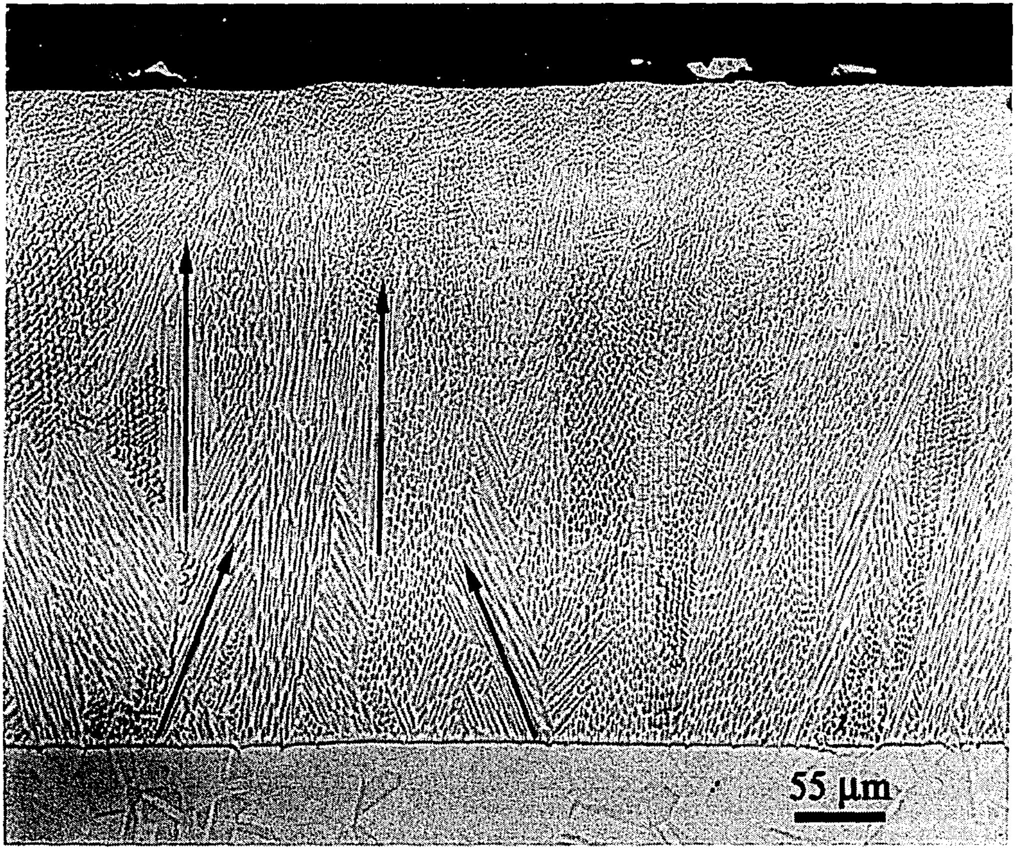

Figure 5.11D - Laser weld performed at 76.2 mm/s travel speed illustrating no cell reorientation. Welding direction is to the right.

Figure 5.12A – Plate surface view of 10 mm/s travel speed GTA weld.

Figure 5.12B - Plate surface view of 40 mm/s travel speed GTA weld.

Figure 5.12C - Plate surface view of 75 mm/s travel speed GTA weld.

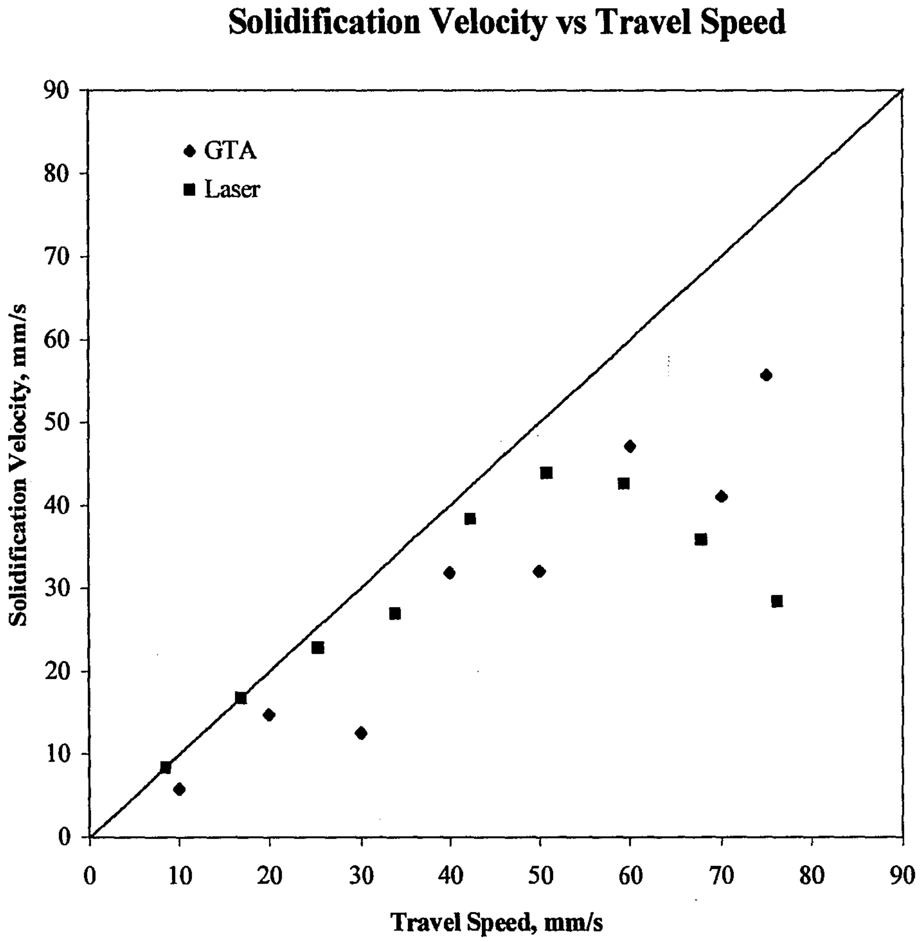

Figure 5.13 – Comparison of solidification velocities for GTA and laser welds.

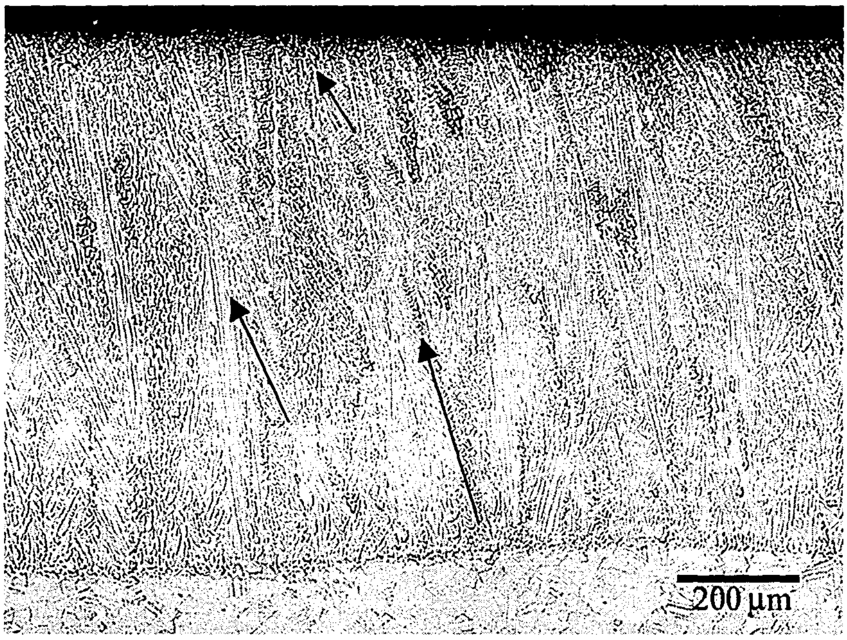

Figure 5.14A - GTA weld performed at 10 mm/s travel speed illustrating no cell reorientation. Welding direction is to the left.

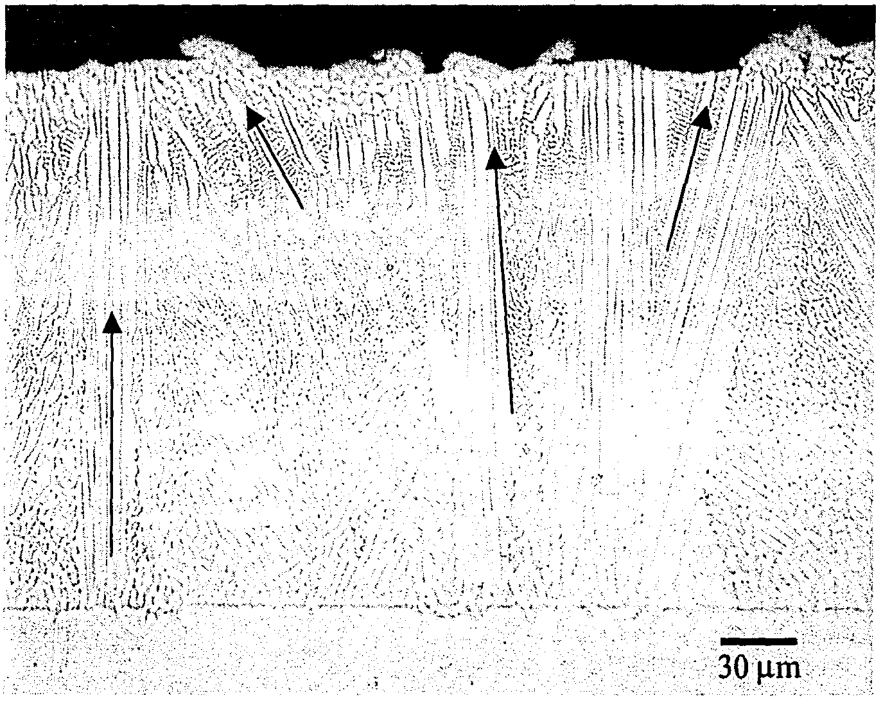

Figure 5.14B - GTA weld performed at 75.0 mm/s travel speed illustrating no cell reorientation. Welding direction is to the left.

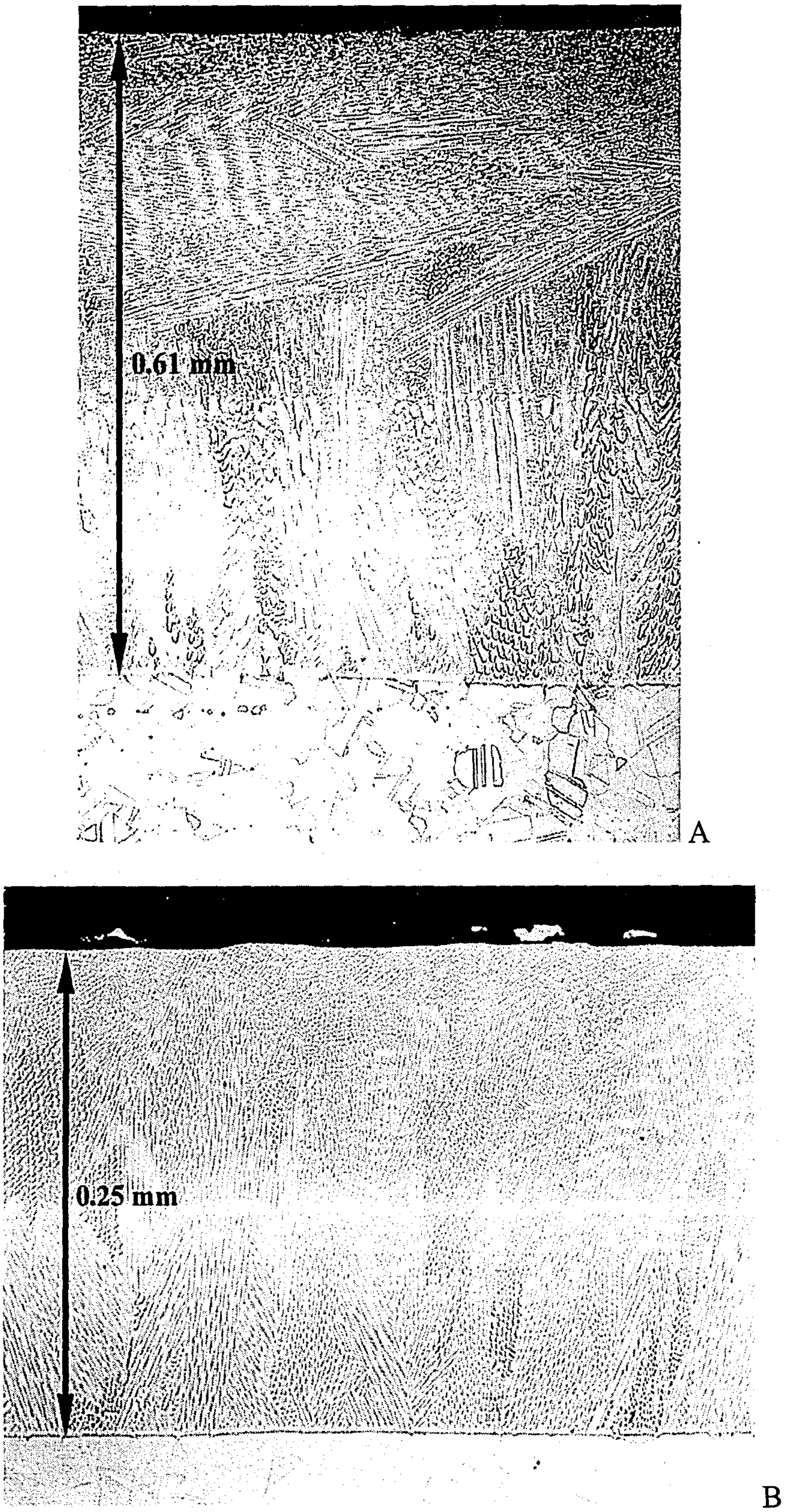

Figure 5.15 – A) Slow (8.5 mm/s) travel speed laser weld showing grain reorientation, B) fast travel speed (76.2 mm/s) laser weld showing no reorientation.

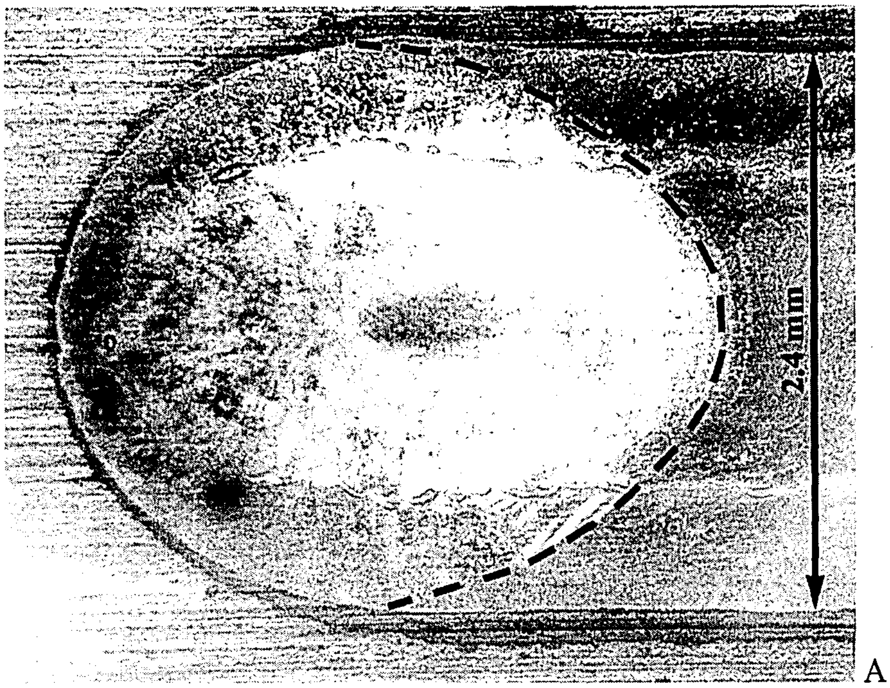

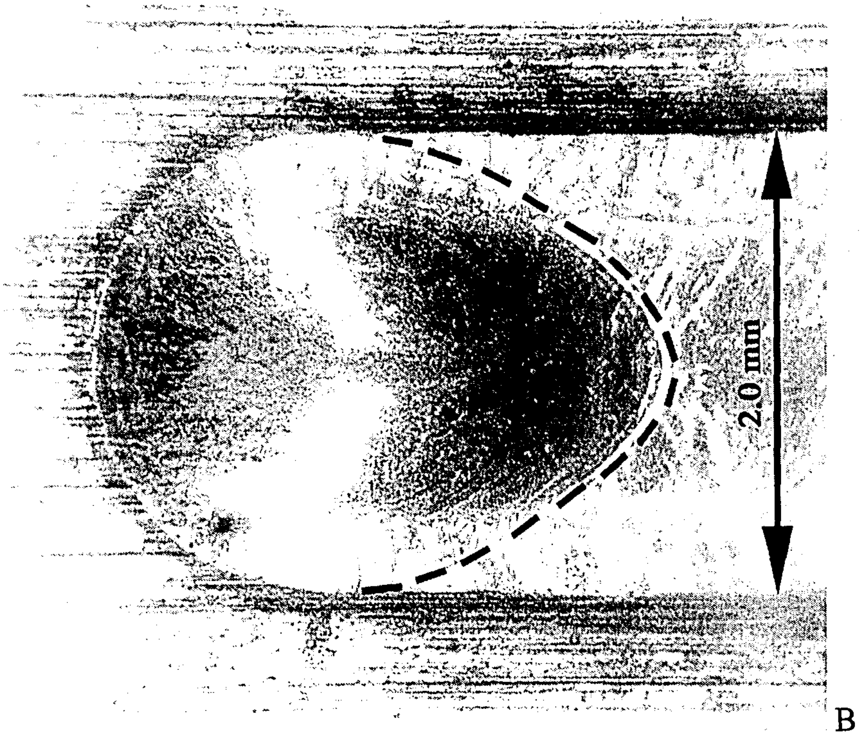

Figure 5.16 – A) Weld pool shape for 8.5 mm/s travel speed laser weld illustrating hemispherical shape. B) Weld pool shape for 16.9 mm/s travel speed laser weld illustrating hemispherical shaped trailing edge.

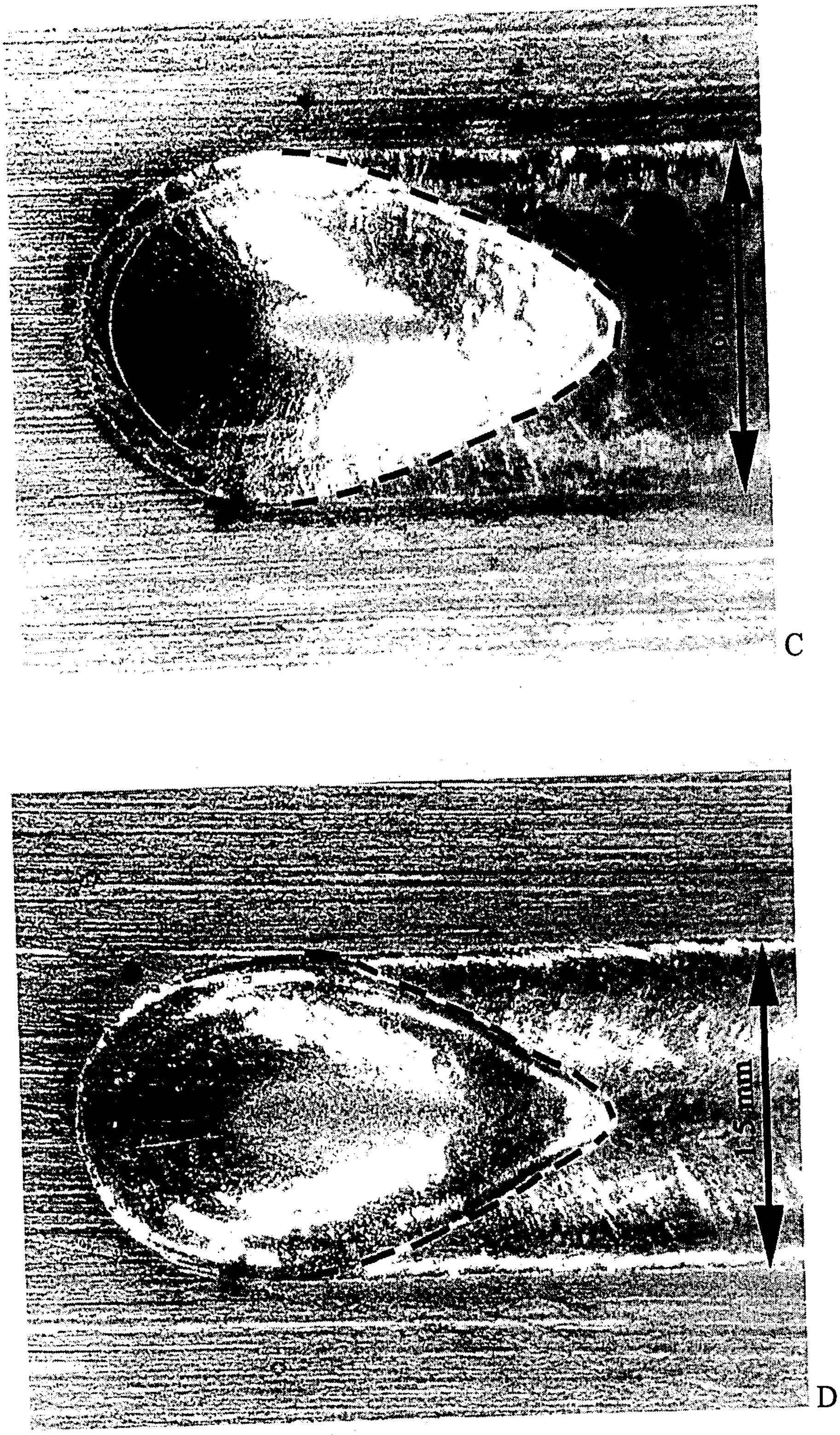

Figure 5.16 – C) Weld pool shape for 33.8 mm/s travel speed laser weld illustrating transitional weld pool shape. D) Weld pool shape for 42.3 mm/s travel speed laser weld illustrating teardrop shaped weld pool.

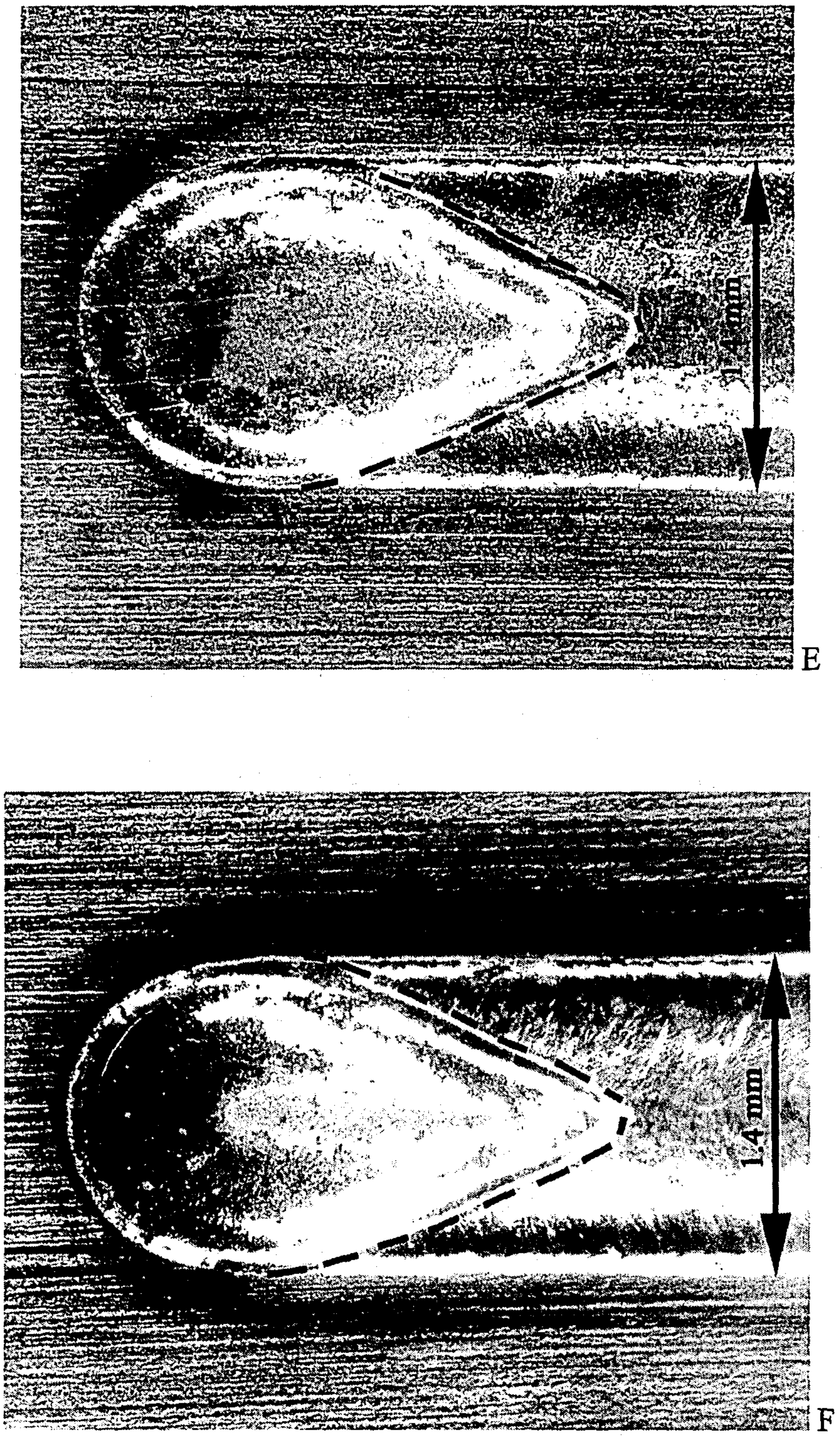

Figure 5.16 – E) Weld pool shape for 50.8 mm/s travel speed laser weld illustrating tear drop weld pool shape. F) Weld pool shape for 59.3 mm/s travel speed laser weld illustrating teardrop shaped weld pool.

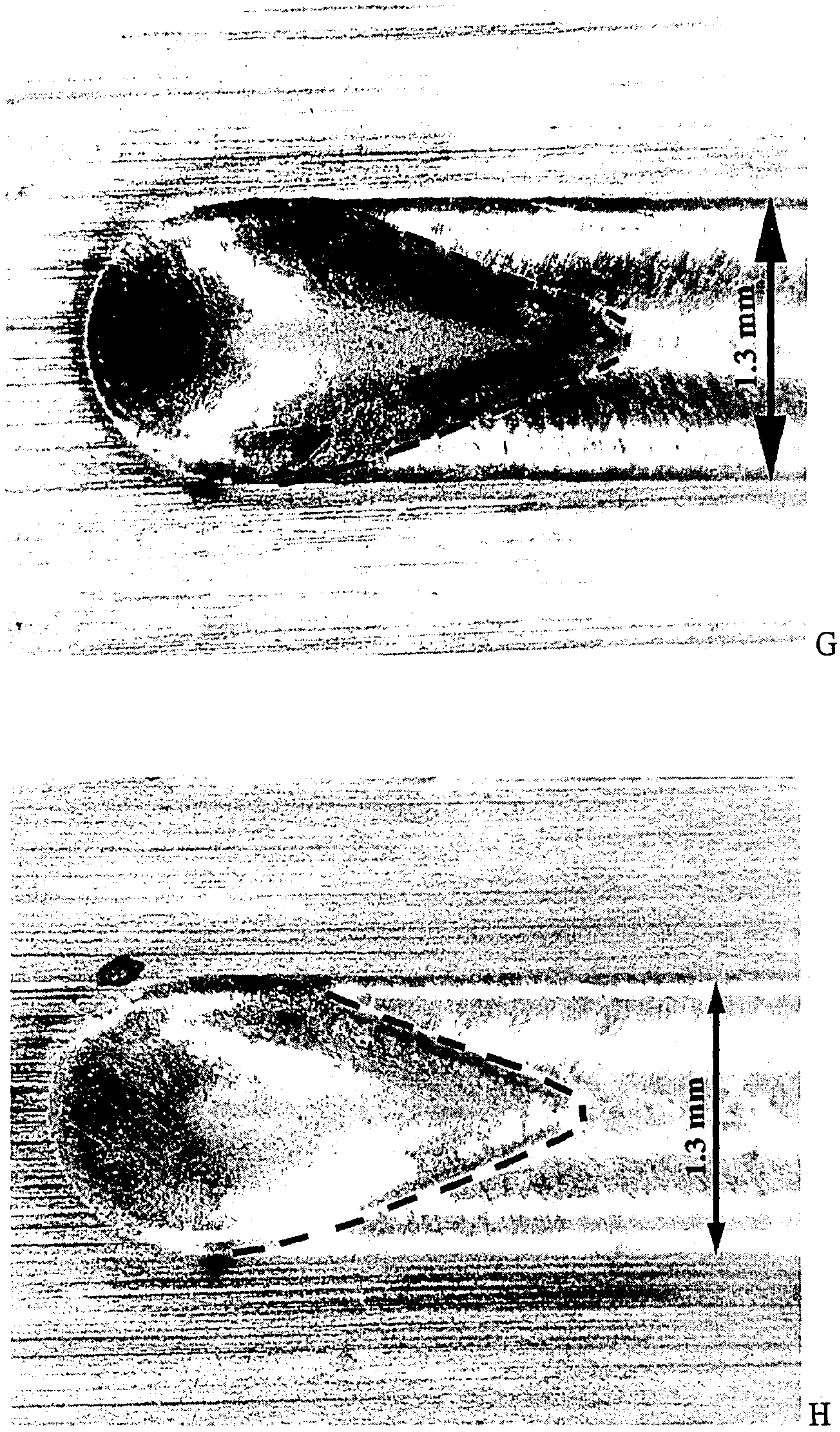

Figure 5.16 – G) Weld pool shape for 67.7 mm/s travel speed laser weld illustrating tear drop weld pool shape. H) Weld pool shape for 76.2 mm/s travel speed laser weld illustrating teardrop shaped weld pool.

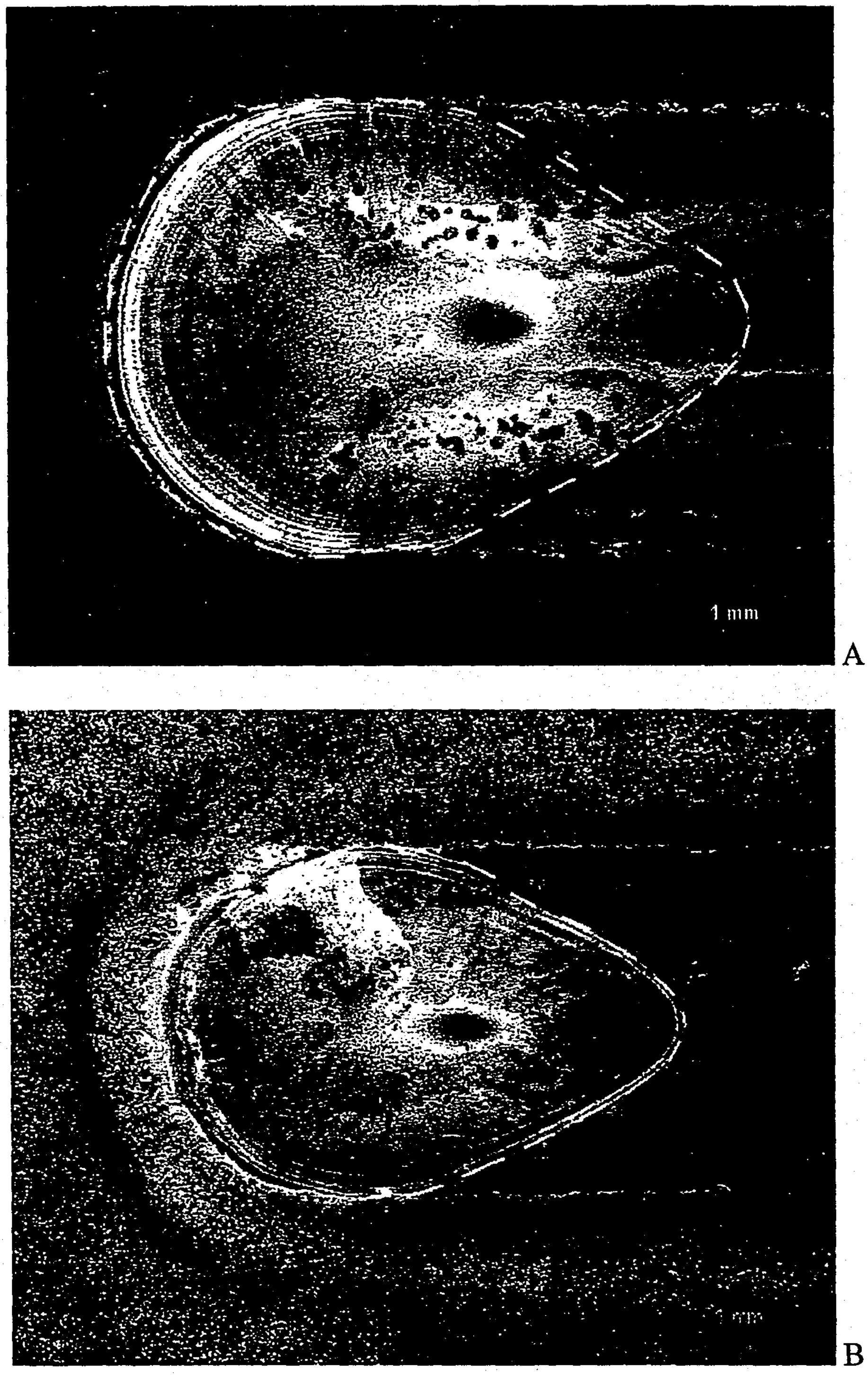

Figure 5.17 - A) Weld pool shape for 5 mm/s travel speed GTA weld illustrating teardrop weld pool shape. B) Weld pool shape for 10 mm/s travel speed GTA weld illustrating tear drop weld pool shape.

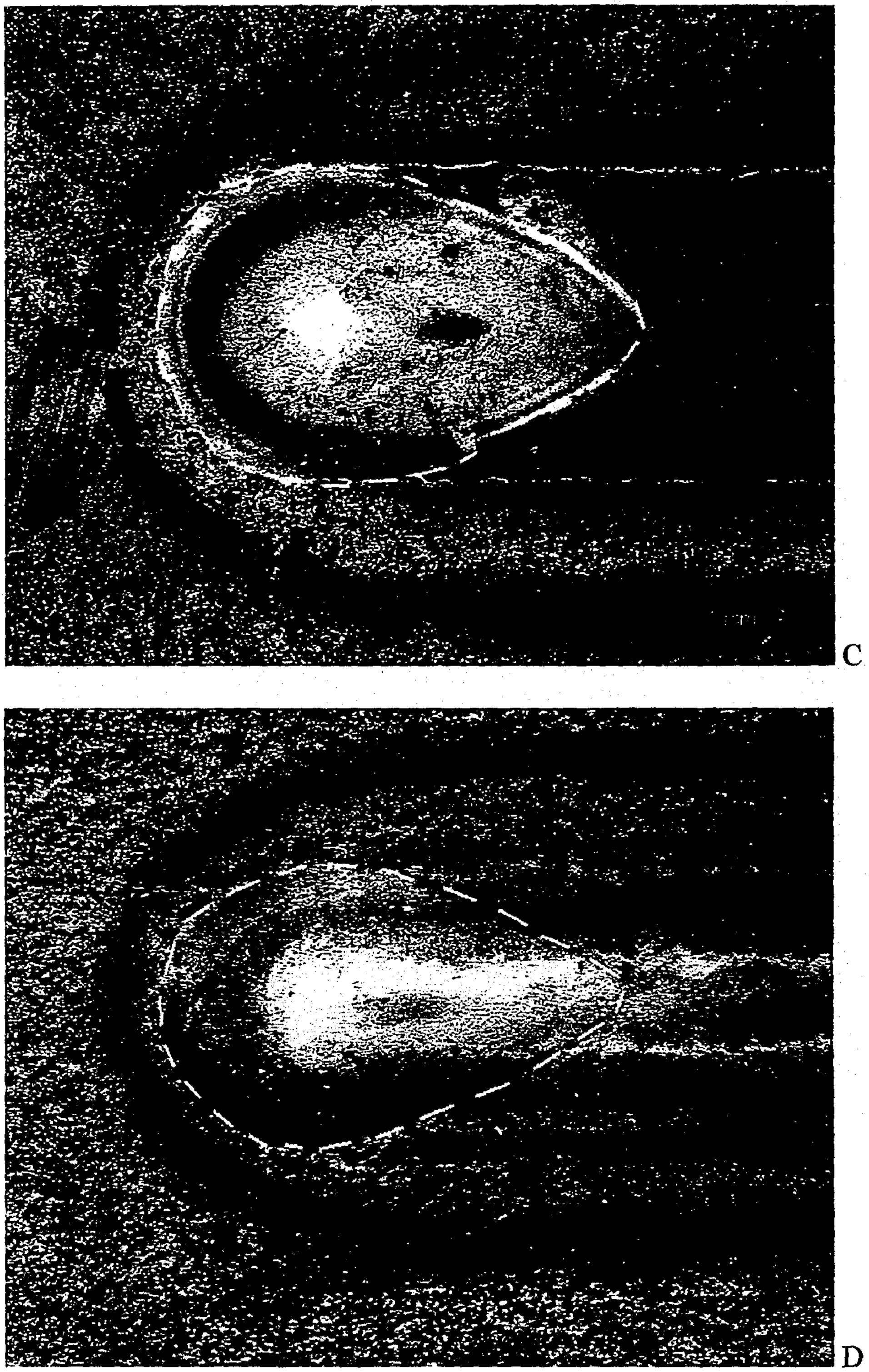

Figure 5.17 - C) Weld pool shape for 15 mm/s travel speed GTA weld illustrating teardrop weld pool shape. D) Weld pool shape for 20 mm/s travel speed GTA weld illustrating tear drop weld pool shape.

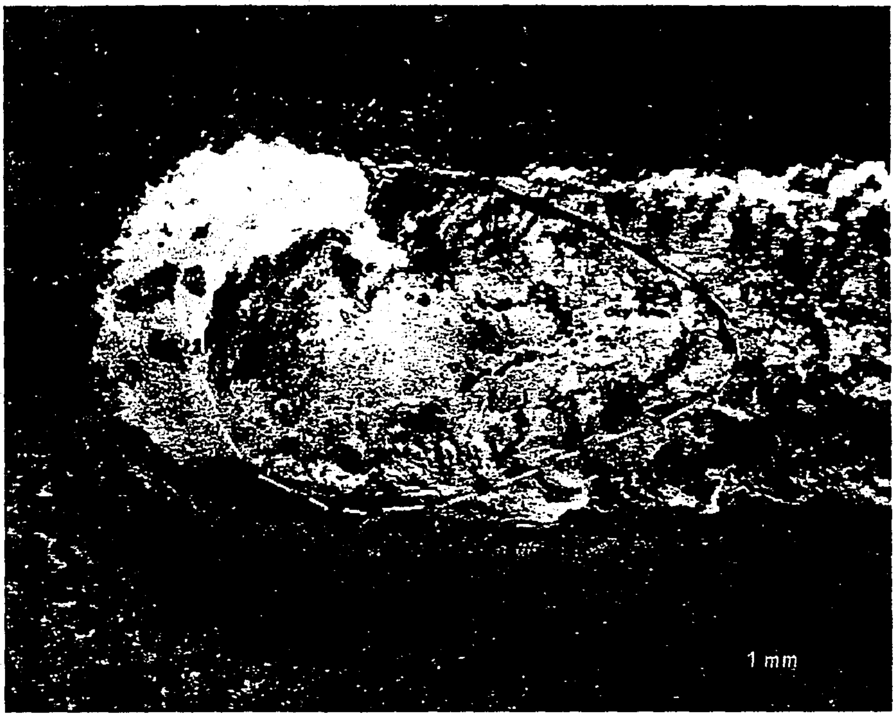

E

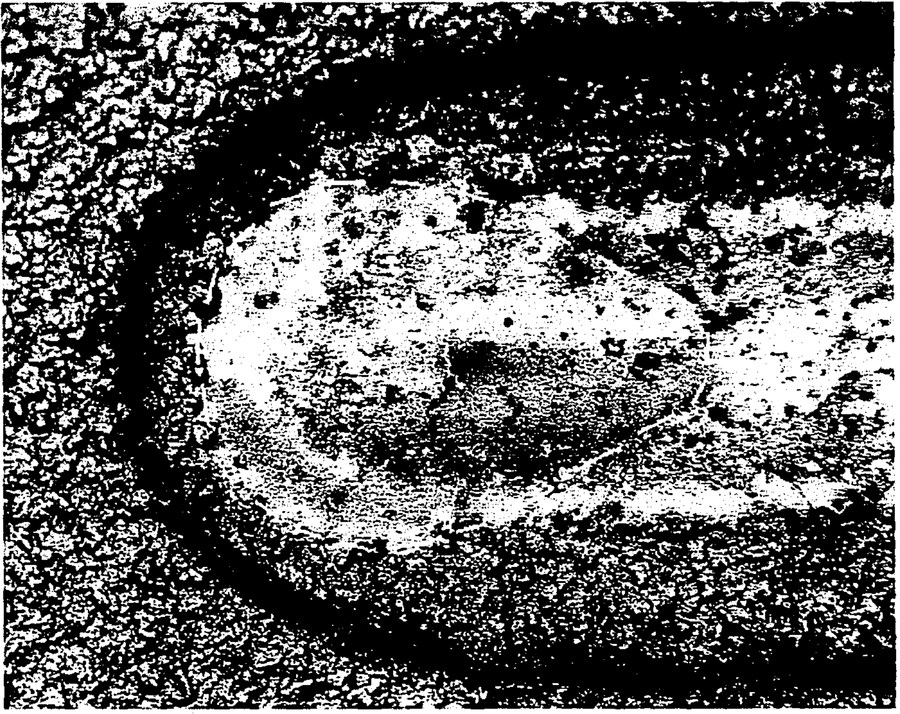

F

Figure 5.17 - E) Weld pool shape for 25 mm/s travel speed GTA weld illustrating teardrop weld pool shape. F) Weld pool shape for 30 mm/s travel speed GTA weld illustrating tear drop weld pool shape.

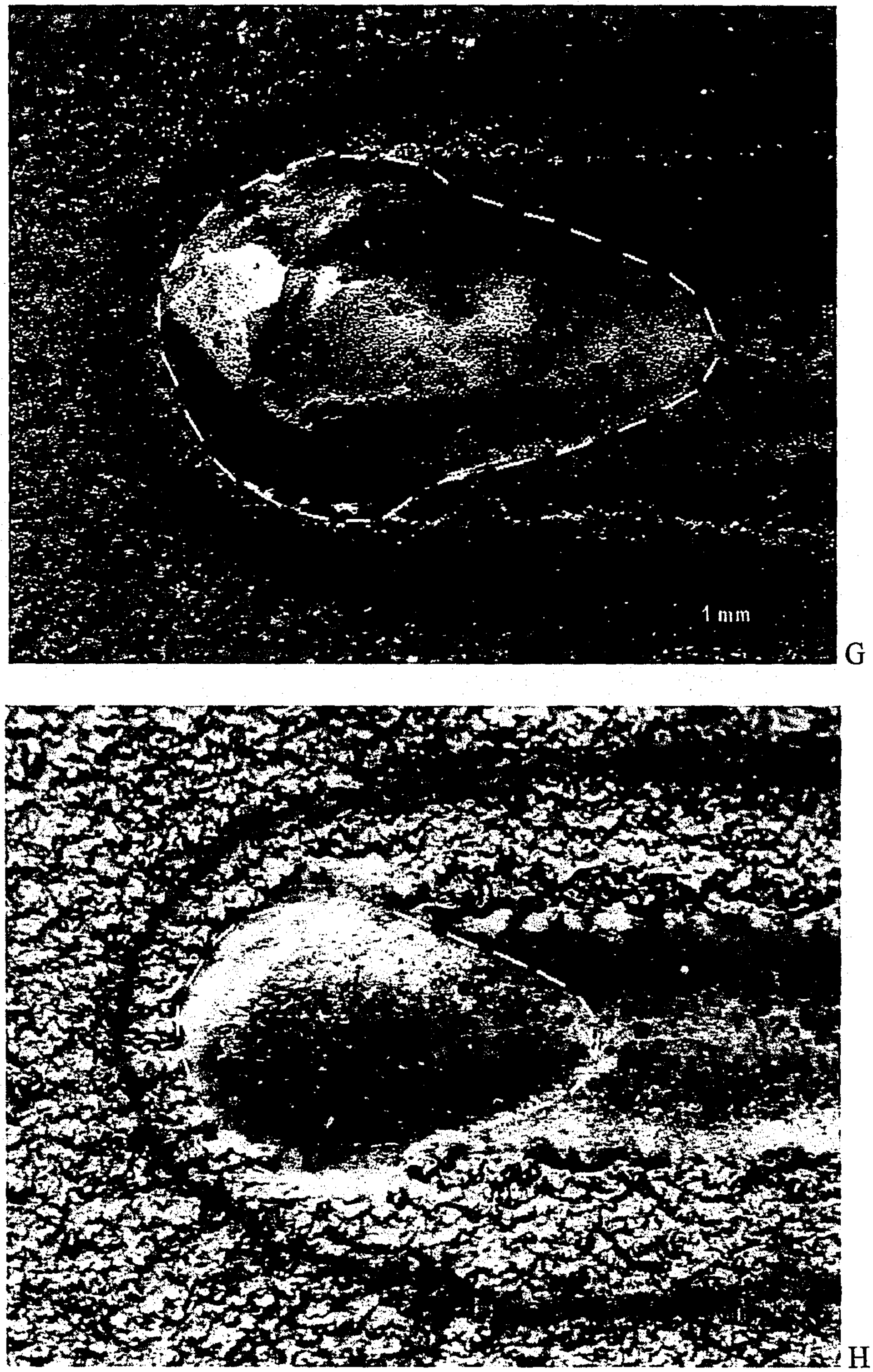

Figure 5.17 - G) Weld pool shape for 35 mm/s travel speed GTA weld illustrating teardrop weld pool shape. H) Weld pool shape for 40 mm/s travel speed GTA weld illustrating tear drop weld pool shape.

I

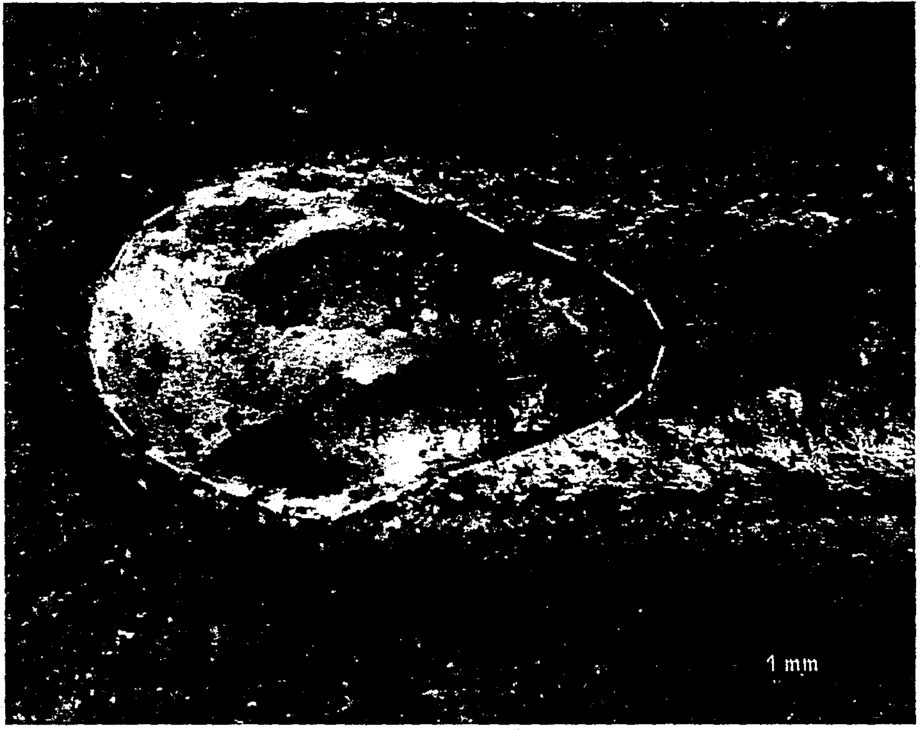

J

Figure 5.17 - I) Weld pool shape for 45 mm/s travel speed GTA weld illustrating teardrop weld pool shape. J) Weld pool shape for 50 mm/s travel speed GTA weld illustrating tear drop weld pool shape.

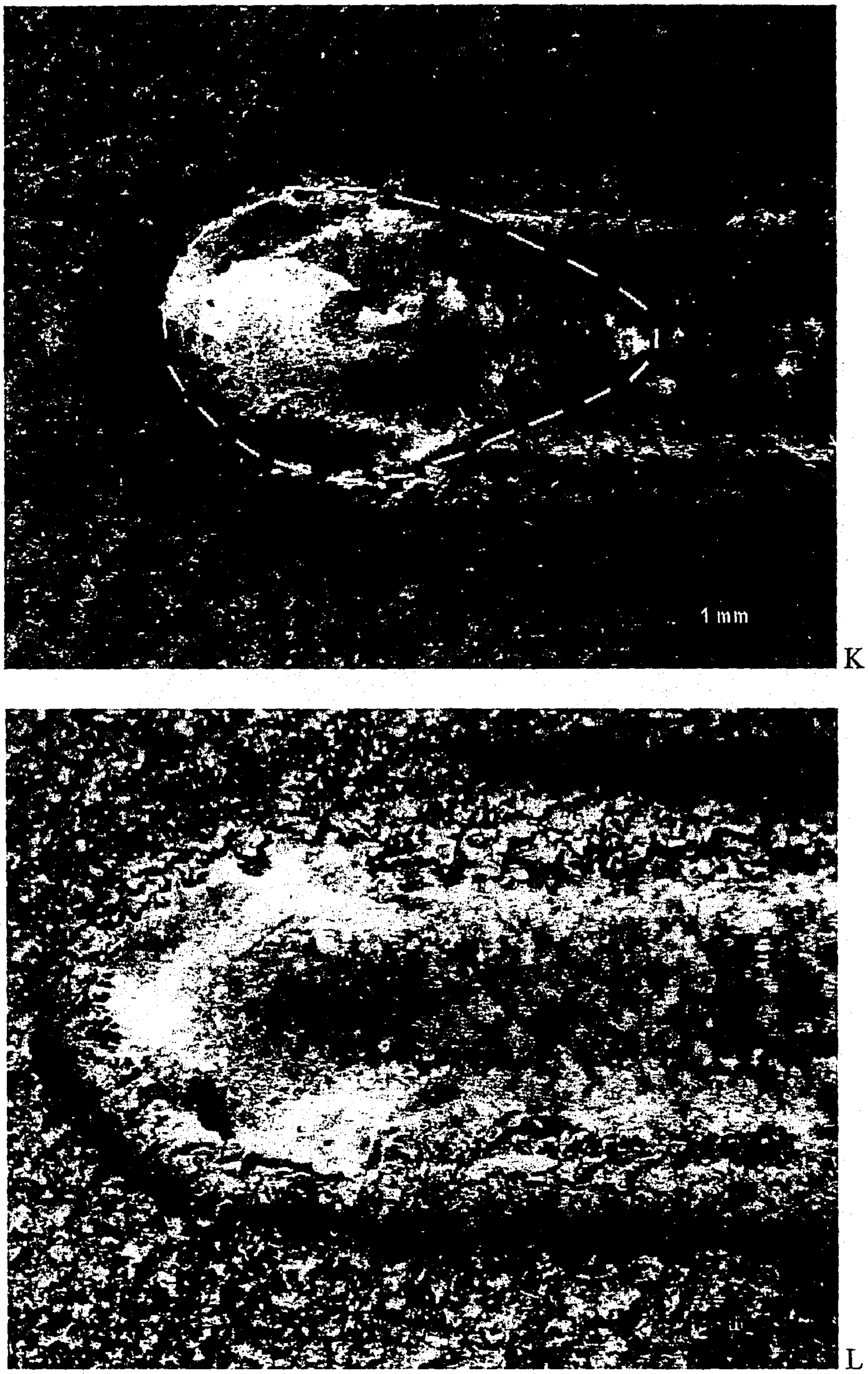

Figure 5.17 - K) Weld pool shape for 55 mm/s travel speed GTA weld illustrating teardrop weld pool shape. L) Weld pool shape for 60 mm/s travel speed GTA weld illustrating tear drop weld pool shape.

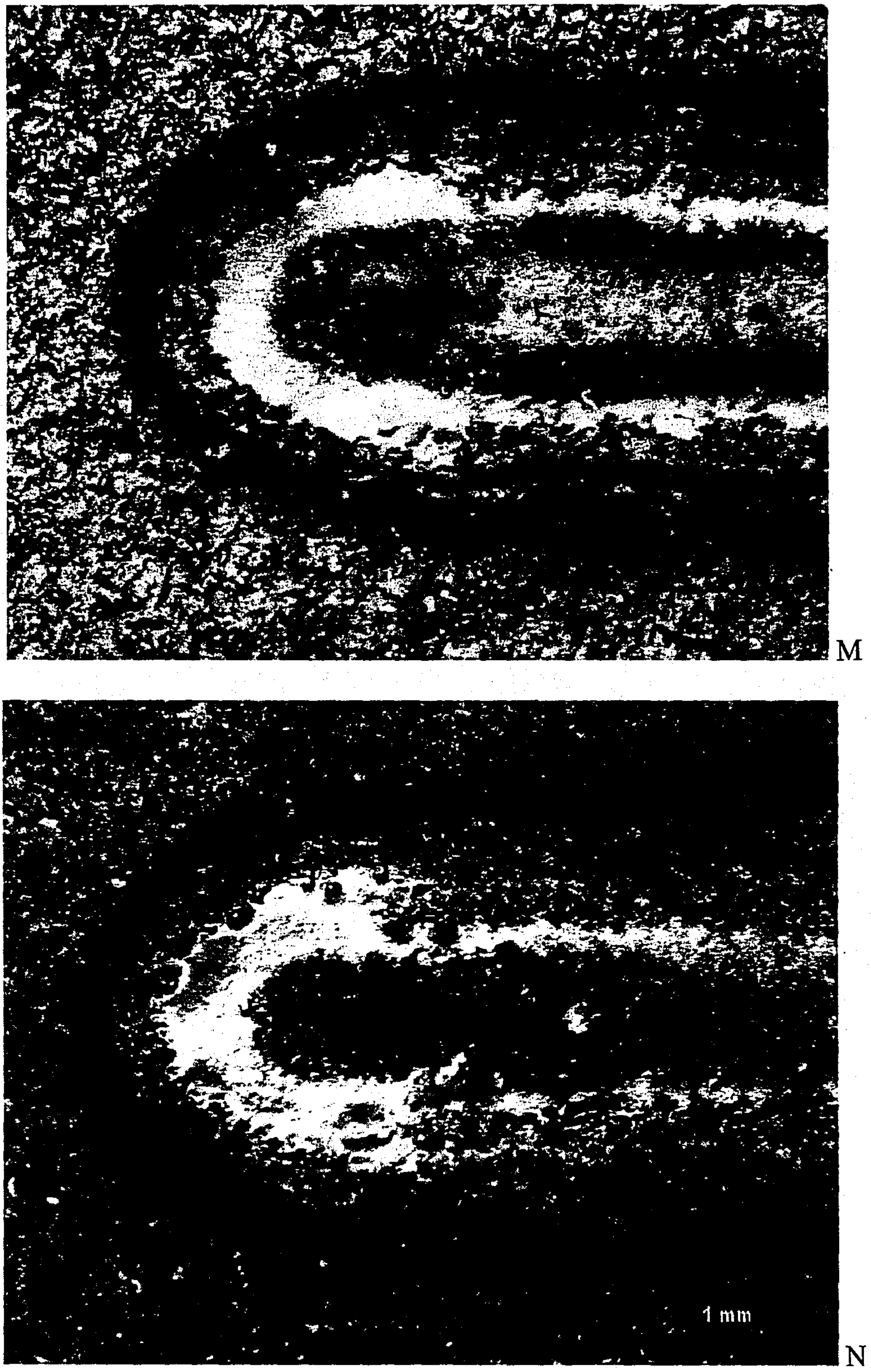

Figure 5.17 - M) Weld pool shape for 65 mm/s travel speed GTA weld illustrating inability to determine weld pool shape. N) Weld pool shape for 70 mm/s travel speed GTA weld illustrating inability to determine weld pool shape.

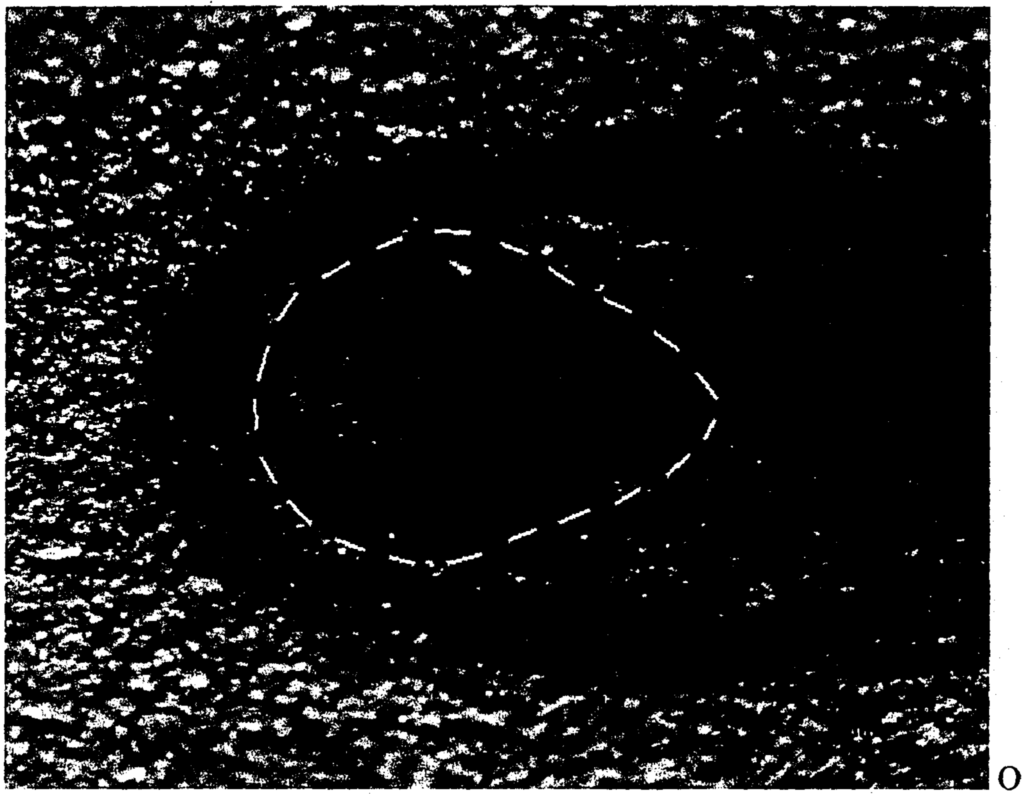

Figure 5.17 - O) Weld pool shape for 75 mm/s travel speed GTA weld illustrating teardrop weld pool shape.

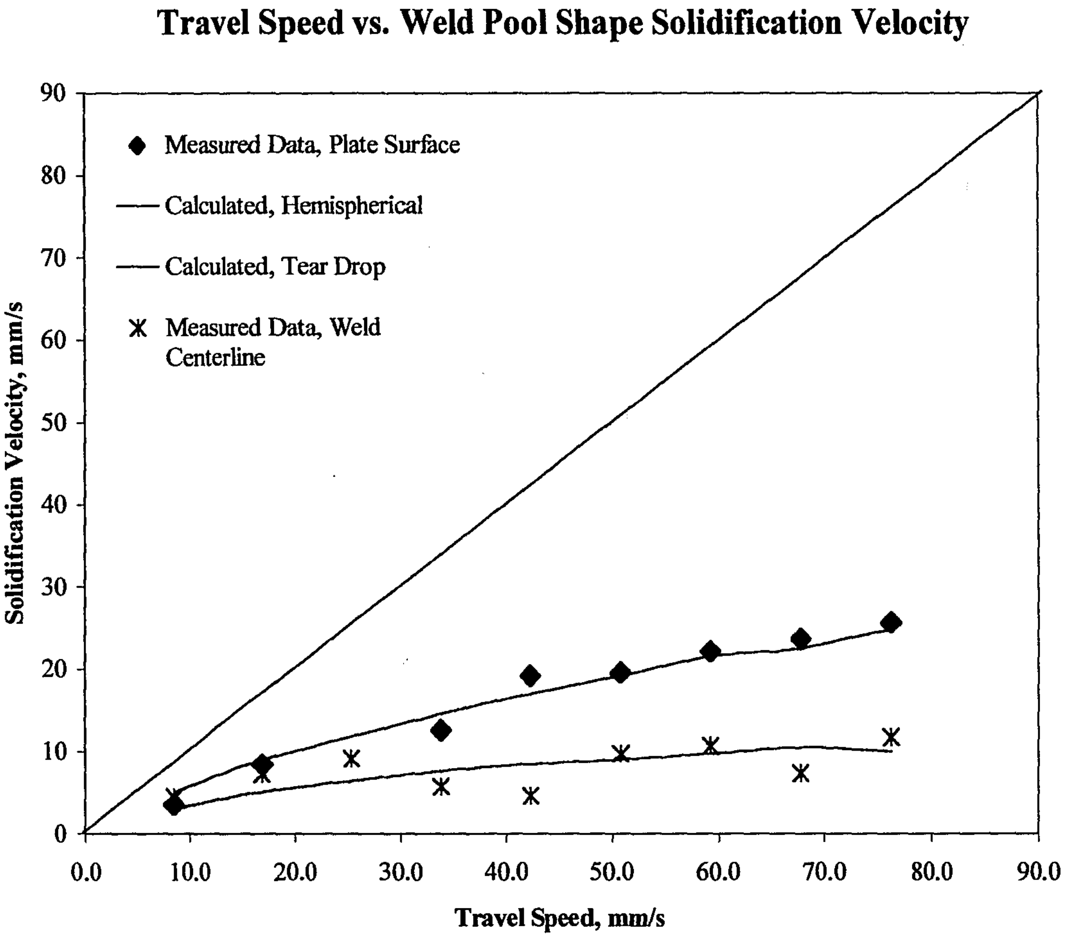

Figure 5.18 – Average solidification velocity versus travel speed for autogenous laser welds.

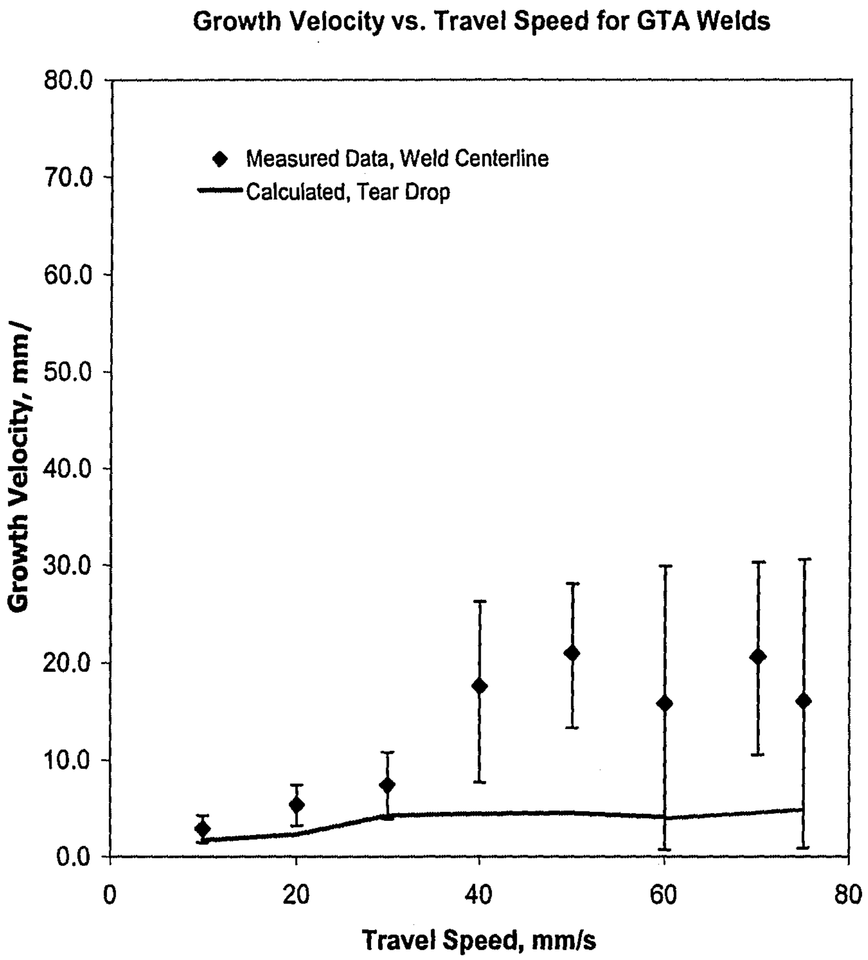

Figure 5.19 - Average solidification velocity versus travel speed for autogenous GTA welds.

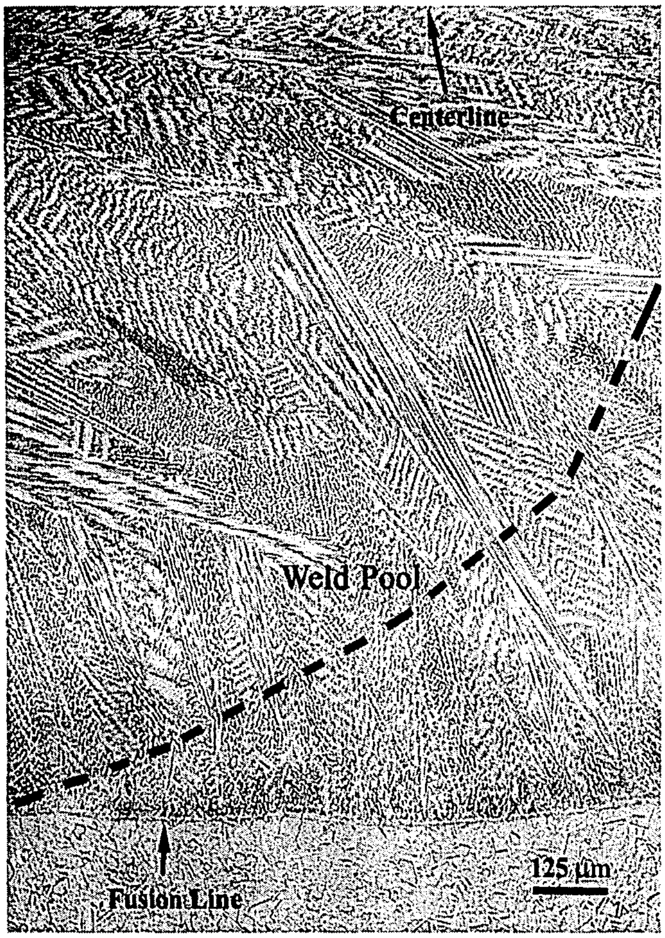

Figure 5.20A – Plate surface view of slow speed (8.5 mm/s travel speed) autogenous laser weld showing dominant cell growth from the sides and shape of weld pool. Welding direction is to the left.

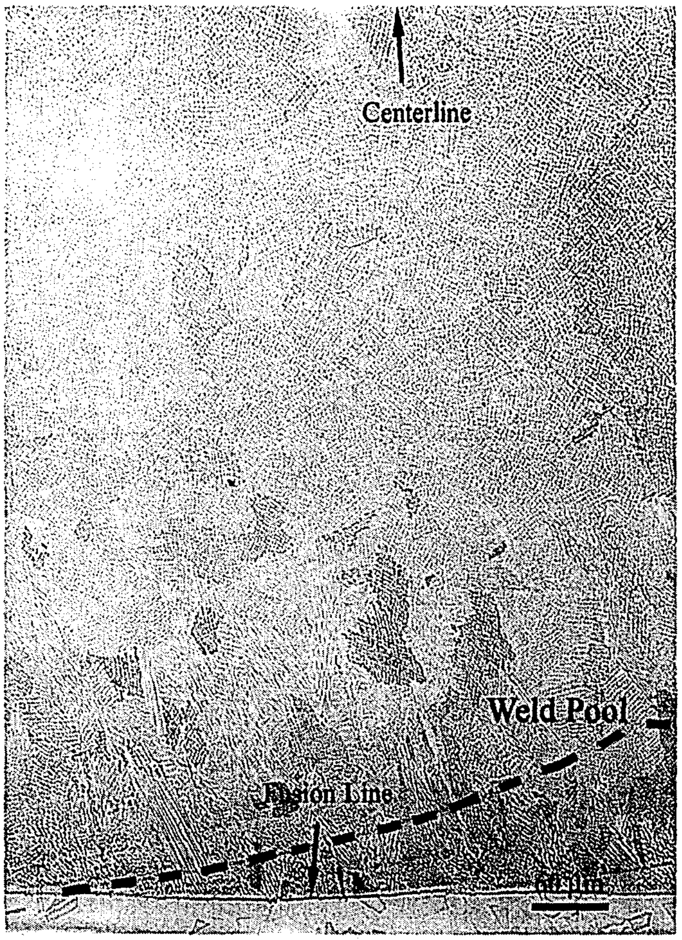

Figure 5.20B – Plate surface view of high speed (59.3 mm/s travel speed) autogenous laser weld showing dominant cell growth from the bottom and weld pool shape. Welding direction is to the left.

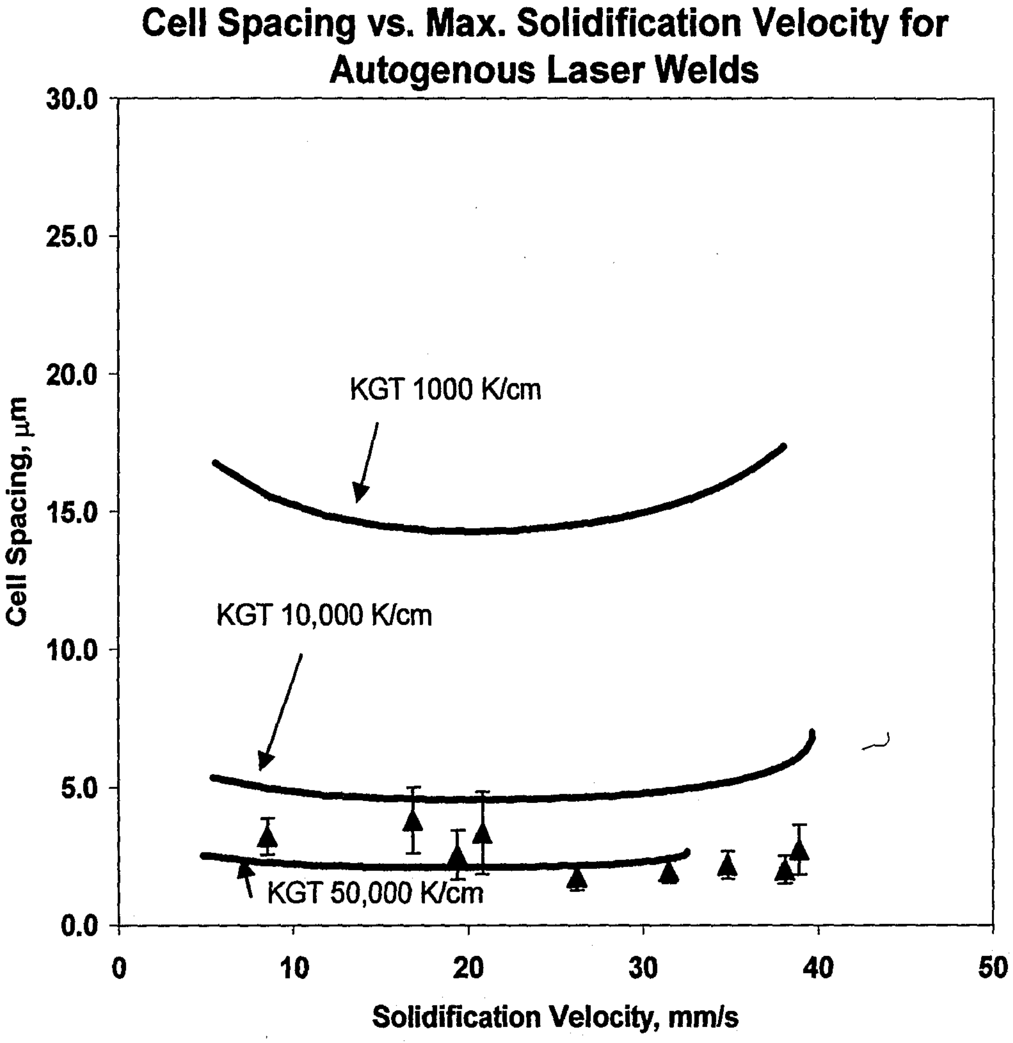

Figure 5.21 – Cell spacing vs. laser weld solidification velocity for both experimentally measured data and KGT model predicted data.

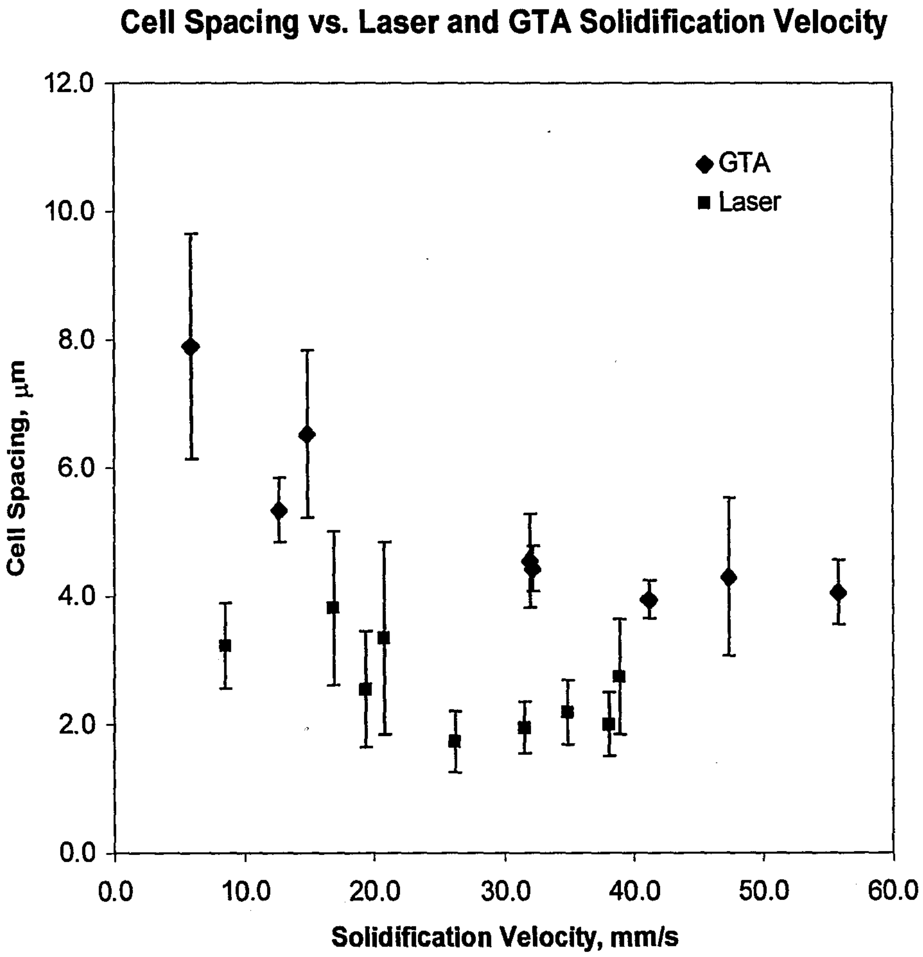

Figure 5.22 – Comparison of Laser and GTA weld cell spacings.

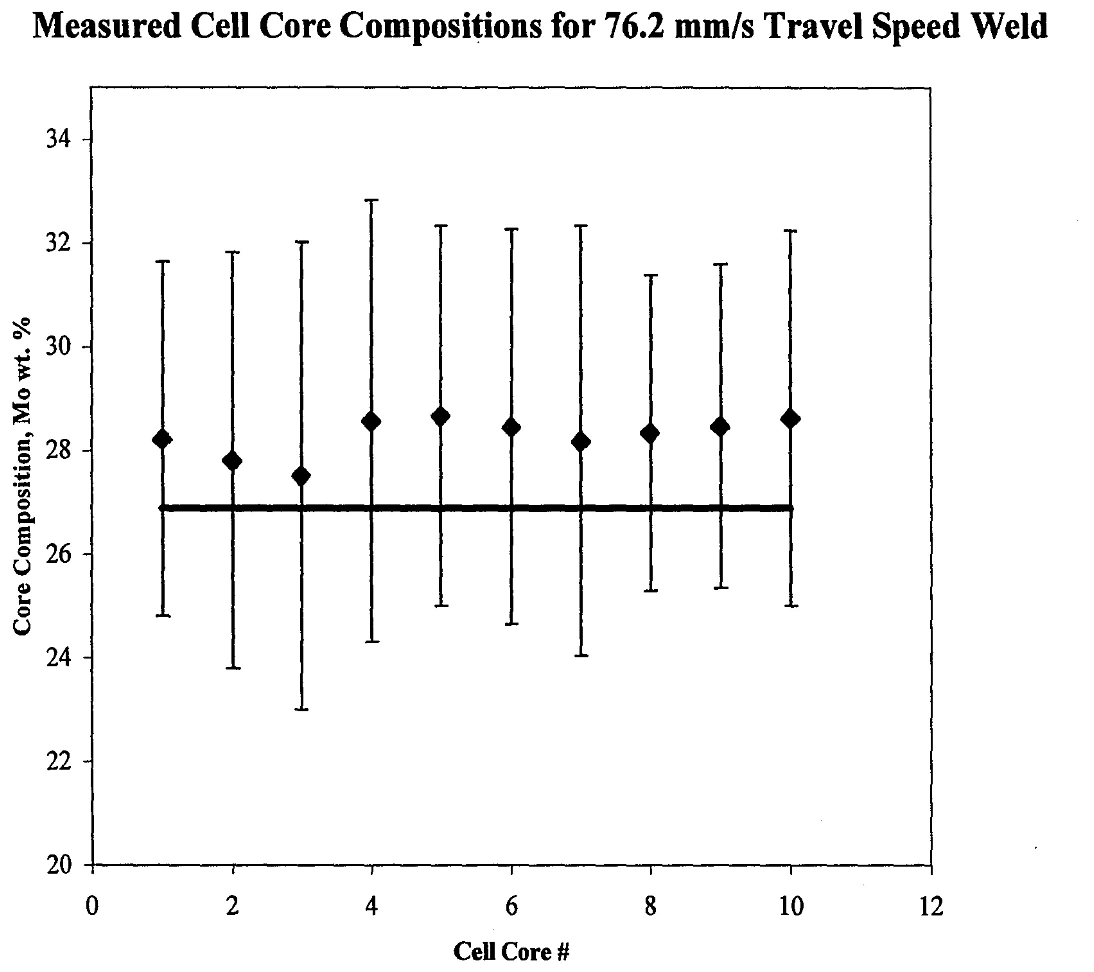

Figure 5.23A – AEM measured laser weld cell core Mo compositions (data points) as compared to KGT predicted core composition (line).

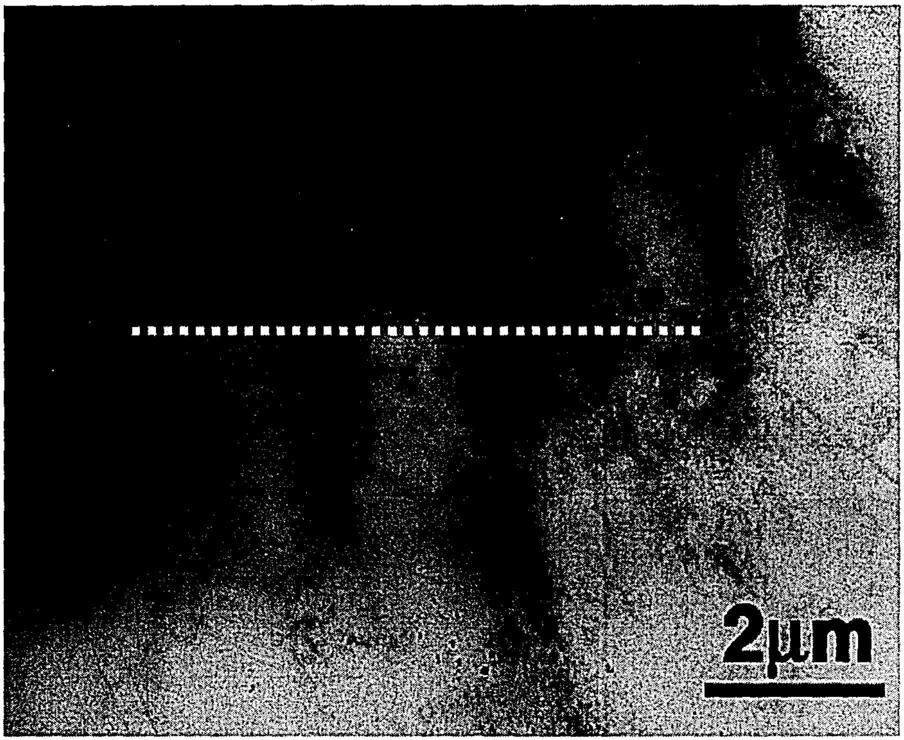

Figure 5.23B – TEM micrograph illustrating compositional traces across laser weld microstructure. The trace crosses three cells oriented parallel to the plane of the paper, each approximately 2 µm wide.

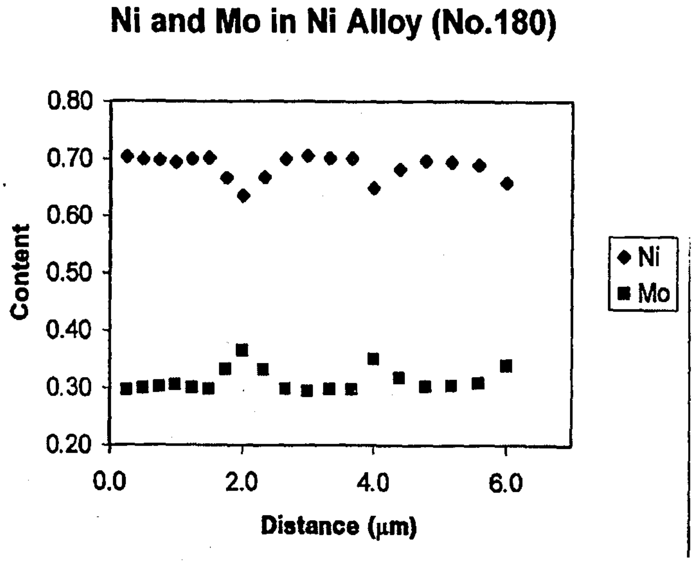

Figure 5.23C - Compositional trace corresponding to the microstructure of Figure 5.23B.

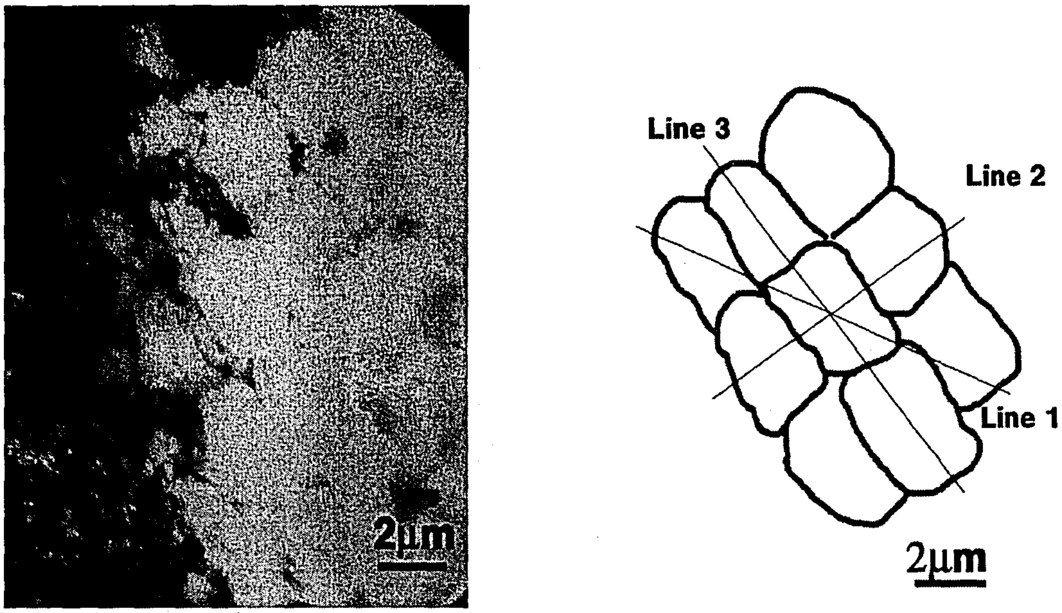

Figure 5.23D - TEM micrograph illustrating compositional traces across laser weld microstructure. The schematic illustrates three traces across the cells which are oriented perpendicular to the plane of the paper, each approximately 2 µm wide.

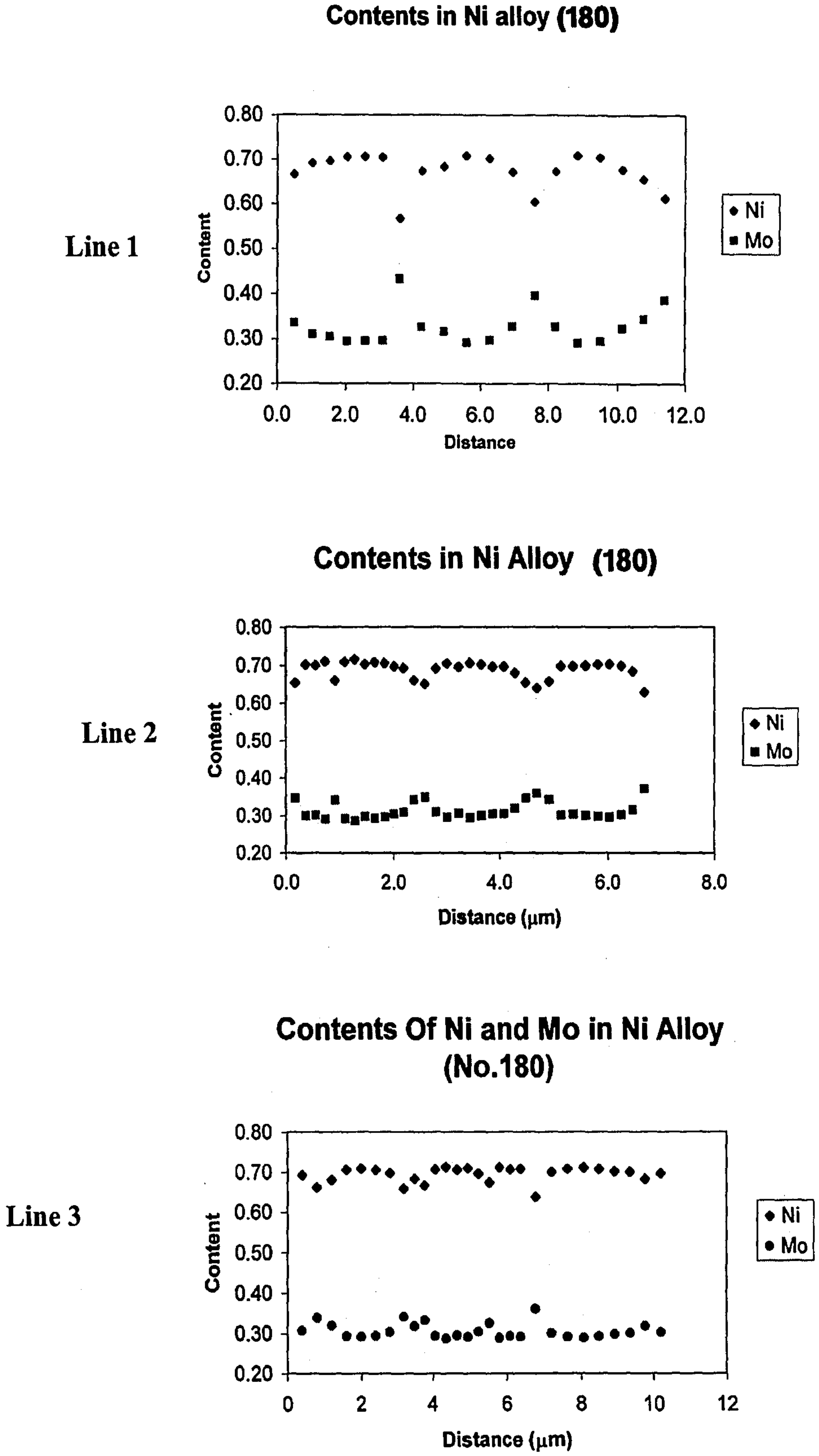

Figure 5.23E - Compositional traces corresponding to the microstructure of Figure 5.23D.

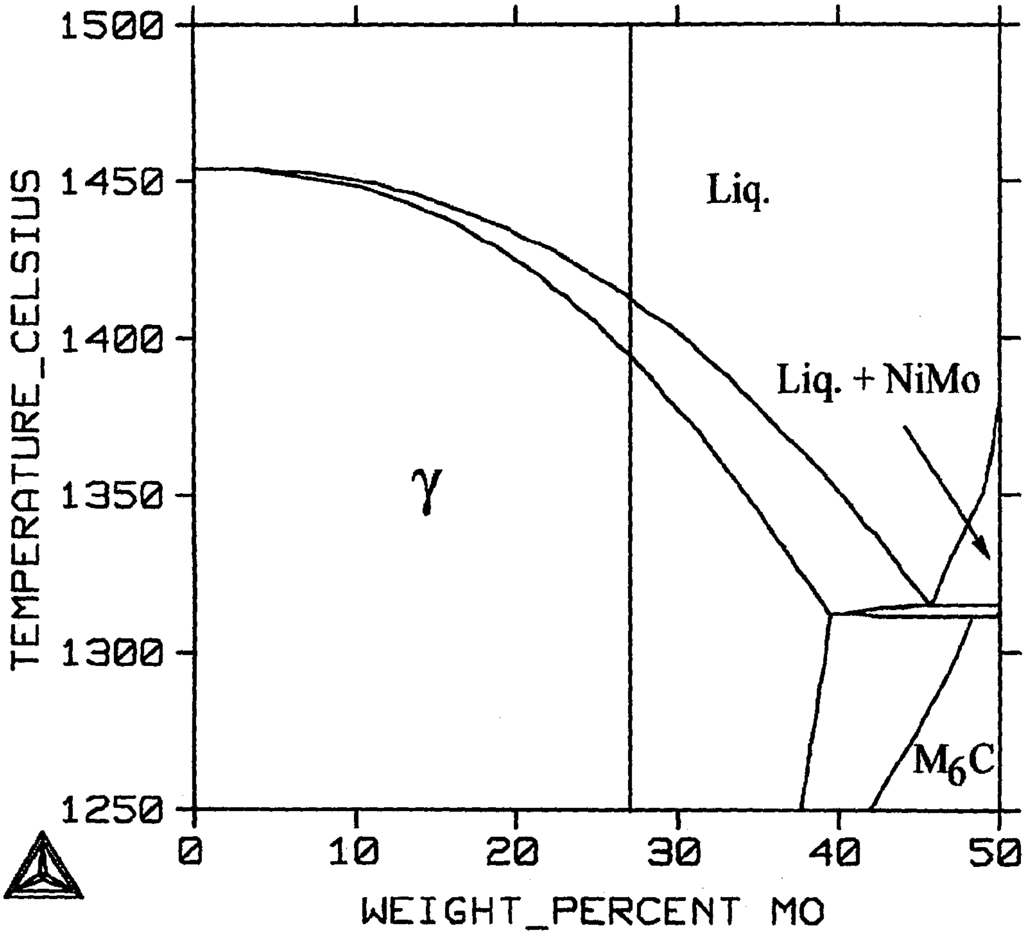

Figure 5.24 – Predicted pseudobinary phase diagram as calculated in ThermoCalc for Hastelloy B2. The red line indicates nominal Hastelloy B2 composition.

6.0 Conclusions

1. The ThermoCalc thermodynamics modeling package was found to be accurate in predicting a variety of phase diagram properties for many nickel-based alloys.

2. ThermoCalc was used successfully to model and calculate pertinent phase diagram information for the Hastelloy B2 alloy. This data was then used as input for solidification modeling.

3. The cell spacing, solidification velocity, and cell core composition were predicted from solidification modeling and found to be in good agreement with experimentally measured data.

4. It was found that the weld pool shape plays a large role in determining solidification velocity. For a high travel speed teardrop shaped weld pool it is possible to actually solidify at slower velocities than a slower travel speed hemispherical shaped weld pool.

5. GTA welds produced at high travel speeds approach laser weld microstructure in scale and solidification rate.

6. The cell core Mo composition was found to be very close to the nominal Mo composition of Hastelloy B2, indicating that the degree of microsegregation is not as severe due to cell tip undercooling.

7.0 Future Work

This work serves as an exploration of coupling the ThermoCalc program with solidification modeling when applied to nickel-based alloys. The alloy studied, Hastelloy B2, is a multi-component alloy which is essentially a binary Ni-Mo alloy with many minor additions. The main mode of solidification is austenite. Therefore, this technique could be expanded to be applied to other austenite based alloys such as stainless steels and other nickel-based alloys and super-alloys.

8.0 References

Section 1.0

1.1 Kou, Sindo. Welding Metallurgy, John Wiley and Sons, New York, 1987, p. 250.

1.2 Brooks, J.A. *Advances in Welding Science and Technology*, Ed. S.A. David, Gatlinburg, TN, 18-22 May 1986, pp. 93-99.

1.3 Fuerschbach, P.W. *Welding Journal*, January 1996, pp. 24s-34s.

Section 2.0

2.1 ASM Handbook, *Alloy Phase Diagrams Volume 3*, ASM International, 1992, pp. 2•292.

2.2 ASM Handbook, *Alloy Phase Diagrams Volume 3*, ASM International, 1992, pp. 3•45.

2.3 Bloom, David S. and Grant, Nicholas J. *Journal of Metals*, February 1954, pp. 261-268.

2.4 Raghavan, M. Mueller, R.R., Vaughn, G.A., and Floreen, S. *Metallurgical Transactions A*, 1984, Vol. 15A, pp. 783-792.

2.5 ASM Handbook, *Alloy Phase Diagrams Volume 3*, ASM International, 1992, pp. 3•45.

2.6 Lienert, T.J., Robino, C.V., Hills, C.R., Cieslak, M.J. *Proceedings of Weldability of Materials*, October 8-12, 1990, ASM, pp. 159-165.

2.7 Knorovsky, G.A., Cieslak, M.J., Headley, T.J., Romig Jr., A.D., Hammetter, W.F. *Metallurgical Transactions A*, 1989, Vol. 20A, 2149-2158.

2.8 HASTELLOY B-2 ALLOY, Product Memo H-2006E, Haynes International, Inc. 1997.

2.9 Brooks, John A. *Proceedings of Weldability of Materials*, October 8-12, 1990, ASM, pp. 41-48.

2.10 Porter, D.A. and Easterling, K.E. *Phase Transformations in Metals and Alloys Second Edition*, Chapman & Hall , London, 1993, pp. 207-249.

2.11 Smith, William F. *Principles of Materials Science and Engineering Second Edition*, McGraw-Hill, Inc., New York, 1990, pp. 419-446.

2.12 Flemings, Merton C. *Solidification Processing*, McGraw-Hill, Inc., New York, 1974, pp. 142-150, 189.

2.13 David, S.A. and Vitek, J.M. *International Materials Reviews*, 1989, Vol. 34, No. 5, pp. 213-245.

2.14 Battle, T.P. *International Materials Reviews*, 1992, Vol. 37, No. 6, pp. 249-270.

2.15 Brody, Harold D. and Flemings, Merton C. *Transactions of the Metallurgical Society of AIME*, May 1966, Vol. 236, pp. 615-634.

2.16 Sarreal, J.A. and Abbaschian, G.J. *Metallurgical Transactions A*, November 1986, Vol. 17A, pp. 2063-2073.

2.17 Brooks, J.A. and Baskes, M.I. *Proceedings of Advances in Welding Science and Technology*, May 18-22, 1986, ASM, pp.93-100.

2.18 Rosenthal, D. Congres National des Sciences, Comptes Rendus, Bruxelles, 1935, Vol. 2, pp. 1277 and Rosenthal, D., *Transactions of the ASME*, 1946, vol. 68, pp. 849. .

2.19 Rappaz, M., David, S.A., Vitek, J.M., and Boatner, L.A. *Metallurgical Transactiona A*, 1990, Vol. 21A, pp. 1767-1782.

2.20 Burden, M.H. and Hunt, J.D. *Journal of Crystal Growth*, 1974, Vol. 22, pp. 99-108.

2.21 Brooks, J.A., Li, M., Baskes, M.I., and Yang, N.C. *Science and Technology of Welding and Joining*, 1997, Vol. 2, No. 4, pp. 160-166.

2.22 Geankoplis, Christie J. *Transport Processes and Unit Operations Third Edition*, Prentice Hall P T R, Englewood Cliffs, New Jersey, 1993, pp. 192.

2.23 DuPont, Robino, Marder, Notis. *Met. Trans. A.* Vol. 29A, pp. 2797-2806.

2.24 Siredey, Nathalie and Lacaze, Jacques. *Scripta Metallurgica et Materialia*, 1993, Vol. 29, pp. 759-764.

2.25 Burden, M.H. and Hunt, J.D. *Journal of Crystal Growth*, 1974, Vol. 22, pp. 109-116.

2.26 Tassa, M. and Hunt, J.D. *Journal of Crystal Growth*, 1976, Vol. 34, pp. 38-48.

2.27 Laxmanan, V. *Journal of Crystal Growth*, 1986, Vol. 75, p. 573-590.

2.28 Trivedi, R. *Journal of Crystal Growth*, 1980, Vol. 49, pp. 219-232.

2.29 Esaka, H. and Kurz, W. *Journal of Crystal Growth*, 1984, Vol. 69, pp. 362-366.

2.30 Laxmanan, V. *Acta metall.* 1985, Vol. 33, No. 6, pp. 1023-1035.

2.31 Kurz, W., Giovanola, B. and Trivedi, R. *Acta metall.* 1986, Vol. 34, No. 5, pp. 823-830.

2.32 Langer and Muller-Krumbhaar. *Journal of Crystal Growth*, 1977, Vol. 42, pp. 11-14.

2.33 Langer, *Solidification Microstructure: 30 Years after Constituional Supercooling* (edited by H. Jones and W. Kurz), Materials Science and Engineering, 1984, vol. 65, p. 37.

2.34 Kurz, W. and Trivedi, R. *Trends in Welding Research, Proceedings of the 4th International Conference, 5-8 June 1995, Gatlinburg, Tennessee,* p. 115-120.

Section 3.0

3.1 Saunders, Nigel. "Ni-DATA a database for nickel-base alloys for use with thermochemical modeling software – ThermoCalc & MTDATA." ThermoTech LTD, Surrey, UK.

3.2 "Metallographic Preparation of HASTELLOY and HAYNES Alloys." Technical notes from Haynes International.

3.3 Fuerschbach, P.W. "Measurement and Prediction of Energy Transfer Efficiency in Laser Bean Welding." *Welding Journal*, January 1996, pp. 24s-34s.

Section 4.0

4.1. M.J. Cieslak, T.J. Headley, and A.D. Romig, Jr., *Metallurgical Transactions A*, Vol 17A, November 19886, pp. 2035-2047.

4.2 J.N. DuPont, C.V. Robino, J.R. Michael, M.R. Notis, and A.R. Marder, *Metallurgical and Materials Transactions A*, Vol 29A, November 1998, p. 2785-2796.

4.3 M.J. Cieslak, T.J. Headley, T. Kollie, and A.D. Romig, Jr., *Metallurgical Transactions A*, Vol 19A, September 1988, pp. 2319-2331.

4.4 M.J. Cieslak, T.J. Headley, T. Kollie, and A.D. Romig, Jr., *Metall. Trans.* A, 1988, Vol. 19A, pp. 2319-2331.

4.5 J.N. DuPont, C.V. Robino, M.R. Notis, and A.R. Marder, *Metallurgical and Materials Transactions A*, Vol 29A, November 1998, pp. 2797-2806.

4.6 T.J. Lienert, *Conference Proceedings Weldability of Materials*. Edited by R.A. Patterson and K.W. Mahin. October 8-12, 1990, ASM 1990, pp. 159-165.

4.7 M.J.Cieslak, T.J. Headley, G.A. Knorovsky, A.D. Romig, Jr., and T. Kollie, *Metallurgical Transactions A*, Vol. 21A, February 1990, pp. 479-488.

4.8 G.A. Knorovsky, M.J. Cieslak, T.J. Headley, A.D. Romig, Jr., and W.F. Hammetter, *Metallurgical Transactions A*, Vol. 20A, October 1989, pp. 2149-2158.

4.9 C.V. Robino, J.R. Michael, and M.J. Cieslak, *Science and Technology of Welding and Joining*, Vol. 2, No. 5, pp. 220-230.

Section 5.0

5.1 Dupont, J. N. and A.R. Marder, Welding Journal, Dec. 1995, pp. 406s-416s.

5.2 Okada, A. 1977. Applications of melting efficiency and its problems, Journal of the Japan Welding Society, vol. 46, #2, pp. 53-61.

5.3 J.W. Elmer, Sc.D. Thesis, Massachusetts Institute of Technology, Cambridge, Ma, 1988 p. 188.

5.4 J.W. Elmer, Sc.D. Thesis, Massachusetts Institute of Technology, Cambridge, Ma, 1988 p. 189.

5.5 Kou, Sindo. <u>Welding Metallurgy</u>, John Wiley and Sons, New York, 1987, p. 24.

5.6 Fuerschbach, P.W. *Welding Journal*, January 1996, pp. 24s-34s.

5.7 David, S.A. and Vitek, J.M. *International Materials Reviews*, 1989, Vol. 34, No. 5, pp. 213-245.

9.0 Vita

Brian Dale Newbury was born in Silver Spring, MD to the parents of Barbara and Dale Newbury on July 23, 1976. He graduated from Quince Orchard High School in 1994. He then attended Lehigh University from 1994-1998, obtaining a B.S. degree with honors in Materials Science and Engineering. Upon completion of his B.S. degree, Brian has been pursuing his M.S. in Materials Science and Engineering and just finished it today!

END OF
TITLE